Study of variability in L- and T-type brown dwarfs: spectral indices and theoretical models

Natalia Lucia Oliveros Gomez

Advisor: Dr. Elena Manjavacas
Co-Advisor: Dr. Dennis Jack

Thesis submitted in fulfilment of the requirements for the degree of Master of Science

Universidad de Guanajuato
Departamento de Astronomía
2023

It has been a challenge to study objects for which you have more questions than answers. But it has been worth it from the academic to the personal.

Acknowledgements

Thanks to the academic support of RECA[1] (Network of Colombian Students in Astrophysics, for its acronym in Spanish) for creating the partnership with my advisor[2], in the RECA Internship 2021, who brought me closer to this area of astronomy that captivated me from the beginning and who has supported me in every step of my academic career, opening doors to what it is to be a professional, or to be a 'scientist'. Thanks to the collaboration and comments about Spectral indices[3]. Thanks to my co-advisor[4] for his support and guidance within the UG.

But above all, thanks to the personal support of my parents[5] and my sister[6] for never leaving me alone, in spite of the more than 3000 km that separate us. For to be my accomplices in the crazy things that may occur to me. Thanks to my nephew[7] just for her existence in my life. Thanks to my partner[8], for being the perfect equilibrium between personal and academic life, and for teaching me about happiness and priorities. And finally, thanks to all the people in @arrecifecosmico[9] who have accompanied me through social media and all that is involved in wanting to do science as an average Colombian.

[1] RECA: https://www.astroreca.org/
[2] Elena Manjavacas
[3] Daniella Bardalez Gagliuffi
[4] Dennis Jack
[5] Roger Oliveros and Olga Lucía Gómez
[6] Catherine Oliveros Gomez
[7] Coral A. Oliveros
[8] Missael Hernandez-Huerta
[9] @arrecifecosmico: https://www.instagram.com/arrecifecosmico/

Study of variability in L- and T-type brown dwarfs: spectral indices and theoretical models

Natalia Lucía Oliveros Gómez

Abstract

The majority of brown dwarfs, also referred to as BDs in the rest of the text, show some level of photometric or spectro-photometric variability (changes in flux) in different wavelength ranges. Variability is most likely due to heterogeneous cloud structure in the atmospheres of these objects and allows us to trace the 3D atmospheric structures of variable brown dwarfs and directly-imaged exoplanets with radiative-transfer models and mapping codes. Nevertheless, not all brown dwarfs show variability, thus finding brown dwarf variables is crucial to studying their atmospheric structures. Finding variable dwarfs requires extensive observing monitoring which implies at minimum a few hours per object, and therefore consumes a lot of resources. The purpose of this thesis is to find a systematic method that would allow the community to find the most likely variable brown dwarfs without the need to spend long hours of telescope time. To this aim, we designed variability spectral indices, that can predict whether a BD will show variability using low resolution near-infrared (NIR) spectra, prior to photometry monitoring.

Spectral indices in brown dwarfs have previously been used to classify spectral binaries whose combined light spectra have different peculiarities, independent of separation (Burgasser et al. 2006, Bardalez Gagliuffi et al. 2014). Now, we designed and tested these NIR spectral indices to pre-select the most likely variable mid-L and mid- and late-T dwarfs, which overlap in effective temperatures with directly-imaged exoplanets. We used time-resolved NIR *Hubble Space Telescope Wide Field Camera 3* spectra of an L6.5 (LP 261-75b), and a T6.5, (2MASS J22282889-431026), to design our novel spectral indices.

We tested these spectral indices on 76 L4–L8 and 26 T5.5–T7.5 NIR SpeX/IRTF spectra. providing eight new mid- and late-T variable candidates. We estimated the variability fraction of our sample in 51^{+4}_{-38}% for L-dwarfs and 38^{+4}_{-30}% for T-dwarfs, which agrees with the variability fractions provided by Buenzli et al. (2014), Radigan et al. (2014) and Metchev et al. (2015), dedicated photometric monitoring ground-based and space surveys in NIR and MIR. We provided a list of 27 new L-variable candidates and 6 new T-variable candidates. We have a recovery rate for variables dwarfs of $\sim 92\%$ and a false-negative rate of $\sim 8\%$ for L- dwarfs and $\sim 67\%$ and a false-negative rate of $\sim 12.5\%$ for T-dwarfs. In both cases, all the known non-variable brown dwarfs were recovered by our indices. These spectral indices may be applicable to directly-imaged

exoplanets of similar effective temperatures and might support the selection of those most likely variables to monitor for variability with the *James Webb Space Telescope* and the 30-m telescopes.

In addition, we compare the observational data of the two main objects of study J2228-4310 and LP 261-75B with the spectroscopy synthetic models to understand the atmospheric behavior in which clouds play a more important role and therefore present greater variability. We found the best fit for J2228-4310 using petitcode-cool-clear model, we found an effective temperature of $T_{\rm eff}$ = 1000 K, a surface gravity of log(g) = 4.9 dex. The best fit for LP 261-75B was petitcode-hot-cloudy model, we found an effective temperature of $T_{\rm eff}$ = 1430 K, and a surface gravity of log(g) = 4.20 dex. Finally, we compare and discuss the main differences between L- and T- dwarfs.

Resumen

La mayoría de las enanas marrones muestran algún nivel de variabilidad fotométrica o espectrofotométrica en diferentes rangos de longitud de onda (cambios en el flujo). Lo más probable es que la variabilidad se deba a la estructura heterogénea de nubes en las atmósferas de estos objetos. Aplicando modelos de transferencia radiativa y códigos de cartografía es posible trazar estructuras atmosféricas tridimensionales de las enanas marrones variables y de los exoplanetas de imagen directa. Sin embargo, no todas las enanas marrones muestran variabilidad, por lo que encontrar enanas marrones variables es crucial para estudiar sus estructuras atmosféricas. Encontrar enanas variables requiere un extenso seguimiento de observación que implica como mínimo unas pocas horas por objeto, siendo muy intensivo en recursos. El objetivo de esta tesis es encontrar un método sistemático que permitiera a la comunidad encontrar las enanas marrones variables más probables sin necesidad de dedicar largas horas de telescopio. Para lograr este objetivo, diseñamos lo que llamamos índices espectrales de variabilidad.

Los índices espectrales en enanas marrones se han utilizado previamente para clasificar binarias espectrales cuyos espectros de luz combinados tienen diferentes peculiaridades, independientemente de la separación del sistema (Burgasser et al. 2006, Bardalez Gagliuffi et al. 2014). Ahora, diseñamos y probamos estos índices espectrales en el infrarrojo cercano para preseleccionar las enanas variables más probables de L-media y T-media y tardía, que coinciden en temperaturas efectivas con los exoplanetas observados con imagen-directa. Utilizamos espectros en el infrarrojo cercano resueltos en el tiempo de la *Wide Field Camera 3* ubicada en el *Hubble Space Telescope* de una L6.5 (LP 261–75b), y una T6.5, (2MASS J22282889–431026), para diseñar nuestros novedosos índices espectrales.

Probamos estos índices espectrales en 76 espectros del infrarrojo cercano L4–L8 y 26 T5,5–T7,5 del catálogo SpeX/IRTF. Estimamos la fracción de variabilidad de nuestra muestra en 51^{+4}_{-38}% para enanas L y 38^{+4}_{-30}% para enanas T, lo que concuerda con las fracciones de variabilidad proporcionadas por Buenzli et al. (2014), Radigan et al. (2014) y Metchev et al. (2015) dedicados a hacer seguimiento fotométrico de enanas marrones con telescopios terrestres y espaciales en NIR y MIR. Proporcionamos una lista de 27 nuevos candidatos a la variable L y 6 nuevos candidatos a la variable T.. Proporcionamos una lista de 27 nuevas candidatas a variables L y 8 nuevos candidatos a variables T. Tenemos una tasa de recuperación para enanas variables de $\sim 92\%$ y una tasa de falsos negativos de $\sim 8\%$ para enanas L y de $\sim 67\%$ y una tasa de falsos negativos de $\sim 12,5\%$ para enanas T. En ambos casos, todas las enanas marrones no variables conocidas fueron recuperadas por nuestros índices. Estos índices espectrales pueden aplicarse a exoplanets observados con imagen-directa de temperaturas efectivas similares, y podrían ayudar a seleccionar los variables más probables para monitorizar la variabilidad con el *James Webb Space Telescope* y nuevos telescopios de 30 m.

Además, comparamos los datos observacionales de los dos principales objetos de estudio LP 261-75B y J2228-4310 con los modelos sintéticos de espectroscopia para comprender el comportamiento atmosférico en el que las nubes desempeñan un papel más importante y, por tanto, presentan mayor variabilidad. Encontramos el mejor ajuste para J2228-4310 usando el modelo petitcode-cool-clear, con el que encontramos una temperatura efectiva de $T_{\rm eff} = 1000$ K y una gravedad superficial de $\log(g) = 4{,}9$ dex. Para LP 261-75B el mejor ajuste fue con el modelo petitcode-hot-cloudy, donde encontramos una temperatura efectiva de $T_{\rm eff} = 1430$ K y una gravedad superficial de $\log(g) = 4{,}20$ dex. Por último, comparamos y discutimos las principales diferencias entre las enanas L y T.

Contents

List of Tables

List of Figures

Chapter 1

Introduction

Brown dwarfs occupy a unique position in the field of astronomy, like a dividing line between stars and planets. These celestial objects have captured the attention of astronomers due to their atypical properties and the valuable insights they offer into the mechanisms of formation and evolution of planetary systems. A key aspect that has emerged as a focal point of the research is the study of the atmospheres of brown dwarfs, which are of significant importance for understanding the physical processes that take place in the interior of these objects.

The study of the atmospheres of brown dwarfs allows us to understand the physical conditions, chemical composition, and dynamic processes that take place in the interior of brown dwarfs, about their formation, evolution, and overall composition (Joergens, 2016). To knowing the composition of these objects, they help us to contrast the formation processes of both stars and planets. By characterizing the atmospheres, we understand the initial conditions and environmental factors that influence the formation of these intermediate objects. This is aligned with understanding the gap between our understanding of planetary formation and star formation, offering valuable clues about the complex interplay between disks, accretion, and the formation of substellar objects (Chabrier, Baraffe, 2000).

In addition, by analyzing the spectra of their atmospheres and the emission characteristics of brown dwarfs at different wavelengths, we can discern the molecules composition, sedimentation, condensates, temperature profiles, vertical transport energy, formation and dissipation of clouds. This contributes to the understanding of atmospheric dynamics, energy transport mechanisms, and cloud formation processes in the interior of brown dwarfs. They also provide valuable data for refining atmospheric models and simulating the behavior of these objects under various conditions.

For these reasons, in this thesis, we will focus on the study of BD atmo-

spheres, and divided this manuscript to describe the most important aspects to be taken into account during this study in Chapter 1, our contributions in the analysis of brown dwarf atmospheres from observational data - spectral indices and theoretical models with their respective results and discussion (Chapter 2 and 3, respectively). The most relevant conclusions and a summary are in Chapter 4.

1.1 Brown dwarfs

Brown dwarfs were first predicted theoretically in the 1960s (Hayashi, Nakano 1963, Kumar 1963), proposing them as "failed stars", answering the question: what if there is an object that in its star formation process does not reach sufficient mass to fuse hydrogen? However, it was not until two decades later, in 1988, that an object was discovered with characteristics that could indicate that it was the first observed brown dwarf, which was a companion of a white dwarf, but due to the lack of information about the orbits and nature of the object, it was not possible to distinguish whether it was a low-mass star, an exoplanet or, a brown dwarf. It was not until 1995 that the first unambiguous example of a brown dwarf was observed, Gl229B (Nakajima et al., 1995), which showed strong methane absorption that firmly established that it was too cool to be a star (Oppenheimer et al., 1995). At about the same time, Teide 1 was discovered (Rebolo et al., 1995), which was identified as a promising brown dwarf candidate in the Pleiades open cluster, due to the presence of the Li I line in its optical spectrum, indicating the absence of hydrogen fusion.

1.1.1 Definition

Brown Dwarfs (BD) are sub-stellar objects (SSO), i.e., they are not massive enough to create the temperature and pressure conditions in their core to sustain burning hydrogen. The study of BD is a field in which relatively little research has been carried out (<50 years), so there is still much were to be done, establishing a formal definition. In the literature, several definitions have been proposed that are based on different principles. For this thesis, we will rely on the definition presented by Chabrier, Baraffe (2000), based on observational data, the physics of the formation of these objects, and the mass limit. Brown dwarfs are free-floating objects with masses below the minimum hydrogen burning mass (0.075 $M_{\odot}$, Burrows et al. 2001), regardless of whether they burn deuterium or not. This definition also includes objects that are companions of a parent star or another BD, formed from the same molecular cloud.

Brown dwarf formation theory indicates that during their pre-main-sequence contraction phases, the cores of these low-mass objects become electron-degenerate, and it is this degeneracy that prevents the object from collapsing further. Normally, in objects with higher masses, the contraction is halted due to the gas pressure and allows the burning of hydrogen, which generates the spectral types of stars OBAFGKM, O representing the hottest stars and M the coolest.

The discussion about BD formation continues, In some studies Cruz et al. (2007), Chabrier et al. (2014) found that the formation scenario of a brown dwarf must be like that of stars. They observed that the brown dwarfs studied are consistent with the same 'universal' Initial Mass Function (IMF). The IMF is an empirical function that describes the initial distribution of masses for a population of stars during star formation. The same IMF that applies to stars is the same that extends to the BD regime (still under debate), and they did find a fragmentation limit close to the H-burning limit, as we can see in Figure 1.1. However, the astronomers still have not modeled the IMF at low masses because it is so hard to measure BD masses (due to age, mass, luminosity degeneracy). Kirkpatrick et al. (2021) discuss about IMF in BD located at less than 20 pc, they find that the best fit is a power law ($dN/dM \propto M^{-\alpha}$) with $\alpha = 0.6 \pm 0.1$. Also, the spike seen at 1200K $< T_{eff} <$ 1350 K, believed to be caused by an increase in the cooling timescale across the L/T transition.

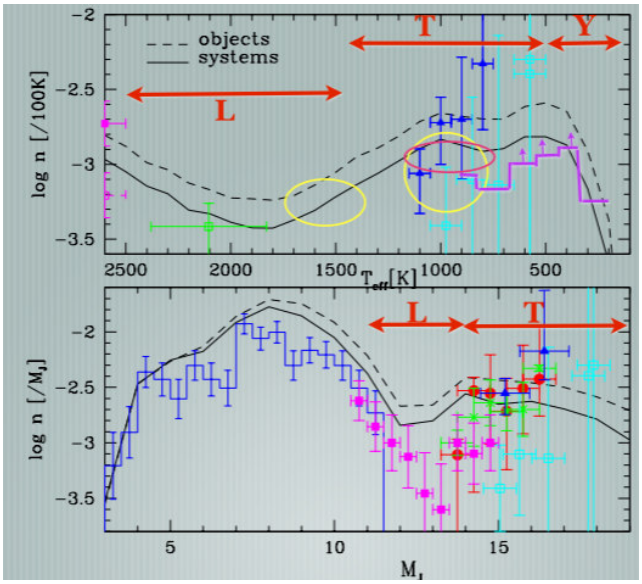

Figure 1.1: Numerical density of brown dwarfs as a function of $T_{\rm eff}$ (top) and absolute J-magnitude (bottom) predicted with a Chauvin et al. (2005) IMF for resolved objects (dashes) and unresolved binary systems (solid). Taken from Chabrier et al. (2014)

On the other hand, more recent studies such as Miret-Roig et al. (2022),

show us that the ejection of planets from their planetary systems could have a contribution comparable to that of core collapse in the formation of free-floating planets (FFP), usually mistaken for brown dwarfs because they share characteristics such as temperature and colors.

The formation scenarios and evolution can define the differences between stars, BD, and giant planets. These studies are made by probing regions where objects are found especially at early, nearer ages, open clusters, and star-forming regions (Luhman, 2012). We can study brown dwarfs mainly at near-infrared wavelengths ($1 - 2.5\mu$m, YJHK bands), even warmer brown dwarfs, can often be detected in red optical bands ($0.6 - 1\mu$m, RIZ bands).

1.1.2 Classification

The identification of Brown Dwarfs is based on the measurement of colors, and magnitudes, from photometry and the measurement of Spectra Energy Distribution (SED) of these cold objects, from spectroscopy. The BDs have very characteristic strong molecular absorption bands (best seen at low resolution), with which radial velocity calculations can be obtained and spectral types can be constrained, giving hints of the effective temperature and mass of a candidate.

The mainly brown dwarf parameters comprise effective temperatures between $T_{eff} \sim [2600 - 250]$ K. They are divided into their three spectral types For L-dwarfs have $T_{eff} \sim [2600-1300]$ K, for T-dwarfs have $T_{eff} \sim [1300-600]$ K and Y-dwarfs have $T_{eff} \sim [600-250]$ K. The BDs have typical surface gravities between $\log g \sim [3, 5]$ dex, depending on the age (Joergens, 2016). They have radii between $R \sim [0.5, 1.5]\ R_J$, and decrease with lower temperatures (Lueber et al., 2022).

Now, based on the analysis of spectra at optical and IR wavelengths, we can find differences in the internal compositions and the importance of different molecules. **late-M dwarfs** are characterized by H_2O absorption-band strength, and the presence of alkali and metal oxides like VO, and TiO. **L-dwarfs** are characterized by a variety of atomic and molecular bands, such as alkaline and neutral. L-dwarfs present H_2O, FeH, and CO strength bands, and the main alkaline lines are Na, Fe, K, Al, and Ca (see Figure 1.2).

The **L/T transition** is characterized by the stronger H_2O band, alkaline and neutral lines, and less pronounced hydride lines. **T-type** have an important contribution to the alkaline bands of NaI, and KI, which begin to suppress the continuum, and in their decreased hydrides and oxides contribution (Burrows et al., 2003), also they have strong CH_4 band, and have strength the H_2O band (see in Figure 1.2).

In **Y dwarfs** as the effective temperature decreases, NH_3 absorption becomes important (Lodders, Fegley Jr 2002; Burrows et al. 2003). In Figure 1.2, we can observe the differences in molecular composition between the spectra for different spectral types. Also, how the hydride bands become stronger with later types and the oxide bands decrease in strength with later types (Kirkpatrick, 2005).

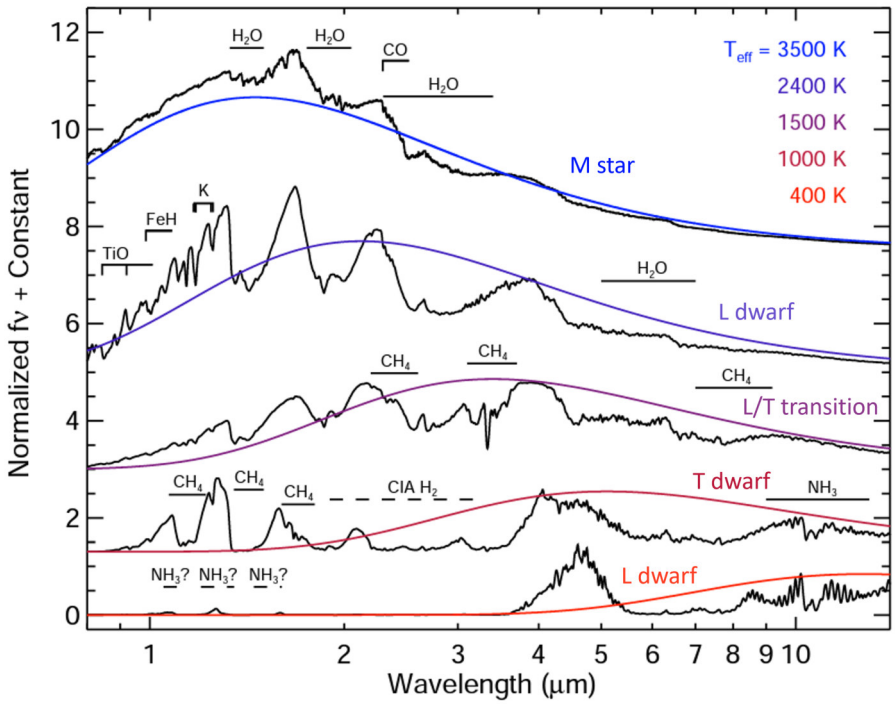

Figure 1.2: Example of spectra of different spectral types of brown dwarfs indicating the presence of different types of molecules in their atmosphere composition. Taken from Cushing website Resources (https://irtfweb.ifa.hawaii.edu/~cushing/resources.html) and modified with the name of spectral types.

From the colors and absolute magnitudes, we get relevant information that gives us clues for a possible classification. While stars, we have the Hertzsprung-Russell diagram, we can produce an empirical equivalent from brown dwarfs in a color-magnitude diagram (Figure 1.3). In the color-magnitude diagram, we can distinguish the 2 most relevant spectral types (L, and T). Also, we include the M-dwarfs, although these are stars, the later types and those of older age begin to have characteristics similar to those of brown dwarfs. We do not include the Y type, because here we focus on $J-$ and $H-$band, and the colors of Y dwarfs will be too faint in those bands, and also because we

focus on the analysis of L- and T-dwarfs

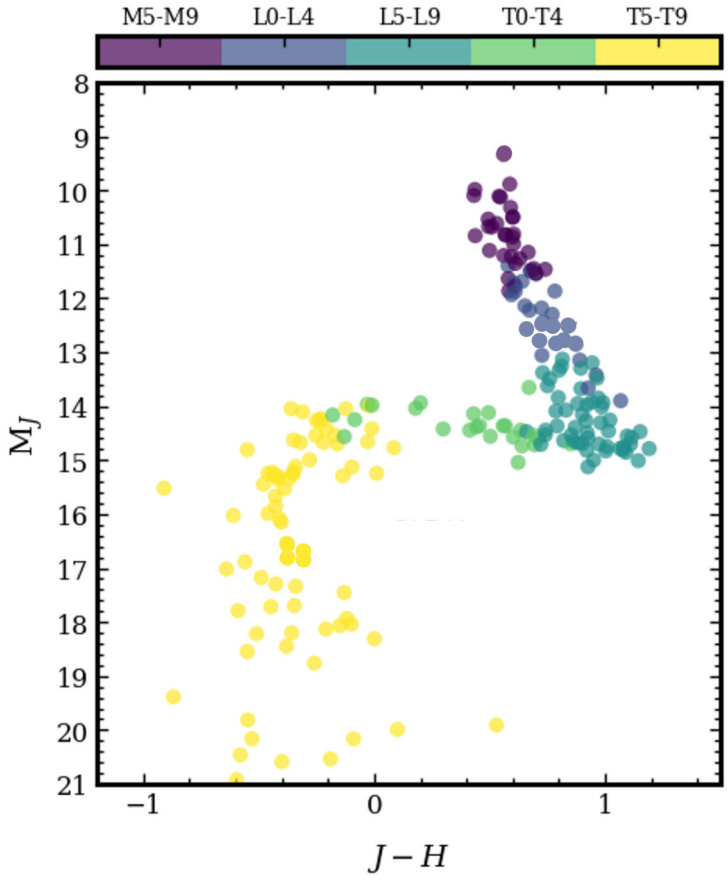

Figure 1.3: Color–magnitude diagram in the MKO system showing all ultracool dwarfs using the `SPECIES Code`.

1.2 Modelling BD Atmospheres

Brown dwarf atmospheres are dynamic. Within BD atmospheres, thermochemical reactions occur which may be after a time of reaching the chemical equilibrium (t_{chem}), and may vary with respect to the atmospheric altitude. In addition, other phenomena occur that do not allow equilibrium to be reached, for example, convection. The phenomenon of convection consists of transporting heat through the movement of fluids. In disequilibrium cases, it is necessary to parameterize the convective process.

The most important cases to study in BD, in reference to the disequilibrium atmospheres are the convective mixing or/and cloud cover. To understand

both processes we can apply the Eddy diffusion analysis. Eddy diffusion is the method to study the swirling of a fluid and the reverse current created when the fluid is in a turbulent flow regime, parameterizing the system in terms of a fluid continuity equation. We included the parameter K_{zz} that represents how efficiently the atmosphere transports the material upwards. This analysis is based on the Mixing Length Theory (see in Section 1.2.1) and depends on the temperature-pressure profile T(P).

In addition, the timescales are important references to study the composition distribution, for example, the *quench point* of species, above that level has freezes where the timescale for convective mixing t_{mix}, based on the mixing length and vertical mixing rate, is equal to the timescale of the kinetic chemical timescale t_{chem} (such that species freeze). There are assumptions about which chemical pathways will be important in the deep atmosphere. This level is different for each species. Therefore, in this section, we will describe some details that are necessary to understand atmospheres and the relevance of their study (Fegley, Prinn, 1985).

1.2.1 Radiative Transfer theory

The importance of understanding the inner atmosphere is to know the behavior of energy transfer in the form of electromagnetic radiation. For this reason, it is necessary to understand conceptually and mathematically the parameters that affect the light we can measure from these objects to understand the spectra of objects, how they might vary over time, and in general the properties of their atmospheres.

The opacity sources depend on the chemical composition of the gas and clouds, gravity, and pressure-temperature relation. The chosen opacities are the key to radiative transfer modeling. The main sources come from:

- Atomic opacity: The major contributors to atomic opacity are bound–bound line transitions and bound-free photoionization into the continuum. This type of opacity is concerned with transitions between energy levels of an atom.

- Molecular opacity: Product of molecule interactions within a molecule, such as rotational, vibrational, or transitions between blended energy levels.

- Line opacity: The opacity $\sigma_{lu}(\nu)$ is made of a component for the strength of the transition (line intensity: S_{lu}) and one for the line broadening function, including natural, doppler, and collisional broadening. That affects the width and T-dependence.

- Raman opacity: Generates short wavelength optical/UV scattering due to the presence of molecules, similar to Rayleigh scattering but weaker. In the case of planets and brown dwarfs, it can significantly affect the albedo, rotational or vibrational states of the molecule. It occurs even in molecules that do not have these transitions like H_2, N_2.

- σ_{MIE} opacity: As a result of the scattering of electromagnetic radiation by spherical particles, Mie's theory provides a complete analytical solution to Maxwell's equations for these cases. According to the wavelength and particle size, we can have the cases:

  - For $r >> \lambda$: Geometric optics.
  - For $r << \lambda$: Rayleigh scattering.

  Where r is the radius of the particle and λ is the observed wavelength.

On the other hand, in addition to the opacities, it is necessary to take into account conditions inside the atmosphere that help us describe the interactions mathematically, known as internal structure equations that must be included in the radiative transfer analysis:

- Hydrostatic equilibrium: Starting from the consideration of a gravitational force is opposed to a force generated by pressure, which varies with depth. These two are always opposite, assuming a spherical symmetry, which is static, and therefore the acceleration has a value of zero. Here, ρ is the density, M_r is the mass in a specific radius r, and G is the gravitational constant,

$$\frac{dP}{dr} = -G\frac{M_r\rho}{r^2} = -\rho g; \quad \frac{dP}{dM_r} = -\frac{GM_r}{4\pi r^4}.$$

- Mass conservation: Assuming a spherical symmetry for the stars, we can consider a mass differential dM_r within a thickness dr located at a distance r,

$$\frac{dM_r}{dr} = 4\pi r^2\rho; \quad \frac{dr}{dM_r} = -\frac{1}{4\pi r^2\rho}.$$

- Energy generation in the core, that in the case of brown dwarfs, we observe only the deuterium burning or the internal heat, thus the gradient of luminosity is product to the internal energy ϵ,

$$\frac{dL_r}{dr} = 4\pi r^2\rho\epsilon; \quad \frac{dL_r}{dM_r} = \epsilon.$$

- Energy transport, to understand the temperature-pressure profiles. Here ∇ is the gradient of the temperature and pressure $\frac{d\ln T}{d\ln P}$

$$\frac{dT}{dr} = -\frac{GM_r\rho T}{r^2 P}\nabla; \quad \frac{dT}{dM_r} = -\frac{GM_r\rho T}{4\pi r^4 P}\nabla$$

- Energy conservation: On a local scale, we can say that the conservation of energy is given, starting from the first law of thermodynamics, and considering spherical shells, inside the constant mass heat changes are related to mass changes $\delta Q = \delta q \Delta m$.

Taking into account the possible opacities, also expressed as cross-sections, and the internal structure equations, mentioned above and that we have interactions in the interior of emission and absorption, we proceed to define the radiative transfer equation as

$$\frac{dI}{ds} = -\sigma_t(s)I(s) + \sigma_s(s)\int_0^\infty \rho(\mu)I(s,\mu)d\mu + S(s), \tag{1.1}$$

where:

- I is the intensity of radiation as a function of distance s and direction μ. Where μ is a parametrization of $cos\theta$
- σ_t is the total cross-section for absorption and scattering.
- σ_s is the scattering cross-section.
- $\rho(\mu)$ is the phase function, which describes the probability of scattering in a given direction μ.
- S is the source term, which represents the medium with which the radiation under study is interacting.

Within the atmosphere, all opacities and physical quantities interact with light depending on the frequency or wavelength. In different spectral regions, there are opacities that are more relevant than others. Therefore, to solve the equations, it is necessary to make assumptions that simplify the calculations. One such assumption that is appropriately used in the codes is to assume a '*gray atmosphere*', i.e., a wavelength-independent extinction coefficient. While this is not a realistic assumption, the non-gray problem can be reduced to the gray case with average opacities. In this case, the solution will automatically satisfy the gray RTE and the RE condition, using *Milne's equation*:

$$I(\tau) = I(0) + \int_0^\tau S(\tau')e^{-\tau+\tau'}d\tau' \tag{1.2}$$

where:

- $I(\tau)$ is the radiation intensity as a function of optical depth τ.
- $I(0)$ is the initial intensity of radiation at $\tau = 0$.
- $S(\tau')$ is the source term, which represents the external radiation sources as a function of optical depth τ.

However, for cool stars, or in the case of brown dwarfs, it is important to take into account factors such as *convection*, which usually affects the outer atmosphere. To describe convection there is no true theory of convective energy transport, but there are comparatively simplistic models for convection that fit optically thick media best. In these cases, for large opacities, one has large temperature gradients ΔT or a given F flux. Opacities are usually large in the P - T regions with ionization, making ionization opacities very relevant.

The model used to describe convection is the *Mixing Length Theory*. Originally developed by Prandtl (1925) and adapted to astrophysics by L. Biermann and modernly updated by Böhm-Vitense (1958). It posits the idea of energy transport by bubbles moving upward (hot) and downward (cold) through the atmosphere. These bubbles transport excess energy upward and dissolve after traveling a characteristic distance, mixing length l then dump the excess energy to the surroundings.

In addition, it is necessary to take into account the internal dependent parameters like the temperature-pressure profile relationship, since it allows us to appreciate which molecular components and condensates of a variety of species can be found within an atmosphere at different altitudes. To correctly account for cloud opacity, it is necessary to model each condensate-forming species, estimating particle sizes and vertical distributions. However, modeling condensates of molecules is difficult both experimentally and theoretically. Therefore, there is a limited list of molecules that are included in the processes of this type of cold atmosphere objects. And these calculations are mainly based on chemical equilibrium calculations.

In Figure 1.4, we can see an example of profile curves for different objects with different effective temperatures, T_{eff} (in blue), and in dotted lines the condensation curves for different molecules. In addition, the cut-off points of the two types of curves would be the heights at which clouds of these particulate molecules can condense. There are numerous atmospheric condensates within the pressure-temperature regime of brown dwarfs. However, not all are of equal importance. It is also necessary to take into account the molecular abundances and how they contribute to the opacities at different optical depths, which creates a challenge for cloud modeling.

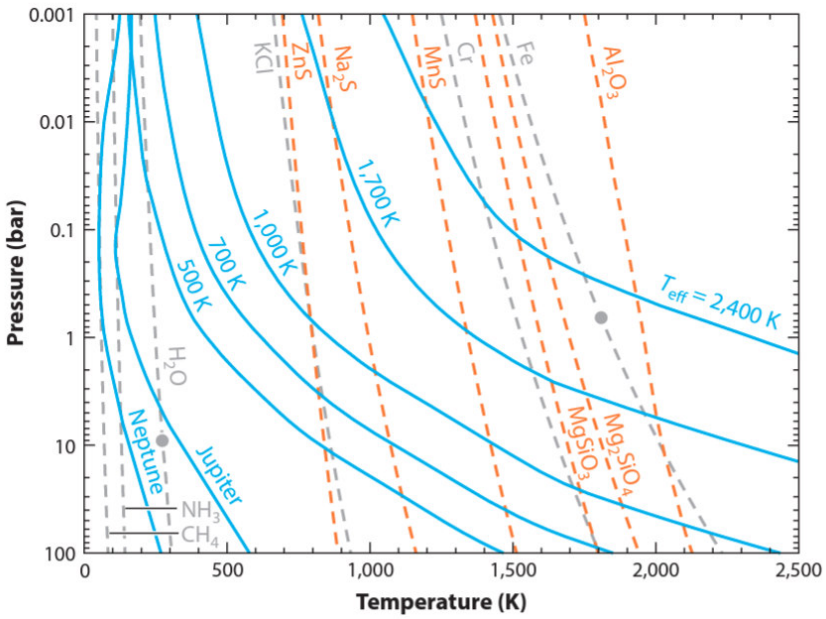

Figure 1.4: Condensation curves for a variety of species (dashed), assuming solar abundances from Lodders (2003). Gray curves are for direct condensation, whereas orange curves are for condensates that form as a result of chemical reactions. Filled circles indicate a liquid-solid transition. Several cloud-free model thermal profiles are provided for comparison (in blue), as well as empirically derived profiles for Jupiter and Neptune. Taken from: Marley, Robinson (2015)

1.2.2 Chemistry of brown dwarf atmospheres

Chemical equilibrium refers to when the number density of atoms, molecules, and condensates is equal in density in a closed system, such as the atmosphere. Although there are changes at the microscopic level, there are no net changes in the system.

In brown dwarf atmospheres, the most important reaction include carbon (C), oxygen (O), and nitrogen (N), which generate mainly oxides and silicates. The fundamental reaction is

$$CO + 3H_2 \longrightarrow CH_4 + H_2O.$$

It is important to consider the initial distribution of C, and O. For high temperatures CH_4, and CO switch to the dissociated forms via the following reactions, depending on the shape of the T-P profile and metalicity of the object:

$$CH_4 \longrightarrow CH_3 + H$$
$$CO \longrightarrow C + O$$

Normally, CH_4 dominates in the upper part of the atmosphere, while CO dominates in the deeper, and hotter layers. If CH_4 is not present, CO can dissociated by $2CO \longrightarrow C + CO_2$. Thus, the spectral measurement of CH_4 can function as a temperature indicator.

For atmospheres with effective temperatures $T_{eff} > 650$ K, there is enough H_2O in the gaseous state, which allows for conversion to CO_2. The major sinks of oxygen are the oxides of magnesium silicates, which make up around 20% of MgO_3Si, while the rest of oxygen gets sequestered into TiO, VO, Al_2O_3, among others.

For the N contribution in the atmospheres, it condenses around $T_{eff} \approx 131$ K. Thus, it is more relevant for low temperatures. For higher metallicity, there is an increase in the number of NH_3 and presents the reaction

$$N_2 + 3H_2 \longrightarrow 2NH_3.$$

In addition, the dominant mixture can be:

$$H_2O/CO/N_2$$
$$H_2O/CH_4/N_2$$
$$H_2O/CH_4/NH_3.$$

As mentioned, chemical models and chemical equilibrium reactions can provide information about the internal composition of these objects depending on the spectral classification (temperature, gravity, and metallicity). In the case of M-type brown dwarfs, there is a presence of TiO and VO, which lower temperatures are given an estimate during the M/L transition. In the optical, L-dwarfs have neutral absorption lines that dominate the spectrum. The elements Na, and K are perturbed by H_2. In the NIR, methane was fundamental at 3.3 μm band for the middle L-type. And for the end L-type, especially at 1, 2.2, and 7.8 μm. L-type brown dwarfs have molecules such as TiO_2 or TiO_3 (perovskite) that begin to form in the atmosphere as well as aluminum condensates (Al_2O_3), and calcium aluminates that form at higher temperatures than titanium compounds, followed by Mg condensates at lower temperatures. In these objects, the opacity of the oxygen band is weakened causing the alkali and hydride (FeH, CrH) lines to increase.

During the L/T transition, the dust disappears from the photosphere due to gravity settling, since the higher the gravity, the more clouds are lost below the photosphere. The condensates, both in quantity and size, control the scattering and absorption, and hence the emergent flux varies quite a lot between these

two spectral types, especially in the NIR, it is necessary to take into account all the parameters mentioned previously to properly characterize BD atmospheres (Section 1.2.1). From here we can refer to the color-magnitude diagram of these objects (Figure 1.3) to see how brightness fluctuates in the L/T transition NIR colors change quickly. In this transition, a condensate rain stage is observed while ending approximately in the middle of the T-type, after which, another cooling stage occurs similar to that of the initial to mid-L types. This is evidenced in Figure 1.3, in the horizontal branch.

1.3 Time-resolved observations

According to Khandrika et al. (2013), a cloud "represents" the large visible ensembles of droplets or crystals suspended in the gaseous atmosphere. In the atmospheres of exoplanets and brown dwarfs, it is challenging to identify the formation path of solid or liquid particles based on observed spectral features.

In brown dwarf atmospheres, 'dust' describes grains formed by condensation of gases in an atmosphere, such as those mentioned in Section 1.2.2. When the opacity of the dust is optically thin, it affects the intensities of individual spectral line profiles. In contrast, a 'cloud' would describe grains formed by condensation that affect the intensity of the optical and/or near-infrared continuum of spectra, due to the significant opacity of the grains over a wide wavelength range.

Many brown dwarfs show some level of photometric or spectrophotometric variability in different wavelength ranges (e.g. Apai et al. 2013, Radigan et al. 2014, Metchev et al. 2015, Zhou et al. 2018, Biller et al. 2018, Vos et al. 2019, Manjavacas et al. 2019, Vos et al. 2020, Vos et al. 2022). Although other scenarios are possible (Tremblin et al., 2015, 2016), the most likely reason to explain the variability of brown dwarfs is the existence of a heterogeneous cloud cover (Apai et al., 2013) in their atmospheres at different pressure levels. This variability allows us to trace the three-dimensional atmospheric structures of variable brown dwarfs and exoplanets observed directly with radiative transfer models and mapping codes. Therefore, finding variable brown dwarfs is crucial to studying their atmospheric structures. But so far, the only techniques available for the determination of atmospheric variability are through the application of many hours of observation time, either from photometry or spectrophotometry.

1.3.1 Time-resolved photometry

Some photometric light curves of brown dwarfs show us a variability of the flux in small periods of time, of hours (bottom of Figure 1.5). However, this variability is not present in all brown dwarfs with similar spectral types (top of Figure 1.5). This represents that similar BD spectral types have different internal structures. Thus, it is important to study the variability to know in detail what is the behavior in the BD atmospheres.

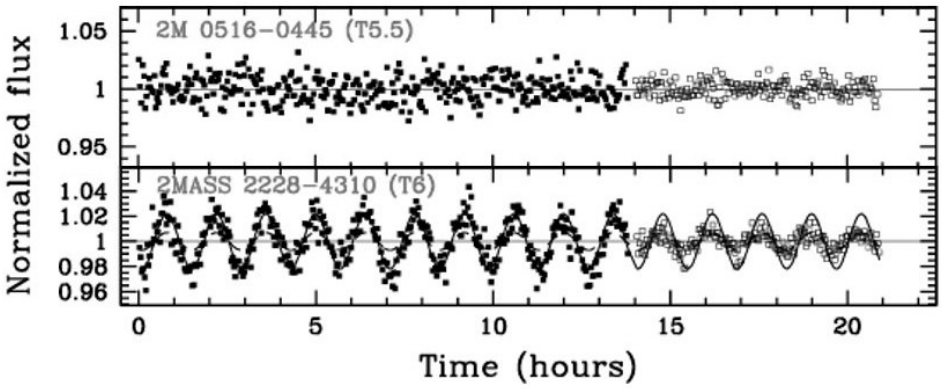

Figure 1.5: Example of two brown dwarfs with and without (2MASSJ05160945-0445499) and with (2MASS J22282889–4310262) photometric variability in J band, respectively. Taken from Metchev et al. (2015)

This variability is λ-wavelength dependence. When analyzing variable light curves of brown dwarfs across different wavelength ranges, there is a clear trend of the phase shift in the variability period and amplitude across different λ-ranges, which correlates with the probed pressure observed at the respective wavelengths: the lower the pressure of the atmospheric layer, the larger the phase shift with respect to the higher pressure layer (see in Figure 1.6). So we can begin to combine our observational studies with theoretical models as described above.

According to this result, the photometric variability detected in brown dwarfs can be attributed to three main scenarios: (1) a change in the temperature–pressure profile $T(P)$ without a change in opacities, where warmer regions may be the result of subsidence, which advects high entropy gas from above. In comparison, cooler regions may be the result of upwelling, which advects low entropy gas from below (Tremblin et al. 2015, Tremblin et al. 2016, Tremblin 2019). (2) a change in the opacities (clouds and/or gas) without change in $T(P)$, due to heterogeneous cloud cover in their atmospheres (Saumon, Marley 2008, Apai et al. 2013, Yang et al. 2016, Biller et al. 2018, Zhou et al. 2018). (3) an intermediate scenario.

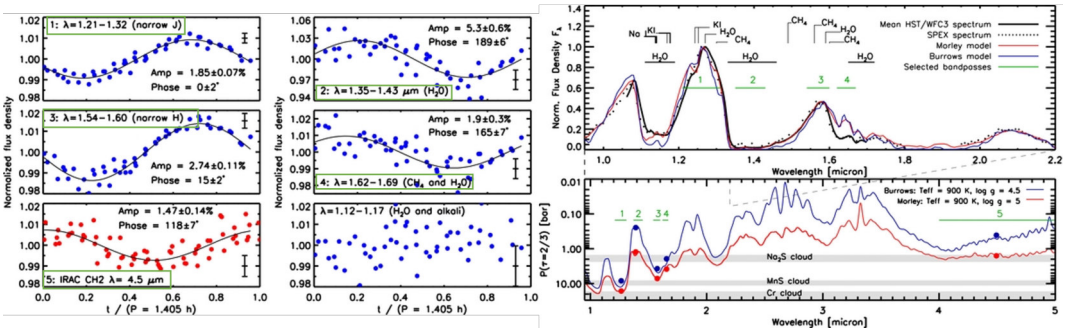

Figure 1.6: 2M2228 spectrum integrated over different bandpasses. normalized HST/WFC3 spectrum of 2M2228 and best-fit atmospheric models by Morley and Burrows. Pressure level probed at optical depth $\tau = 2/3$ as a function of wavelength for the two models. Taken from: Buenzli et al. (2012)

Due to the importance of understanding the atmospheres of brown dwarfs from their variability, the community has spent significant effort in time-resolved surveys with ground-based (Radigan et al., 2014) and space-based telescopes (Buenzli et al. 2014, Metchev et al. 2015). Radigan et al. (2014) monitored a sample of 57 L, L/T, and T-dwarfs in the J-band using the Du Pont 2.5 m telescope at Las Campanas Observatory and the Canada–France–Hawaii Telescope on Mauna Kea. Radigan et al. (2014) reported significant variability with a fraction of $39^{+16}_{-14}\%$ of L9–T3.5 dwarfs and hat $60^{+22}_{-18}\%$ of mid-to-late L and T dwarfs (excluding L9–T3.5 spectral types). Similarly, Buenzli et al. (2014) monitored a sample of 22 L5 to T6 dwarfs with the *Hubble Space Telescope/Wide Field Camera 3* in the J- and H-bands, finding a variability fraction of $29^{+20}_{-10}\%$ of L-early type, $40^{+21}_{-16}\%$ of L-mid type, and $29^{+20}_{-10}\%$ of T-mid type. In addition, Metchev et al. (2015) monitored a sample of 44 L3 to T8 dwarfs using the *Spitzer* Space Telescope in the [3.6] and [4.5] channels, reported significant variability with a fraction of $61\%^{+17\%}_{-20\%}$ of L3–L9.5 dwarfs and $31\%^{+25\%}_{-17\%}$ of T0–T8. Metchev et al. (2015) concluded that $80\%^{+20\%}_{-27\%}$ of L-dwarfs vary by $\geq 0.2\%$, and $36\%^{+26\%}_{-17\%}$ of T-dwarfs vary by $\geq 0.4\%$. We notice that the difference in variability fraction per spectral type in the different surveys is most likely due to the following factors:

- The difference in sensitivity between ground-based and space-based telescopes.
- The wavelength range at which each sample was observed.
- The different time scales in the observations.

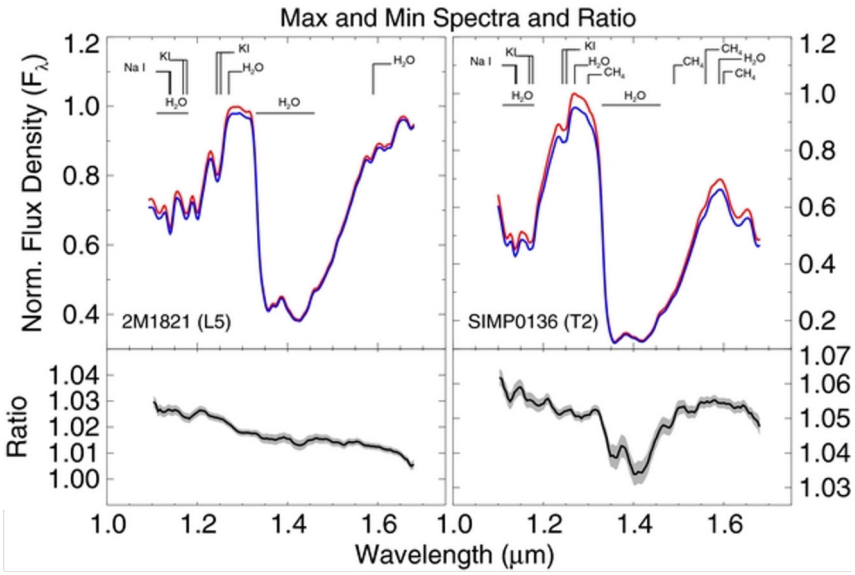

Figure 1.7: Comparison between brightest (red) and faintest (blue) spectra, to understand the variability ratios (minor panel) in different wavelength ranges, during one HST visit for 2M1821 (L6), and SIMP0136 (T2), respectively. We can notice the different dependence in terms of the spectral type objects. Taken from: Yang et al. (2015)

1.3.2 Time-resolved spectrocopy

As mentioned in Section 1.3.1 we can observe the different depths of the atmosphere, with near-infrared photometry, in particular, J-, H-, or K-bands. Using spectroscopy, we can take a more detailed look across wavelengths and continue to study variability in specific absorption lines and bands. With spectroscopy, we can observe different depths of the brown dwarf atmosphere. The cloud cover depends on the pressure-temperature profile, thus we have cloud formation at different heights according to the spectral type. Thus, we can find areas of the spectrum with greater variability than others, and correlate the specific pressure levels in the atmosphere.

Yang et al. (2015) studied the spectral variability in different wavelength ranges and concluded that the variability of the 1.4 μm water band can probe the height of cloud decks in the atmospheres of T-dwarfs (see Figure 1.7). A weaker wavelength dependence of the spectral variations observed in L dwarfs, which would indicate that the dust grains giving rise to the flux variability are likely located at high altitudes, which is also in line with the general model predictions (Yang et al., 2015).

Yang et al. (2016) used radiative transfer and atmospheric chemistry models to compare with observational spectra and determine the flux contribution

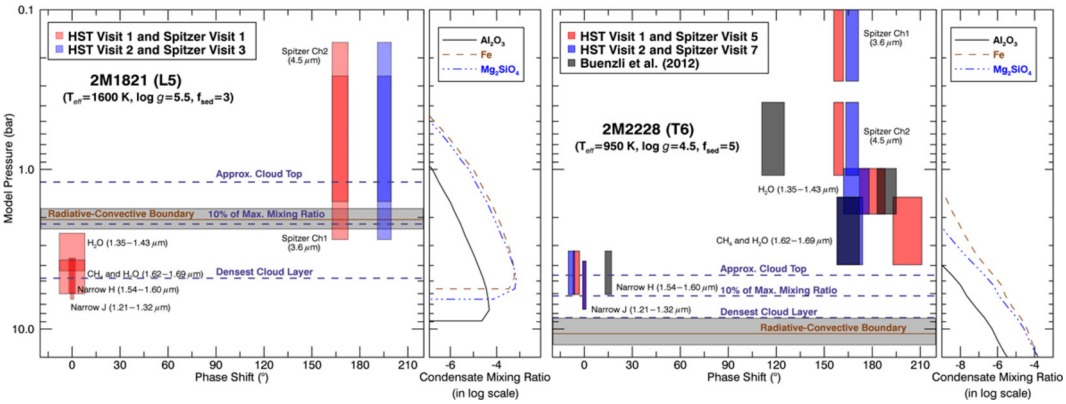

Figure 1.8: Left panel: Phase shifts between light curves of spectral bands plotted as a function of characteristic pressure levels for 2M1821 (L6), and 2M2228 (T6), respectively. We note the impact of variability in different spectral ranges with respect to the depth position of atmospheres and cloud condensation. Right panel: condensate volume mixing ratio in the model plotted as a function of model pressure. Taken from: Yang et al. (2016)

of each pressure layer to different spectral bands (see Figure 1.8). They show how the limit to the radiative-convective boundary changes depending on the spectral type, and the clouds coverage too. In the case of T dwarfs, the boundary is deeper, thus we can observe greater variability only in J, and H bands, in the lower part of the atmosphere. But, in the case of L dwarfs present high variability in other bands as 3.6μm and 5.4μm bands. In addition, we observe how the condensate mixing ratio of different molecules and their relevance for different altitudes changes.

1.4 Motivation

As explained above, time-resolved photometric or spectroscopic data provide a wealth of information about the internal structure of the atmospheres of brown dwarfs. Nonetheless, not all brown dwarfs show photometric or spectroscopic variability. Until now, to determine if a brown dwarf is variable or not, long hours of telescope time are needed to investigate if a particular object would show variability or not, which is very resource-intensive.

Throughout this thesis, we adopted both an observational and theoretical approach to the study of the atmospheres of brown dwarfs. Our aim for this master thesis is to **generate a systematic method to determine variable candidates' brown dwarfs L- and T-type to facilitate the study of atmospheric variability due to heterogeneous clouds.** This method might be also applicable to the analogs of brown dwarfs, directly-imaged exoplanets,

which will be the focus of the study for the *James Webb Space Telescope*, and the next generation of 30-m telescopes. Thus, this method will likely save the community's expensive telescope time. Have a tool that can guide the search for variable objects more easily, study and understand the complexity of the atmospheres of brown dwarfs, and even consider the possibility of extending it to exoplanets that share temperature and color characteristics with BD. We develop the method and discuss its results in Section 2, both for L- and T-dwarfs.

The method we designed is based on observational spectral indices. Previously, spectral indices have been used in this field of brown dwarfs, as a method to calculate fractions of spectral binaries of brown dwarfs, whose combined light spectra show different peculiarities, allowing an independent identification of the separation between objects (Burgasser et al. 2006, Bardalez Gagliuffi et al. 2014). However, within their results, they found that for some cases, objects with variability within the binary classification were found. Therefore, our objective is based on a similar principle, but this time analyzing additional characteristics that focus on the internal variations of the atmosphere that generate the variability.

A second aim is to **understand the internal structure of brown dwarfs and the role of clouds in the spectra of these objects**. In Section 3, we explain the theoretical models that we use to generate synthetic spectra and compare them with observational data and we discuss the main results.

In Section 4, we summarize the most important results of this thesis and mention some ideas that we can develop in the future, thanks to the results obtained. Finally, in the Appendices A and B, we include relevant information about the individual objects that we took into account to test our method and which have already been studied in the literature.

Chapter 2

Method to identify variable candidate brown dwarfs

We designed a set of novel spectral indices to identify the most likely variable brown dwarfs. Spectral indices are flux ratios that allow us to compare the flux in different spectral ranges within the same spectrum of one object. In Ashraf et al. (2022), we used existing indices (Bardalez Gagliuffi et al., 2014) in new parameter spaces for L/T dwarfs transition.

2.1 Spectral Indices Method

We designed spectral indices using near-infrared HST/WFC3 spectra to find candidate variable L and T dwarfs using any single-epoch near-infrared spectra, with the aim of facilitating the search for photometric and spectro-photometric variability L and T dwarfs, stating from low-resolution archival NIR spectra.

The time-resolved near-infrared HST/WFC3 spectra of LP 261-75B (L6) were published in Manjavacas et al. (2018) and J2228-4310 (T6) were published in Buenzli et al. (2012). We have an NIR light curve for each object (See Figure 2.1), where each data point is a NIR time-resolved spectrum itself. To design our spectral indices, we explored which wavelength ranges of the HST/WFC3 spectra of each object vary within the object's rotation due to its heterogeneous cloud coverage.

We obtained the most and least variable wavelength ranges of each spectrum for each object. For that, we subtracted each of the maximum flux spectra from a spectral template (see Figure 2.2), created by median combining all HST/WFC3 spectra. Then, we identified the corresponding wavelength ranges in which the difference between the most variable spectrum and the template spectrum is maximum and minimum (in absolute value). The template spectrum would be similar to a single-epoch spectrum in which several minutes of

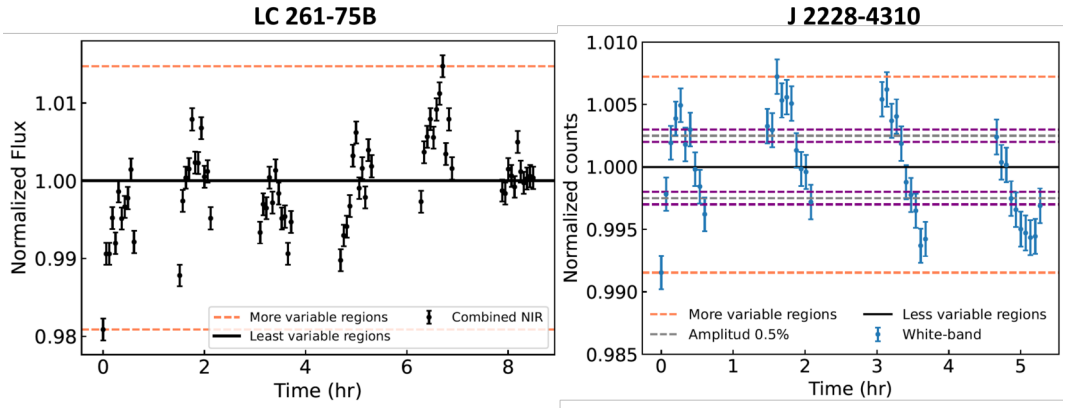

Figure 2.1: Near-infrared light curve of LP261-75B (left) and J2228-4310 (right), to identify areas of variability from visual inspection. The least variable spectra are those corresponding to the center of the light curve (flux 1, black line). The most variable spectra are those corresponding to the peaks of the light curve (orange dashed lines).

integration are needed to obtain a high signal-to-noise spectrum.

The most variable wavelength ranges are those that have higher absolute difference values, and the least variable wavelength ranges are those that have absolute differences (subtraction) close to zero. We found that the most and least variable regions of each spectrum are similar for all spectra. In Figure 2.2, we highlighted in blue the most variable wavelength ranges of the spectra, and in red the least variable wavelength ranges. The wavelength ranges are defined as the moving average of the entire spectrum with 0.03 mm wide windows that are shifted every 0.01 mm. After obtaining the mean values in each window, we selected two regions as the most and least variable, for the J- and H-band.

Following this process, we consolidated the spectral ranges to create spectral indices to measure the variability in the H-band and in the J-band, which are calculated with Equation 2.1.

$$\text{index} = \frac{\int_{\lambda_1}^{\lambda_2} F_1(\lambda) d\lambda}{\int_{\lambda_3}^{\lambda_4} F_2(\lambda) d\lambda} \tag{2.1}$$

In Equation 2.1, the numerator is one of the most variable regions of the spectrum, and the denominator is an adjacent least variable region. Both cover the same wavelength width. In addition, for each spectral type, we include other indices according to the properties of each spectrum, which are better detailed in Section 2.2 for the L-method and Section 2.3 for the T-dwarfs.

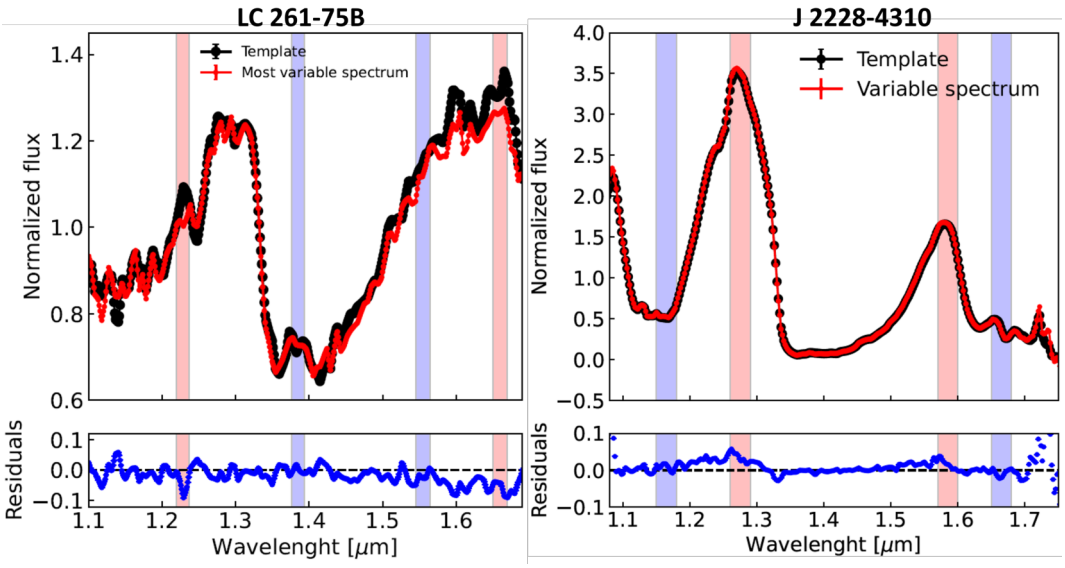

Figure 2.2: Top panel: *template* of LP261-75B (left) and J2228-4310 (right) after combining the median of the 66 HST/WFC3 spectra (black), and an example of a variable spectrum for LP261-75B and J2228-4310, respectively. Lower panel: residuals after subtracting the variable spectrum of LP261-75B and J2228-4310 with the *template*. We highlight in red the most variable region, and in blue the least variable regions of the spectrum according to the residuals shown.

2.2 Method to identify variable L-dwarfs

2.2.1 Spectroscopic observations

The data used for our analysis were obtained on December 21, 2016 (UTC) with the infrared channel of the *Wide Field Camera 3* (WFC3) on board the *Hubble Space Telescope* (HST) and its G141 grism, in Cycle 23 of the HST program. That provides spectra covering a wavelength range between 1.05 and 1.69 μm (P.I. D. Apai, GO14241). These spectra were published in Manjavacas et al. (2018).

The observations were performed using a 256 x 256 pixels subarray of the WFC3 infrared channel, with a plate scale of 0.13 arcsec/pixel. In addition, a direct image was taken at each orbit in the F132N filter to obtain an accurate wavelength reference. The spectra were acquired over six consecutive HST orbits, spanning 8.49 hr, obtaining a total of 66 spectra. In each orbit, we obtained 11 spectra. The spectral resolving power was 130 at 1.4 μm.

In Figure 2.1 (left) we can observe the infrared light curve, using a spectral range between 1.1-1.69 μm of this LP261-75B object, which presents a pho-

tometric variability appreciable to the naked eye, with a maximum variability in peak-to-peak amplitude of 3.25%, where the spectra with the highest variability are those at the extremes of the light curve and those with the lowest variability are those closest to unity, and where each of the points represents a spectrum.

In addition, each point in the NIR light curve is a spectrum. In Figure 2.2 (left) we see an example, in which the most variable spectrum is compared with respect to the *template*, with the respective residuals of the comparison

2.2.2 Method

We applied the method described in Section 2.1, taking into account indices used in previous studies (Table 2.1), totaling six spectral indices to predict variability in L-dwarfs.

Spectral index	Numerator Range (μm)	Denominator Range (μm)	Feature	Reference
H	1.22-1.25	1.375-1.405	Difference variability in H-band	(1)
J	1.64-1.67	1.545-1.575	Difference variability in J-band	(1)
max-var	1.66-1.69	1.34-1.37	Minor difference variability	(1)
H_2O-J	1.975-1.995	2.08-2.10	1.90 μm H_2O	(2)
CH_4-J	1.635-1.675	1.56-1.60	1.65 μm CH_4	(2)
J-curve	1.26-1.29	1.14-1.17	Curvature across J-band	(3)

Table 2.1: Limiting ranges used for the creation of spectral indices. References: (1) This document, (2) Burgasser et al. (2006) (3) Bardalez Gagliuffi et al. (2014)

We apply these indices to all 66 spectra of the brown dwarf LP261-75B, to make index-index plots and observe the behavior of each of these spectra, as shown in Figure 2.3. As can be seen at a glance, two delimited areas are marked, separating the spectra with higher variability amplitude from the less variability ones. The goal is to delimit these areas with greater mathematical rigor.

Variability areas

Given that we have a limited amount of spectra for LP261-75B, before we can robustly define the *variable* and *non-variable* areas in the index-index plots in Figure 2.3, we generated synthetic spectra, similar to the most and least variable spectra of LP261-75B, to further help in the definition of both areas. Using a Monte Carlo simulation we generated 100 synthetic spectra from the least variable spectra of LP261-75B, and 100 synthetic spectra from

the most variable spectra. To generate the synthetic spectra using a Monte Carlo simulation, we selected the most and least variable spectra in the light curve and redefined each point in the spectrum using a Gaussian random number generator. The mean value of the Gaussian is the original flux of the spectrum, and the standard deviation is the uncertainty of each point in the sample spectrum. Finally, we ran our spectral indices through all synthetic spectra, and we generated new index-index plots (see Figure 2.4).

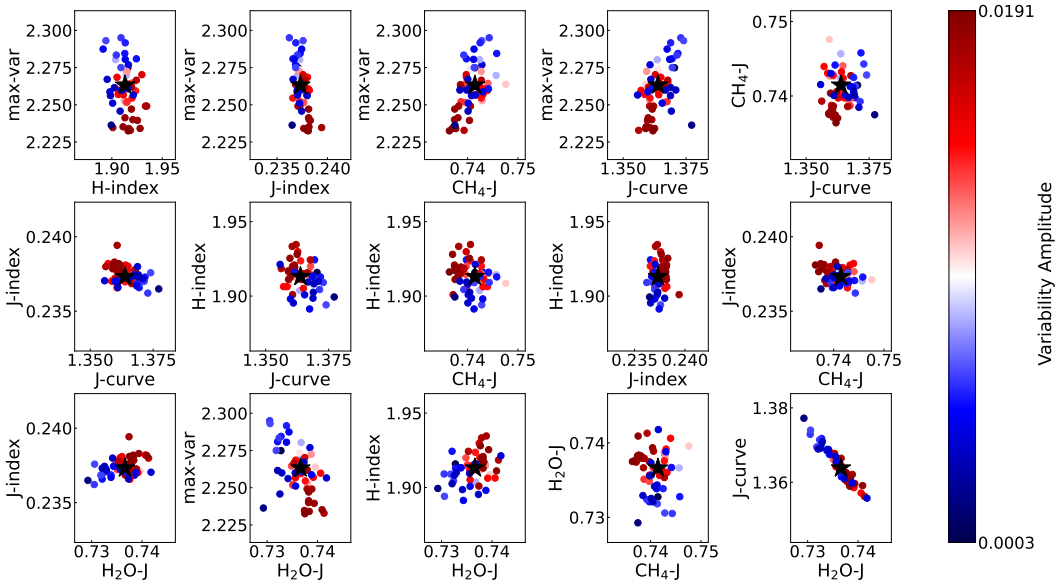

Figure 2.3: Index-index plots which compare all spectral indices among them for the HST/WFC3 spectra of LP261-75B. The blue dots correspond to the spectra showing the smallest variability amplitude ($\sim$ 1.0 on the light curve in Figure 2.1 - left), and the red dots correspond to the higher variability amplitude (about 1.01 or 0.98 on the light curve in Figure 2.1 - left). The black star in the center corresponds to the calculated indices for the template spectrum, as a reference of a single-epoch spectrum.

To robustly define the variable and non-variable areas of the index-index plots, we use a supervised learning method, *Support Vector Machine* (SVM). To use the SVM method, we must provide a sample containing the points and their value that classifies it to one category or another. In our case, we generated a sample with the points of each index-index plot for the 200 synthetic spectra created with the Monte Carlo simulation -described above-, and with the value assigned to it if it is variable (1) or non-variable (0).

The SVM method uses a portion of the sample values as training examples so that it begins to iterate to classify the two groups and evaluate them. This is in order to maximize the gap between the two categories. Then, use the rest

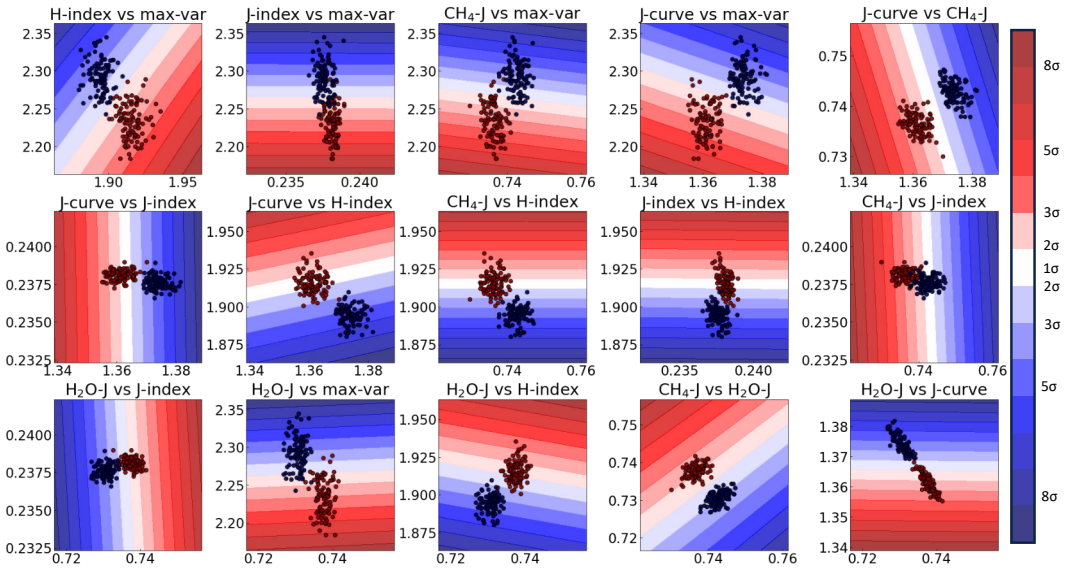

Figure 2.4: Index-index plot same as Figure 2.3, but using the synthetic spectra generated with the Monte Carlo method from the HST/WFC3 spectra of LP261-75B. The most variable spectra are shown as red dots, and the least variable spectra are shown as blue dots. We show the areas of variability computed using *Machine learning* (`scikit-learn`) with their respective reliability regions.

of the sample data to map the space that is predicting which category they belong to and evaluate the method.

We used `scikit-learn` to apply this supervised learning method (Pedregosa et al., 2011). In addition, we were able to do kernel variations (linear, radial basis, and polynomial) to define the separation boundaries of the two categories. We decided to use a 'linear' kernel because it shows the most consistent results. We also tested varying the number of contour levels to use, which is related to the reliability of finding an object in one category or another. We ended up with 15 contours because, from this value, the results were no longer changed.

We note in Figure 2.4 that the contours separating the two categories are not reliable to classify as variable or non-variable ($1 - 2\sigma$). The reliability in the areas increases, declaring objects in the 3σ regions and above as being in a reliable variable or non-variable area. Variable areas are shown in red $> 3\sigma$, and non-variable areas are shown in blue ($> 3\sigma$).

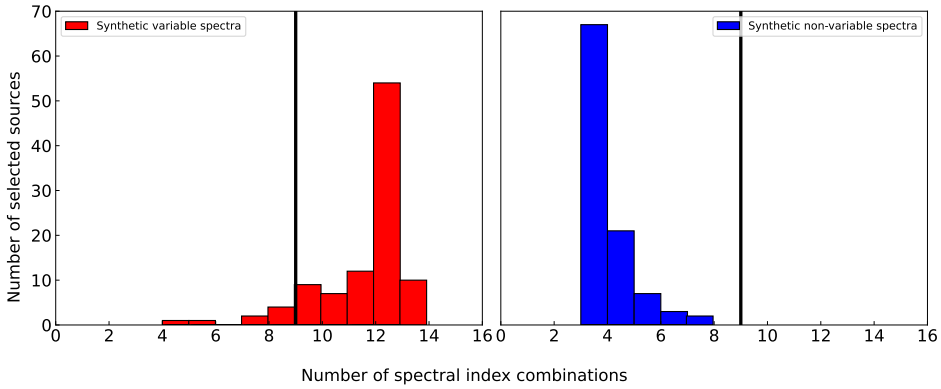

Figure 2.5: Histogram showing how many of the synthetically generated variable and non-variable spectra fall in the *variable* or *non-variable* area. We use these histograms to define the minimum number of *variable* areas inside the index-index plots in which one spectrum needs to fall to be considered *variable* (threshold). Similarly for the *non-variable* spectra.

Threshold

Once we define the variable and non-variable areas, we generate a histogram that includes the indices for all 200 spectra. And it gives us information on how many of the 15 *variable areas*, each of our spectra falls into (see Figure 2.5).

We defined variability threshold in 9 of 15 index-index plots, because 87% of the synthetic variable spectra fall in at least 9/15 *variable* areas, and 100% of the non-variable synthetic spectra fall in *non-variable* areas. Thus, any brown dwarf that is located in more than 9 index-index plots in the *variable areas* is considered a variable candidate. The spectra found in less than 9 index-index plots inside *variable* areas are considered a non-variable candidate.

The Python code to find L4–L8 brown dwarf variable candidates using the spectral indices presented in this work is publicity available and ready to be used in `https://github.com/ntlucia/BrownDwarf-SpectralIndices`.

2.2.3 Validation method

Once robust areas were defined within the index-index plots, we were able to use our spectral indices method to identify variable early- to mid-T brown dwarf candidates. We used a sample of 75 brown dwarfs with a single epoch spectrum, low resolution near-infrared (0.7–2.5 μm) spectra from the SpeX/IRTF

spectral library [1] (R between 75-120) with spectral types between L4 and L8 since they are within 2 spectral sub-types of LP261-75B (L6).

We show the details of the L4-L6 sample in Table A, and the record of our variability results using our spectral index method, concluding in 38 of the 75 L-dwarfs being candidate variables (See Figure 2.6). This value represents the $\sim 51\%$ variability fraction in our L4-L8 sample.

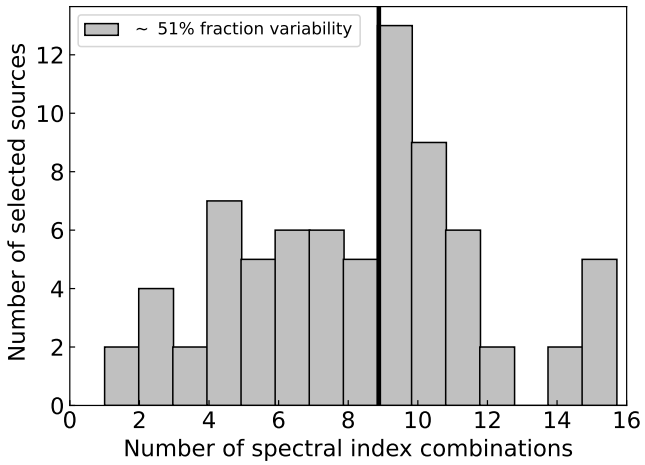

Figure 2.6: Validation histogram applying the spectral index method to the sample of 75 brown dwarfs, indicating the number of objects falling in the variable regions.

In addition, for brown dwarfs with records in the variability literature, we also add the respective citations and their description of their variability status. In total, 21 objects have been studied photometrically in the literature, of which 11 are presented as variables (Section B.1.1). We confirm 8 as non-variables in literature and with our method (Section B.1.2). Three objects present marginal variability or discrepant variability in the literature and our method reports them as non-variables (J0103-3801, J0820+4500, and J2148+4003 - Section B.1.2). One only the literature variables is found by our method as a non-variable (J1010-0406 - Section B.1.2). In total, we reported 24 new variable candidates (See Section 4.3 - Oliveros-Gomez, N., et. al, submitted).

[1] SpeX/IRTF spectral Library: https://cass.ucsd.edu/~ajb/browndwarfs/spexprism/html/ldwarf.html

2.2.4 Results and Discussion

In this Section, we discuss the results obtained and the relevance for future brown dwarf variability studies.

Recovery Rates

From the sample of 75 L4–L8 brown dwarfs with IRTF/SpeX spectra, a subsample of 23 brown dwarfs was monitored for variability studies in the literature (see Table in Appendix A). From those 23 objects, 12 are known variables (see Appendix B.2.1), and the other 11 are known non-variables (see Appendix B.2.2). Our spectral index method found 11 of the 12 known variables, as variable candidates. However, one of them, J1010-0406 (Cruz et al., 2003), was classified as non-variable by our spectral indices as it was found in a *variable* area in only 6 out of 15 index-index plots. This is the only false negative of our sample. Therefore, the recovery rate for variable L4–L8 brown dwarfs for the spectral indices presented here is $\sim$ 92%, and the false negative rate is $\sim$8% (1/12 objects).

For the 11 known non-variables, we obtained that all of them were flagged as non-variables by our spectral indices. Thus, our spectral indices are able to recover 100% of all the non-variable brown dwarfs, demonstrating to be a useful tool to rule out the most likely non-variable brown dwarfs. This is particularly important to conduct successful rotational modulation campaigns of brown dwarfs, especially in this spectral range (L4–L8) in which not all brown dwarfs show significant photometric or spectro-photometric variability. In this work, we provide the list of the most likely variable L4–L8 brown dwarfs according to our spectral indices in Section B.2.1, and the list of L4–L8 brown dwarfs to avoid in monitoring campaigns in Section B.2.2.

Variability Fraction

We estimate the variability fraction in the L4–L8 spectral range using the spectral indices introduced below, over the sample of 75 L4–L8 brown dwarfs in the IRTF/SpeX spectral library, assuming that in fact, all brown dwarfs flagged as variables by our indices are indeed variable. We compare the variability fraction obtained with our index method to the fraction obtained by other brown dwarf variability surveys in the literature.

In this work, we found that 12 out of the 75 are known variable candidates, flagged as variables by our indices (Section B.1.1). In addition, our indices found 27 new variable candidates for which no variability information was available in the literature (Section 4.3 - Oliveros-Gomez, et. al., in prep). In total, our indices found 38 L4–L8 variable candidates out of the 75 L4–L8

brown dwarfs with IRTF/SpeX spectra (51%). In the literature, only 11 of the 75 are confirmed by variability surveys as variable, bringing the minimum variability fraction to 14% for L4–L8 dwarfs. We follow the same method as Burgasser et al. (2003) to estimate the maximum variability fraction using a Poisson distribution. We use as the mean of the distribution the percentage of variable candidates found by our indices (51%), and the minimum variable fraction (14%) as the minimum of the distribution. We integrated the probability until reaching 0.68 (1-σ limit) which give us the upper limit for the variability fraction. Following this procedure, the variability fraction estimated for L4–L8 dwarfs is 51^{+4}_{-38}%.

We compare this variability fraction that we obtained with our indices to those calculated by ground-based (Radigan et al., 2014) and space-based brown dwarf variability surveys (Buenzli et al., 2014; Metchev et al., 2015). Radigan et al. (2014) performed a brown dwarf variability survey on 57 L, L/T, and T brown dwarfs using the Du Pont 2.5 m telescope at Las Campanas Observatory and the Canada–France–Hawaii Telescope on Maunakea. Radigan et al. (2014) obtained a variability fraction of 60^{+22}_{-18}% for brown dwarfs outside the L/T transition (L9.0-T3.5), although they do not report a specific variability fraction for the L4–L8 spectral range, this fraction is consistent to that estimated in this work.

Finally, we compare our results to the variability fraction obtained by Buenzli et al. (2014) and Metchev et al. (2015) using the HST/WFC3 instrument and the Spitzer telescope, respectively. Buenzli et al. (2014) monitored during two HST orbits a sample of 22 L, L/T, and T-dwarfs, and found that 4 dwarfs in the range L5-L8 showed significant or tentative variability out of the 12 dwarfs observed in that spectral range (∼33%). Metchev et al. (2015) using the [3.6] and [4.5] Spitzer channels, monitored a sample of L, L/T, and T-dwarfs, from which 16 were in the L4–L8 spectral range. Eight out of the 15 L4–L8 brown dwarfs were classified as a variable (∼50%). After correcting for sensitivity, Metchev et al. (2015) found that 80^{+20}_{-27}% of L dwarfs show variability amplitudes higher than 0.2%. Within uncertainties, our variability fraction is in agreement with the variability fraction estimated by Radigan et al. (2014), Buenzli et al. (2014) and Metchev et al. (2015).

Physics behind the index method

Our spectral indices compare the wavelength ranges of the HST/WFC3 spectrum of LP 261-75b which vary the most, and the ranges that vary the least as the object rotates (see Section 2.1). As shown in Figure 2.2 the wavelength ranges that vary the most are between 1.22 and 1.25 μm in J-band, and between 1.64 and 1.67 μm in the H-band, and those that vary the least are close to the water band at 1.4 μm (1.375-1.405 μm and 1.545-1.575 μm). To under-

stand why certain wavelength ranges show higher flux variations than others, we use the contribution functions predicted for an object of similar effective temperature and surface gravity by radiative-transfer models (Saumon, Marley, 2008). In Figure 2.7 we show the pressure levels probed by HST/WFC3 and the G141 grism for a field L6.0 brown like LP 261-75 b (T_{eff} = 1500 K, log g = 4.5, Bowler et al. 2013) according to radiative-transfer models (Saumon, Marley, 2008). Therefore, the greater variability in some spectral ranges than others is related to the area of the atmosphere being studied and the behavior of clouds at those altitudes.

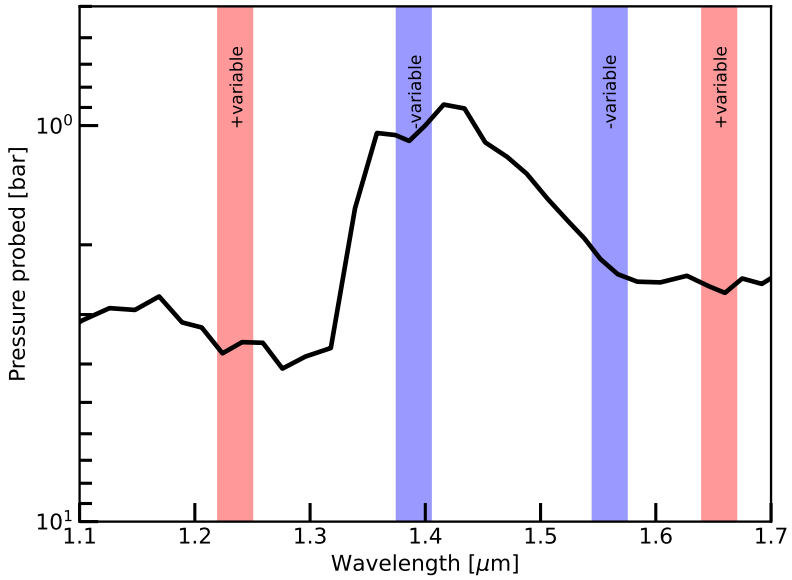

Figure 2.7: Pressure levels trace by the HST/WFC3 + G141 wavelength range in the atmosphere of LP 621-75b.

As observed in Figure 2.7, the most variable wavelength ranges in the *J*- and *H*-bands trace higher pressure levels (deeper) in the atmospheres of mid-L dwarfs. The 1.22–1.25 μm region traces the atmosphere of LP 261-75b at 3.64 mbar, and the 1.64-1.67 μm region traces the atmosphere at 2.60 mbar. The least variable regions of the spectrum between 1.375-1.405 μm and 1.545-1.575 μm, trace the 1.04 mbar and 2.27 mbar pressure levels, respectively. The most variable areas in the *J*- and *H*-bands are tracing a thicker and deeper cloud layer which might introduce higher variability amplitudes in localized wavelength ranges of the HST/WFC3 spectra. On the other hand, the pressure levels traced by the least variable regions are more superficial in comparison, with less cloud coverage present at those atmospheric levels (see Figure 2.8), which might probably explain the lower variability measure on those ranges.

As observed in Figure 2.8, and in Figure 2.9 for a qualitative representation, the most variable regions of the J- and H-bands trace also pressure levels with more cloud coverage, potentially explaining the higher variability measure on those wavelength ranges.

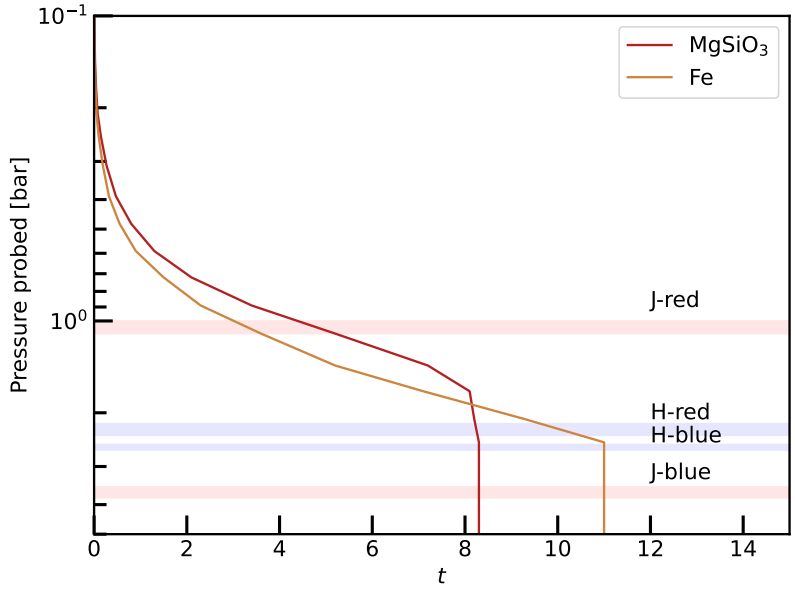

Figure 2.8: Condensate volume mixing ratio in the model plotted as a function of model pressure.

Beyond Brown Dwarf Variability

Brown dwarfs share colors and effective temperatures with some directly-imaged exoplanets (Faherty et al., 2016). Particularly in the mid-to late-L spectral type range, a handful of directly-imaged exoplanets are found: β-Pictoris b (Lagrange et al., 2009), with a T_{eff} = 1650±150 K (Bonnefoy et al., 2014b). HIP 65426 b (Chauvin et al., 2017), with a $T_{eff} = 1500^{+100}_{-200}$ K (Chauvin et al., 2017). AB-Pictoris b (Chauvin et al., 2005), with a $T_{eff} = 2000^{+100}_{-300}$ K and log g = 4.0±0.5 (Bonnefoy et al., 2010). Finally, kap And b (Carson et al., 2013) with a $T_{eff} = 1900^{+100}_{-200}$ K (Bonnefoy et al., 2014a).

Time-resolved spectroscopic data provides a wealth of information about the atmospheric dynamic and composition of brown dwarfs. Brown dwarf spectroscopic variability is most likely due to heterogeneous cloud structures at different pressure levels of the atmospheres of brown dwarfs that evolve within several rotations (Apai et al., 2017). Using radiative-transfer models (Saumon, Marley, 2008) we can infer which types of clouds are introducing the variability

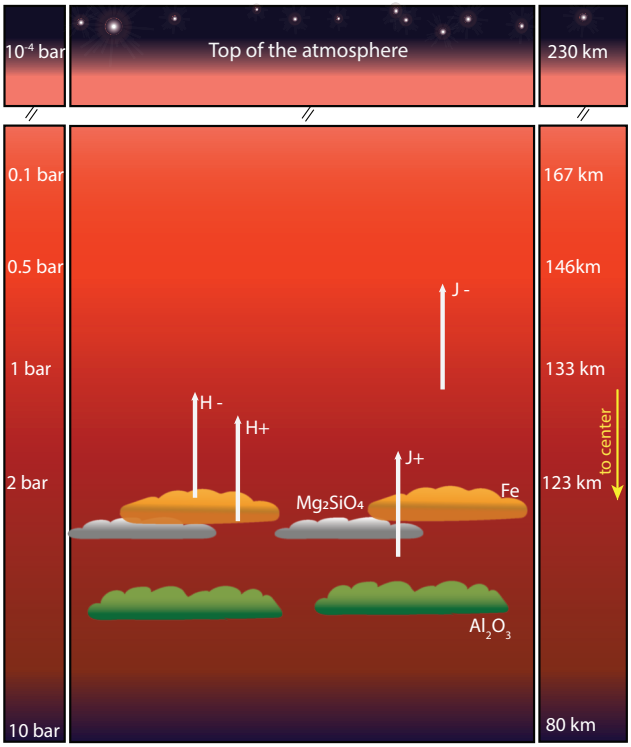

Figure 2.9: Representation of the vertical cloud structure of LP 261-75b and brown dwarfs of similar spectral types. We indicate where the Fe, Mg_2SiO_4, and Al_2O_3 clouds condensate, and the pressure levels traced by each wavelength range relevant for some of our spectral indices.

found at those pressure levels (Yang et al., 2016; Manjavacas et al., 2021). In addition, if we monitor spectroscopically the object during several rotations, we can infer the map of its surface to reconstruct the atmospheric characteristics (spots and/or bands) that are shaping the light curve produced at different wavelengths (Karalidi et al., 2015; Luger et al., 2019a). Time-resolved spectroscopic campaigns have been performed for several dozens of brown dwarfs (Buenzli et al. 2014; Radigan et al. 2014; Metchev et al. 2015; Biller et al. 2018; Manjavacas et al. 2018; Vos et al. 2020, among others), but only for one system of directly-imaged exoplanets HR 8799bc (Apai et al., 2016; Biller et al., 2021) for which only upper levels of variability could be set, due to the low signal-to-noise of the data. Luckily, after the successful launch and commissioning of the *James Webb Space Telescope*, we are obtaining unprecedented quality spectra for directly-imaged exoplanets. Spectroscopic variability of these objects will provide extremely valuable information about the dynamics, clouds, and structure of directly-imaged exoplanets, nonetheless, to ensure the success of the first rotational monitoring campaigns for directly-imaged exoplanets,

spectral indices like those presented in this work might be extremely helpful to pre-select the most likely candidates to show variability. Until now no systematic method to pre-identify variable L-dwarfs was available, thus these spectral indices will very likely save hours of valuable telescope time.

2.3 Method to identify variable T-dwarfs

Part of this thesis work has already been published in Oliveros-Gomez et al. (2022). However, we consider it convenient to explain in this thesis the details of the creation of the method that we designed to test near-infrared spectral indices to preselect the most likely variable mid- and late-T dwarfs, which overlap in effective temperatures and colors with directly imaged exoplanets.

2.3.1 Spectroscopic observations

The data used for our analysis were obtained on 2011 July 7 with the infrared channel of the WFC3 on board the HST and its G141 grism, providing spectra covering a wavelength range between 1.10 and 1.70 μm (GO-12314, GO-70170; PI: D. Apai). These spectra were published by Buenzli et al. (2012).

The observations were performed using a 256 × 256 pixels subarray of the WFC3 infrared channel, with a field of view of approximately 30" × 30". A SPARS25 was used in 1024 ×1024 pixels readout mode with 11 reads per exposure. Each sub-readout has an exposure time of 22.34 s, after an initial first short read at 0.27 s, allowing for a maximum exposure number of 27,000 counts, which is below the average detector capacity. A total of 54 spectra were acquired over six consecutive HST orbits spanning 8.57 hr. In each orbit, we obtained nine spectra with a cadence of 241.99 s. The resolution of the spectra is ∼100, and the signal-to-noise ratio is ∼124.

Observations for 2MASS J22282889–431026 (J2228-4310) were obtained with the Wide Field Camera 3 instrument. J2228-4310 is a T6.5 brown dwarf (Burgasser et al., 2003) at a distance of d = 10.64 ± 0.79 pc (Faherty et al., 2012). Buenzli et al. (2012) estimated Teff = 900 K and log g = 4.5-5.0, typical of T dwarfs. J2228-4310 is variable with a period of 1.43 hr and a peak-to-peak amplitude of 1.85 ± 0.07% in the [4.5] Spitzer channel, 1.85 ± 0.07% in the J band, 2.74 ± 0.11% in the *H*-band, and 5.3 ± 0.6% in the H_2O band (Buenzli et al., 2012). Metchev et al. (2015) measured its variability amplitude as 4.6% in the Spitzer [3.6] band and an amplitude of 1.6% in the [4.5] channel. Buenzli et al. (2012) measured a phase shift of 89-38 ± 13-18° between the *J*- and *H*-band HST/WFC3 light curves, which was interpreted as evidence of large-scale longitudinal-vertical structures. The variability amplitudes and

phase shifts were confirmed by Yang et al. (2016) in data obtained four years later, which indicates that the light curve of J2228-4310 is relatively stable on long timescales.

Their light curve showed a variability amplitude between 1.45% and 5.3%, depending on the wavelength range of the J2228-4310 used to create the light curve (Figure 2.1 - right). In the near-infrared light curve, each data point is a near-infrared time-resolved spectrum itself (see Figure 2.2 - right).

2.3.2 Method

Following the process described in Section 2.1, we consolidated the spectral ranges to create two spectral indices: one to measure the variability in the *H*-band and the other in the *J*-band, both of which are calculated with Equation 2.1. In addition, we created two other indices, comparing the *J*- and *H*-bands with each other, one corresponding to the index color, and the other being a ratio between the *H*- and *J*-band, to compare the two most variable bands in our spectrum. Finally, we supplemented our indices with two other indices published in Bardalez Gagliuffi et al. (2014) were used *J*-slope and *J*-curve, focusing on the band that has the highest variability, according to the residuals in Figure 2.2 - right. The six indices examined are described in Table 2.2.

Spectral index	Numerator Range[2] (μm)	Denominator Range[3] (μm)	Feature	Reference
H/J	1,51-1,62	1,205-1,315	Comparison of H-band and J-band	(1)
J-H	1,205-1,315	1,51-1,62	J-H Color index	(1)
H	1,59-1,62	1,64-1,67	Difference variability in H-band	(1)
J	1,22-1,25	1,15-1,18	Difference variability in J-band	(1)
J-slope	1.27-1.30	1.30-1.33	1.28 μm flux peak shape	(2)
J-curve	1.26-1.29	1.14-1.17	Curvature across J-band	(2)

Table 2.2: Boundary ranges used for the creation of the spectral indices. References: (1) This paper, (2) Bardalez Gagliuffi et al. (2014)

We measured the six spectral indices for the 54 HST/WFC3 NIR spectra of J2228-4310. We compared these measurement indices in index-index plots (see Figure 2.10). As observed in Figure 2.10, we see the values of the indices for the most variable and least variable spectra clustering in specific areas of the index-index plots. Among the initial index-index plots, we selected 12 that better segregated the most and least variable spectra of J2228-4310, and did not resemble any of the other plots. To identify the regions of the index-index plots in which the variable mid- and T-dwarfs would be located, we color-coded the points with higher (red) to lower variability amplitudes (blue) spectra, as shown in Figure 2.10.

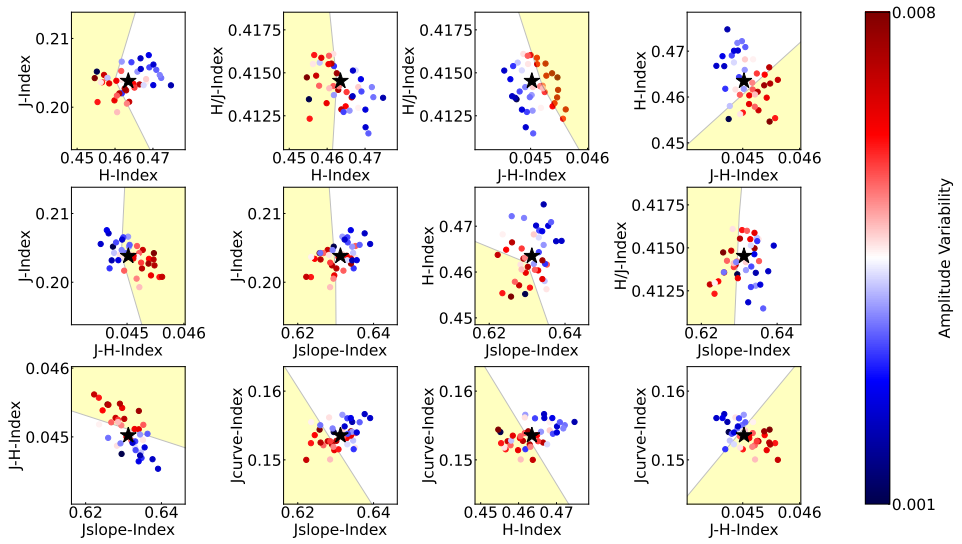

Figure 2.10: Index-index plots comparing the designed spectral indices to find mid- and late-T brown dwarf variables. The blue points correspond to the spectra that show the least variability amplitude (close to the 1.0 of the light curve in Figure 2.1 - right), and the red corresponds to the most variable spectra (close to the 1.007 or 0.992 of the light curve in Figure 2.1 - right). The black star in the center corresponds to the indices calculated for the template spectrum with no variability. We show the provisional variable regions (in yellow) using the indices calculated only with observed spectra.

Areas of high variability likelihood in index-index plots

The points in Figure 2.10 corresponding to the most variable spectra (red points) coincide with the maximum (or minimum) of the combined near-infrared light curve of J2228-4310, and the least variable spectra are those corresponding to the points of the light curve located near a value of 1.0, as shown in Figure 2.1 - right. From this analysis, we were able to visually identify the regions where most of the variable spectra are in the index-index plots, as shown in Figure 2.10 (yellow areas). The variability regions presented in Figure 2.10, are limited to the 54 spectra available for J2228-4310. Thus, to provide robust regions of high likelihood of variability in the index-index plots, we generated synthetic spectra, similar to the HST/WFC3 near-infrared spectra, using a Monte Carlo simulation. For that purpose, we redefined each point of the spectrum using a Gaussian random number generator. The mean value of the Gaussian is the original flux in the spectrum, and the standard deviation is the uncertainty of each point of the sample spectrum.

We generated two different sets of synthetic spectra: the first set is similar to the most variable spectrum in the J2228-4310 light curve (in the light curve

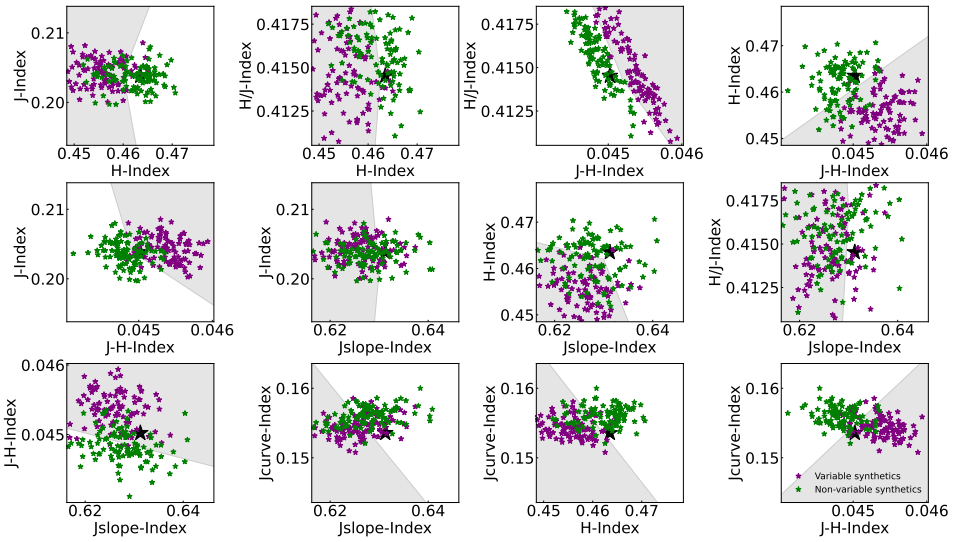

Figure 2.11: Index-index plot as in Figure 2.10 including the value of the indices calculated for the synthetic spectra created using the most variable spectra of J2228-4310 (purple stars), and the least variable J2228-4310 spectra (green stars). We show the updated new variable regions (in grey) using the synthetic spectra.

in Figure 2.1 - right) at 0.3 hr, normalized flux ≈ 0.99024), and a second set from the least variable spectrum in the object's light curve. The least variable spectrum of J2228-4310 is the one with a relative flux value closest to 1.0 in the target's light curve (in Figure 2.1 - right at 3.4 hr, normalized flux = 0.99997). We generated 100 new synthetic spectra using the most variable spectrum of J2228-4310, and 100 new synthetic spectra using the least variable spectrum of J2228-4310. With these 200 new synthetic spectra, the six indices are calculated for each spectrum and plotted alongside the initial 54 spectra of J2228-4310 in the index-index comparison plots (Figure 2.11). Using the newly generated synthetic spectra, we refine the initial variable areas in the index-index plots. The new regions of variability are shown in Figure 2.11.

Candidate selection

Using the areas defined previously, it is possible to denote variability candidacy based on the number of times a spectrum is found within the regions of variability. Figure 2.12 shows two histograms with the frequency in which spectra are identified as variable or non-variable in a given number of index plots. We found that 70% of the synthetic spectra generated using the most variable J2228-4310 spectrum are within the variable regions in at least 11 of the 12 index-index plots (upper panel). For the case of the synthetic spectra

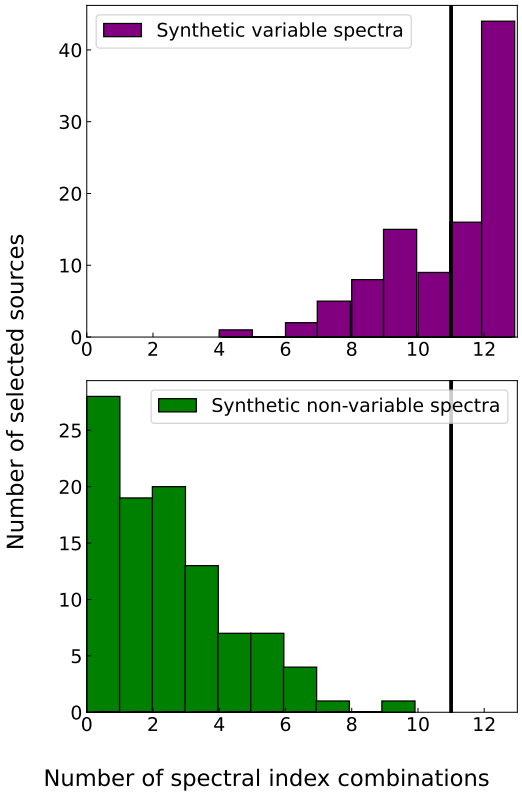

Figure 2.12: Upper plot: Histogram showing how many synthetic variable spectra fall in variable areas of index-index plots. The histogram shows that most of the variable synthetic spectra fall at least in 11 variable areas in the index-index plots. Bottom plot: Histogram showing how many synthetic non-variable spectra fall in variable areas. The histogram shows that most of the non-variable synthetic spectra fall in less than 10 variable areas. Thus, we mark the threshold on 11 plots to catalog an object as a variable candidate.

generated using the least variable J2228-4310 spectrum, we found that 100% of the spectra fall in the variable region in less than 9 of the index-index plots (lower panel). For this reason, we identify as *variable candidates* those found at least in 11 regions in our index-index comparison plots. This code to preselect T-dwarf candidate variables is available in GitHub[4]

2.3.3 Validation method

Once robust areas were defined within the index-index plots, we were able to use our spectral indices to identify variable mid- to late-T brown dwarf

[4]GitHub code: https://github.com/ntlucia/BrownDwarf-SpectralIndices

candidates.

We used all available near-infrared (0.7–2.5 μm) spectra from the SpeX/IRTF spectral library[5] (R$\sim$120) with spectral types between T5.5 and T7.5. We end up with 26 brown dwarfs with a single epoch spectrum. We test our spectral indices with brown dwarfs with spectral types between T5.5 and T7.5 since they are within one spectral type of J2228-4310 (T6.5). In this sample, we included the SpeX spectrum of J2228-4310 itself to confirm the validity of our method with spectra taken with other instruments different from WFC3.

In Table A.2, we show the details of the T5.5-T7.5 sample that we used to test our method. We calculated the indices for the 26 brown dwarfs, and created the index-index plots, concluding that 10 of the 26 T5.5-T7.5 dwarfs were selected by the indices as variable candidates. This represents a 38^{+4}_{-30}% variability occurrence for the T5.5 - T7.5 spectral sample considered in this study.

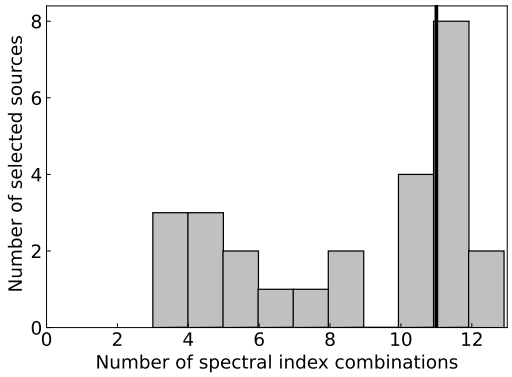

Figure 2.13: Histogram of the number of times each of the mid-to late-T dwarfs fall in the variability regions in each of the 12 index-index plots.

From the SpeX sample, ten objects have been monitored for variability in previous works (Radigan et al. 2014, Metchev et al. 2015). The only known variables, apart from J2228-4310 are J0050–3322 and J1047+2124. There are seven others of the T5.5-T7.5 sample that have been confirmed as non-variable or with amplitudes below noise level in previous works (Clarke et al., 2008; Radigan et al., 2014; Buenzli et al., 2014; Metchev et al., 2015).

In addition, two of the three previously known variables in our sample of SpeX spectra are flagged as variable candidates by our indices. Similarly, all seven known non-variables in our sample are flagged as non-variable objects by our indices. These results suggest that our spectral indices might be used to find variable mid- and late-T brown dwarf variables. These indices may be

[5] http://pono.ucsd.edu/~adam/browndwarfs/spexprism/html/tdwarf.html

crucial in the future to select cool directly-imaged exoplanets for variability studies.

2.3.4 Results and Discussion

Recovery Rates

Using our method, we find that 10 objects in the sample of 26 T5.5-T7.5 dwarfs were monitored for variability studies in the literature. Three of them were found to be variable (J2228-4310, J0050-3322, and J1047+2124 see in Appendix B, Section B.2.1), while the other seven are not variable (see in Appendix B, Section B.2.2). The index method presented before was able to recover two of the three known variable brown dwarfs (recovery rate of 67%). For the known non-variable brown dwarfs, our index method was able to recover all seven known non-variables (recovery rate of 100%), we found a single false negative, J1047+2124, which would suggest a false-negative rate of 12.5% (1/8). In addition, J1047+2124 is a borderline variable candidate, selected as a variable by 10/12 regions, and we decided to consider it as a "weak variable candidate". Further variability monitoring campaigns are needed to observe the new variable candidates and confirm the recovery rates of our index method.

Variability Fraction

Using the index method presented here over a sample of 26 mid and late-T dwarfs SpeX near-infrared spectra with spectral types between T5.5 and T7.5, and based on the assumption that the variable candidates are indeed variable, we aim at estimating the variability fraction given by our indices and compare it with other estimations in the literature.

We found that 10 of the 26 objects are variable candidates. This suggests a variability fraction of 38^{+4}_{-30}% for this spectral range. Of the 10 variable candidates, only 2 are known variables (J2228-4310 and J0050–3322). We followed the same method as in Burgasser et al. (2003) to estimate the uncertainties of the variability fraction using a Poisson distribution. Considering that the total number of objects in our sample is 26, the mean of the distribution is 10 (variable candidates found by our indices), and the minimum variable fraction of our sample is $2/26 \sim 8\%$. We integrated the probability of the distribution until reaching 0.68, equivalent to 1-σ Gaussian limits. We estimated the variability fraction of our sample in 38^{+4}_{-30}% according to our indices. However, taking into account the false negative rate of the indices, the true fraction of variability could be slightly higher.

We compared this variability fraction with the results of ground-based (Radigan et al., 2014) and space-based (Buenzli et al. 2014, Metchev et al. 2015) surveys to understand if the variability fraction reported in this work is consistent with those. Radigan et al. (2014) monitored a sample of 57 L, L/T, and T-dwarfs in the J-band using the Du Pont 2.5 m telescope at Las Campanas Observatory and the Canada–France–Hawaii Telescope on Mauna Kea. Radigan et al. (2014) studied 15 dwarfs with a spectral type later than T5.5, and reported significant variability for three of them, implying a variability fraction of ∼20%. Because of the limited stability and sensitivity of the ground-based data, this 20% should probably be considered as a lower limit rather than an intrinsic variability fraction. Similarly, Buenzli et al. (2014) monitored a sample of 22 L5 to T6 dwarfs with the *Hubble Space Telescope/Wide Field Camera 3* in the J- and H-bands, finding six brown dwarfs with confident variability and five brown dwarfs with tentative variability. This leads to a variability fraction between 27–50%. In addition, Metchev et al. (2015) monitored a sample of 44 L3 to T8 dwarfs using the *Spitzer* Space Telescope in the [3.6] and [4.5] channels. Metchev et al. (2015) monitored five T-dwarfs with spectral types later than T5.5, finding significant variability for two of them (∼40%). Metchev et al. (2015) concluded that most of the T-dwarfs in their sample showed low-level variability (>0.2%).

The difference in variability fractions is most likely due to three factors: (1) the difference in sensitivity between ground and space-based telescopes, (2) the wavelength range at which each sample was observed, and (3) the different time scales: the *Spitzer* observations were usually much longer than what is possible from the ground. The J-band traces deeper pressure levels of the mid to late-T atmospheres (∼5 bar, Yang et al. 2016, see their Figure 19) than the [3.6] and [4.5] *Spitzer* bands (∼0.2 bar and ∼0.6 bar, respectively, Yang et al. 2016). Given that most of the cloud deck is expected to be at pressures above ∼1 bar (Yang et al., 2016), in principle, we do not expect a high variability in the *Spitzer* channels. A visual representation of the atmospheric structure of a similar spectral type object, 2M0050-3322, can be found in Manjavacas et al. (2022), their Figure 19. Nevertheless, the sensitivity of the *Spitzer* Space Telescope is higher than ground-based observatories. The variability fraction we report on this work, 38^{+4}_{-30}%, is consistent to the *Spitzer* variability fraction reported by Metchev et al. (2015). We confirm the regions of variability in the spectrum with respect to the depths of the atmosphere, as shown in Figure 2.14.

Physics behind the index method

The spectral indices presented in this work compare the wavelength ranges of the J- and H-bands of the HST/WFC3 spectra of 2M2228 that vary the most

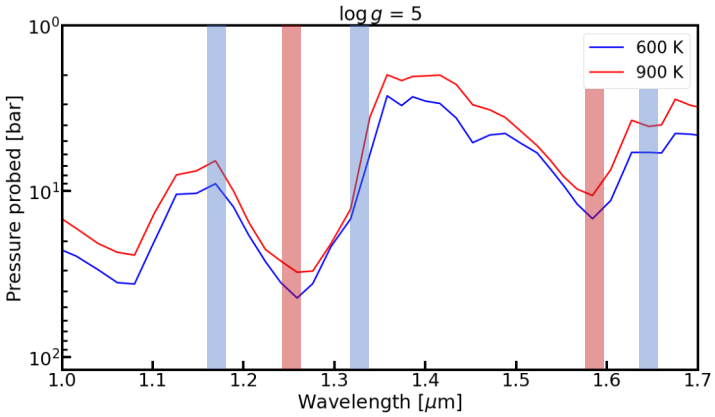

Figure 2.14: Pressure levels probed by the HST/WFC3 + G141 wavelength range for T dwarfs with temperatures of 900 K (red line) and 600 K (blue line), covering spectral types T5-T8 according to radiative transfer models. We shade in red the most variable wavelength ranges of the spectra, which were used as numerators for the J and H indices. We shade in blue the least variable wavelength ranges of the spectra, which were used as denominators for the J, H, and J-slope indices.

with the wavelength ranges that vary the least as the object rotates. The most variable ranges of the *J*- and *H*-bands are usually located around the maximum of the bands (see Table 2.2), and the least variable is usually located at the wings of the bands (see Table 2.2). In addition, two of our indices compare the *J*- and *H*-band flux between them. To understand the reason why certain wavelength ranges show higher flux variations than others, we use the vertical structure predicted for an object of similar spectral type and surface gravity to 2M2228 by radiative-transfer models (Saumon, Marley, 2008) in Yang et al. (2016). In Figure 2.7 we show the pressure levels probed by HST/WFC3 and the G141 grism, similar to the contribution functions presented in Yang et al. (2016), their Figure 18. As seen in Figure 2.7, the peaks of the *J*- and *H*-bands around 1.25 μm and 1.58 μm (shaded in red), respectively, probe the deepest layers of the atmosphere of a mid to late-T dwarf that we are able to trace. The peak of *J*-band probes the 30–40 bar level, and the *H*-band peak probes the 10–20 bar level. In the meantime, the wings trace upper layers: the $\sim$10 bar level is traced with wavelengths around 1.17 μm and 1.32 μm for the *J*-band, and the $\sim$6 bar level is traced with wavelengths around 1.65 μm in the *H*-band (see Figure 2.7, shaded in blue). As discussed in Section 2.1, these wavelength ranges covered by the wings barely change during the rotational period of 2M2228.

In addition, the condensate mixing ratio (mole fraction) of the clouds present in 2M2228's atmosphere (Al_2O_3, Fe, and Mg_2SiO_4 clouds) is predicted

to decrease with decreasing pressure (see Yang et al. 2016, their Figure 19). Thus, as we probe higher levels in the atmosphere of 2M2228, we expect to have less dense clouds, and therefore potentially less variability too. This scenario would explain why the variability observed in the wings of the J- and H-band is smaller than in their respective peaks. Finally, the high signal-to-noise of the HST/WFC3 near-infrared spectra is enough to quantify the differences in variability amplitude, and thus to design the spectral indices that allowed us to identify new >T5.5 variable candidates (see Section 4.3 of Oliveros-Gomez et al. 2022) with a single-epoch near-infrared spectrum.

Top-of-the-atmosphere features

In contrast to early-T dwarfs, mid- and late-T dwarfs show in general relatively low variability amplitudes (Radigan et al., 2014; Metchev et al., 2015). Variability surveys from the ground and space-based facilities have not found variability amplitudes above the 2% for mid- and late-T dwarfs, with the only exception of Ross 458 c (Manjavacas et al., 2019). Nevertheless, Metchev et al. (2015) showed that most mid- and late-T dwarfs do show low-level variability (>0.4%). Even though few mid- and late-T dwarfs have been monitored for spectrophotometric variability with space-based facilities that provide high signal-to-noise data, they are expected to show bands and spots as Solar System planets do, according to General Circulation models (GCMs) (Tan, Showman, 2021). GCMs provide instantaneous model maps for the top-of-the-atmosphere thermal flux, and predict the most likely light curve for such an object. The variability amplitude predicted for a T-dwarf of a similar spectral type to 2M2228 (2M0050–3322, Manjavacas et al. 2022) is about ∼1% for an edge-on object. The predicted variability amplitude decreases to about 0.2% for a pole-on object. GCMs predict a band near the equator driven by the radiative feedback of MnS and Na_2S clouds. A more extended sample of mid- and late-T dwarfs with high signal-to-noise spectrophotometric monitoring data from space-based facilities would help constrain the properties and dynamics of mid- and late-T dwarfs and would allow to confirm the prediction of GCMs.

Analogs to Cool Directly-Imaged Exoplanets

Brown dwarfs are analogs to directly-imaged exoplanets, as they share effective temperatures, colors, and sometimes surface gravities and masses (e.g. Faherty et al. 2016). This is the case of the 51 Eridani b directly-imaged exoplanet (600–750 K, Macintosh et al. 2015), HD 19467 b (1040±40 K, Wood et al. 2019), Gl 758 b (600–750 K, Bowler et al. 2018), or HD 4113C (500–600 K, Cheetham et al. 2018), which show significant variability of HR8799bc Biller

et al. (2021), among others. Thus, a comprehensive atmospheric characterization of the technically easier-to-observe isolated T-dwarfs might shed light on the atmospheric structures of cool directly-imaged exoplanets (Apai et al., 2017). High signal-to-noise spectro-photometric time-resolved data provide information about the variability introduced at different pressure levels of the atmospheres of these objects, which allows us to understand at which pressure levels most of the heterogeneous clouds introducing the measured variability are found, using radiative-transfer models (e.g. Yang et al. 2016). Continued monitoring of a few rotational periods of these objects allows us to produce a map of its surface and reconstruct which atmospheric structures (band and/or spots) have most likely produced its light curve at different pressure levels.

Mapping Codes like *Stratos* (Apai et al., 2013), *Aeolus* (Karalidi et al., 2015) or *Starry* (Luger et al., 2019b) allow us to generate 2D maps of a given light curve expanding over 2-3 rotational periods. Such a detailed atmospheric characterization is yet technically challenging for directly-imaged exoplanets (Apai et al., 2016). Nevertheless, with the advent of the first scientific data from the just launched *James Webb Space Telescope*, we will be able to characterize more cool directly-imaged exoplanets. The spectral indices presented in this paper will be of special importance since they will allow the community to pre-select the most likely variable T-dwarf type-like directly imaged exoplanets to be monitored for spectro-photometric variability. Since until now, no systematic method to pre-identify variable T-dwarfs exists, these spectral indices will very likely save hours of precious telescope time.

Chapter 3

Spectral Synthetic Models for L- and T- dwarfs

We focus on the modeling of synthetic spectra to describe two of the brown dwarfs used to develop our spectral indices in Chapter 2: LP 261-75b (L6), described in Chapter 2.2, and J2228-4310 (T6), described in 2.3.

Our goal is to have a better understanding of some physical and chemical phenomena that occur in the interior of brown dwarfs. Generally speaking, as they cool along their spectral sequence, lower temperatures allow more complex molecules to form, resulting in cloud condensation. When the temperature is cool enough (< 2000 K) the large condensate grains cannot remain suspended in the atmosphere and begin to sink below the observable photosphere, allowing methane and molecular hydrogen in the gas phase to become the dominant absorbers.

For L-dwarfs, clouds are expected to form in an optically thin region of the photosphere where the effective temperature is $T_{\rm eff} > 1600$ K. As the temperature decreases, the clouds thicken and begin to fall deeper into the atmosphere (as they transition to T dwarfs - see Figure 1.3 as a horizontal branch). As the dust moves into the optically thick region of the atmosphere ($T_{\rm eff} < 1400$ K), the upper atmosphere cools rapidly and the conversion of CO to CH_4 begins along with near-infrared color reversal. While this seems to be a good description of the physical process, the color inversion is not enough.

The first studies to include clouds in spectral models were by Marley et al. (2002), who introduced the parameter f_{sed}, which defines the efficiency of sedimentation in relation to turbulent mixing. They propose values of f_{sed} $[0-3]$ for mid-L, $f_{sed} > 3$ for early-T, and almost $f_{sed} = \infty$ for mid- and late-T (cloud-free). However, the color variation process at the transition was still much slower than observed.

However, Burgasser et al. (2002) proposed to treat the interior not as uni-

form clouds, but as patches and holes, similar to the nearby cases of Jupiter and Saturn. The holes allow flow from the deeper, warmer layers to emerge. Brown dwarfs with fewer clouds will have bluer colors. The most significant difference between BD evolution calculations published in the last decade is in the treatment of the model's surface boundary condition, which connects the surface properties (Effective temperature - $T_{\rm eff,}$ and gravity - log(g)), to the interior model (Mass - M, Luminosity - L, Radius - R, and age), for example `Phoenix Code` (Witte et al., 2011).

We will now describe some of the models we use to generate synthetic spectra of these types of brown dwarfs, mainly taking into account the difference between cloudless and cloudy. Mainly those that had a more accurate fit to the observed spectra. Since we implemented others that were not close to the expected results, we will not take them into account.

3.1 Cloudless models

Although it has been shown observationally that T-type dwarfs might have clouds in their deeper atmosphere, leading to measurable variability (Radigan 2014, Buenzli et al. 2014, Radigan 2014), the models that best fit these objects are models that do not take clouds into account (Lueber et al., 2022).

3.1.1 ATMO

ATMO is a library containing spectral models with solar metallicity as well as evolutionary models for cool brown dwarfs ($< 1000K$) and luminous giant exoplanets (Phillips et al., 2020). These are generated by a 1D radiative-convective equilibrium code. It has surface boundary conditions to calculate the interior structure and time evolution for objects with masses between 0.001-0.075 $M_{\odot}$. They contain one grid for spectra with equilibrium chemistry (CEQ) and two using non-equilibrium chemistry due to vertical mixing (NEQ-strong and NEQ-weak), all three calculated in a self-consistent manner with the pressure and temperature structure of the atmosphere.

ATMO takes into account 22 atomic and molecular species, where each spectral line is broadened including Doppler broadening and pressure broadening with H_2 and He collisions. This generates a grid of pressures and temperatures, with 40 pressure points spaced logarithmically from $10^{-9} - 10^{3}$ bar, and 20 temperature points spaced logarithmically in the 70-3000 K range.

The interior structure calculations and evolutionary models are based on the Lyon stellar evolution code and are described in detail in these papers: Chabrier, Baraffe (1997), Baraffe et al. (1998) and Baraffe et al. (2003). Which use libraries from the model atmosphere `Phoenix code`.

3.1.2 PetitCODE cool

PetitCODE cool is a library of modeled spectra that computes a grid of 1D radiative-convective atmospheres. Emission spectra are calculated with the pressure-temperature iterator code and a spectral emission calculator for planetary atmospheres (`PETIT`), assuming chemical equilibrium (Mollière et al., 2015).

This library uses an opacity database comprising atomic lines, molecular lines, and continuous opacities from ultraviolet to infrared wavelengths. It takes into account only absorption processes. Calculations are performed on a pressure-temperature grid with 10 grid points in pressure ranging from 10^{-6} to 10^{3} bar (spaced equidistantly in logarithmic space). And points ranging from the effective temperature of 500 to 1000 K, also equidistantly spaced in logarithmic space.

Opacities with effective temperatures $T_{\text{eff}} < 270$ K are only calculated up to pressures of $P = 1$ bar. For $270 < T_{\text{eff}} < 670$ K only up to $P = 10$ bar and for $670 < T_{\text{eff}} < 900$ K only up to $P = 100$ bar. It also makes variations in metallicity [-0.5, 0.0, 0.5, 1.0, 2.0], since in high metallicity objects cloud effects can become important, especially if appreciable amounts of silicate, iron, or corundum condensates can form.

3.1.3 Sonora

Bobcat

Sonora Bobcat has models of temperature-pressure profiles, upper atmospheric emergent spectra, thermal evolution, photometry, and in addition, precipitation chemical equilibrium tables used to calculate the models (Marley et al., 2021).

This library is used for modeling cloudless objects (such as T-type brown dwarfs, or exoplanets with little variability). Models are calculated on a grid with surface gravities $3.25 < \log(g)(\text{cgs}) < 5.5$ and effective temperatures $200 < T_{\text{eff}} < 2400$ K. The steps in T_{eff} vary from 25 K to 1000 K and the steps in log g are 0.25 or 0.5 dex. Some combinations of model grid parameters include additional gravity values. In addition, models are provided, for varying the metallicity among values of $[M/H]$ = -0.5, 0.0, and +0.5. All these grid values are calculated assuming chemical equilibrium, but in addition, *rainout* chemical equilibrium (not pure equilibrium) tables are included.

Cholla

The Sonora Cholla models (Karalidi et al., 2021) have the same principles taken into account as for Sonora Bobcat, where a grid of cloudless solar metallicity atmospheres for brown dwarfs and giant planets is available. Now, for this model package, we have a broad separation with key molecular species such as CH_4, H_2O, CO, and NH_3, including their non-equilibrium. The grid of this model covers atmospheres with effective temperatures of $T_{\rm eff} \sim$ [500 K, 1300 K], surface gravities of log(g) $\sim$ [3.0, 5.5] (cgs), and an eddy diffusion parameter of log($K_{\rm zz}$) = 2, 4 and 7 (cgs).

3.2 Cloudy models

Models that include clouds are somewhat more recent and tend to be a bit more complex due to the behavior of clouds in the interior of brown dwarfs. These are mainly used for objects such as L dwarfs, which exhibit the greatest variability, in terms of amplitude variations, which have been measured observationally (Buenzli et al. 2014, Radigan 2014, Metchev et al. 2015). In addition, they have also been recorded in both photometric (Apai et al. 2013, Karalidi et al. 2015) and spectral (Burgasser et al. 2010b, Lueber et al. 2022) model comparisons.

3.2.1 BT-Settl

BT-Settl is a model that can simulate stellar atmospheres of small stars and brown dwarfs Allard et al. (2003a), it produces synthetic spectra Using the `Phoenix` atmospheric code, with plane-parallel transfer energy, and the Mixing Length Technique. The grid covers atmospheres with $T_{\rm eff} \sim$ [400, 4000] K, and surface gravities log(g) $\sim$ [3.5, 5.5] (csg). Opacities are calculated for each [T,P]-point, taking into account the microphysical and convective characteristics Allard et al. (2013)

3.2.2 DRIFT-Phoenix

DRIFT-Phoenix is a package of grid models that combine the non-equilibrium, and stationary cloud model DRIFT (seed formation, growth, evaporation, gravitational settling, element conservation) with the model atmosphere code `Phoenix` (radiative transfer, hydrostatic equilibrium, mixing-length theory, chemical equilibrium) Helling et al. (2008). These models allow to be consistent between the calculation of cloud formation, radiative transfer, and feedback on convection and gas-phase depletion. Unlike other codes, Drift describes the formation of mineral clouds and allows the prediction of cloud details such as

particle size and composition. The grid covers atmospheres with effective temperatures $T_{\rm eff}$ ∼ [1000, 3000] K, surface gravities of log(g) ∼ [3.0, 5.5] (csg), and metallicities of $[M/H]$ ∼ [-0.6, 0.3] (Witte et al., 2011).

3.2.3 PetitCODE hot

PetitCODE hot is a grid model with the same behavior that PetitCODE cool (cloud-free or cloudy atmospheric models in chemical equilibrium) but now, including different levels of carbon to oxygen ratio (C/O). This model covers the atmosphere with effective temperatures $T_{\rm eff}$ ∼ [1000, 2600] K, surface gravities of log(g) ∼ [2.0, 5.0] (csg), metallicities of $[Fe/H]$ ∼ [-1.0, 2.0] and carbon-oxygen relation $[C/O]$ ∼ [0.25, 1.25] (Molaverdikhani et al., 2019).

Including C/O in these models with clouds is very important, since at low temperatures we find that the pressure level of the photosphere strongly influences whether the atmospheric opacity is dominated by water (for low C/O) or methane (for high C/O), or both (regardless of C/O). For hot carbon-rich objects, this pressure level determines whether the atmosphere is dominated by methane or HCN. Therefore this C/O ratio is an indicator of atmosphere composition species.

3.2.4 ForMoSA

ForMoSA is a Bayesian inference tool, that uses the ATMO version but includes processes that simulate the behavior of clouds (Petrus et al., 2023). According to the design of these models, adiabatic convective processes (Tremblin et al. 2016, Tremblin 2019) induced by out-of-equilibrium CO/CH_4 and N_2/NH_3 chemistry can reduce the temperature gradient in the atmosphere and reproduce reddening, without the need to include clouds.

These models have solar metallicity and take into account evolutionary models. In general, the grid covers atmospheres with effective temperatures of $T_{\rm eff}$ ∼ [800, 3000] K, surface gravities of log(g) ∼ [2.5, 5.5] dex, metallicities of $[M/H]$ ∼ [-0.6, 0.6], carbon-oxygen relation $[C/O]$ ∼ [0.3, 0.7] and effective adiabatic index γ ∼ [1.01, 1.05].

3.2.5 Saumon & Marley (2008)

Saumon & Marley models are a set of synthesized spectra that take into account clouds by means of the parameter $f_{\rm sed}$. Large values of $f_{\rm sed}$ correspond to rapid particle growth and large mean particle sizes. In this case condensates quickly fall out of the atmosphere, leading to physically and optically thin clouds. When $f_{\rm sed}$ is small, particles grow more slowly and the atmospheric condensate load is larger and clouds thicker.

This grid covers atmospheres with $T_{\rm eff} \sim [500, 2400]$ K, and surface gravities of $\log(g) \sim [3.5, 5.5]$ dex. The cloud model is fully coupled with the radiative transfer and the (P, T) structure of the model during the calculation of a model so that they are fully consistent when convergence is obtained.

3.3 SPECIES

The toolkit `species` allows the atmospheric characterization of directly imaged exoplanets or brown dwarfs. This Python package is publicly available in the `species` PyPI [1] and maintained on Github[2]. The software provides a coherent, easy-to-use framework to store, inspect, analyze, and plot observational data and models. It benefits from a wide variety of publicly available data such as atmospheric model spectra, photometric libraries, spectral libraries, evolutionary tracks, photometry of directly imaged companions, and filter transmission profiles.

Thanks to its online documentation, it is easy to install and use. The installation of this program requires an environment in which certain versions of some commonly used libraries are pre-installed on the system. But it also runs with the help of independent libraries such as `petitRADTRANS`[3] (pRT). pRT is a Python package for calculating the transmission and emission spectra of exoplanets, assuming clear or cloudy atmospheres. In addition, it also uses the `pymultinest`[4], this is a Bayesian inference tool which calculates the evidence and explores the parameter space which may contain multiple posterior modes and pronounced (curving) degeneracies in moderately high dimensions.

After the complete installation of `species`, we proceed to run the code. Initially, we create a `database` where we are going to include the models (described above) with the task `add-model` and the spectra with which we are going to compare (J2228+4310 and LP261-75B) with the task `add-object`, where we include the parallax of the object, the path of the file and the resolution of the spectrum. It is very important that we are going to work all in physical units of flux [W m^{-2} μm^{-1}] and wavelengths of [μm].

We define a parameter space with the variation in the parameters that we can change in each model. The most important parameters are the effective temperature $T_{\rm eff}$ and the surface gravity $\log(g)$. We proceed to apply the `multinest` and `mcmc` methods to find the best fitting parameters. Finally, when the fit converges, the residuals from the comparison between the model and the observational data can be obtained, in terms of the likelihood function $\mathcal{L}$, which

[1] `species` repository: https://species.readthedocs.io/en/latest/index.html
[2] Github: https://github.com/tomasstolker/species
[3] `pRT` repository: https://petitradtrans.readthedocs.io/en/latest/
[4] `pymultinest` repository: https://github.com/JohannesBuchner/PyMultiNest

is the mathematical relationship between the model D_j,m, the observational data D_j, and the uncertainties s_j associated with the data for all j measured data points. It is common practice to assume a Gaussian likelihood function Kitzmann et al. (2020):

$$\ln \mathcal{L} = -\frac{1}{2} \sum_{j=1}^{J} \frac{(D_j - D_{j,\ \mathrm{m}})^2}{s_j^2} - \frac{1}{2} \ln \left(2\pi s_j^2\right) .$$

As a reply, the method provides us with a confidence plot (see in Figure 3.1, top panel), that plots the exploration of parameters that were done in the process and with this the values of the parameters that best fit. It also gives us a plot and the datafile of the comparison of the model and the observational data (see in Figure 3.1, down panel). In addition, it is important to note, as shown in Figure 3.1 that the errors given by the program are very small, because they are statistical and systematic and refer to model fits the observational data and not to physical errors. Therefore, we do not include the errors in our results.

3.4 Discussion

In this section, we will discuss the behavior of the different models used to compare to observational data. We discuss the importance of taking into account some characteristics and parameters, like cloudless and cloudy models, and the main differences between T-type and L-type dwarfs modeling, among other important aspects.

3.4.1 L-dwarfs

In this Section, we aim at reproducing the spectrum of LP261-75b (L6). LP261-75B is characterized by a SED spectral energy distribution similar to that typical of a field L6 brown dwarf. As seen in Figure 3.2, it has prominent FeH features in the H-band, an important slope, and changes in the CH_4- and H_2O-bands. It has significant KI and Na alkali lines in its near-infrared spectrum, mainly in the J-band (Liu et al., 2016). The age calculations for LP261-75B, where for the entire LP261-75AB system we have values between 100-200 Myr using evolutionary models (Burrows et al., 2001), and for the single object, LP261-75B an age of $\sim$ 100 Myr, obtained with the measurement of strong Hα emission, suggesting that relatively young age (Reid, Walkowicz, 2006).

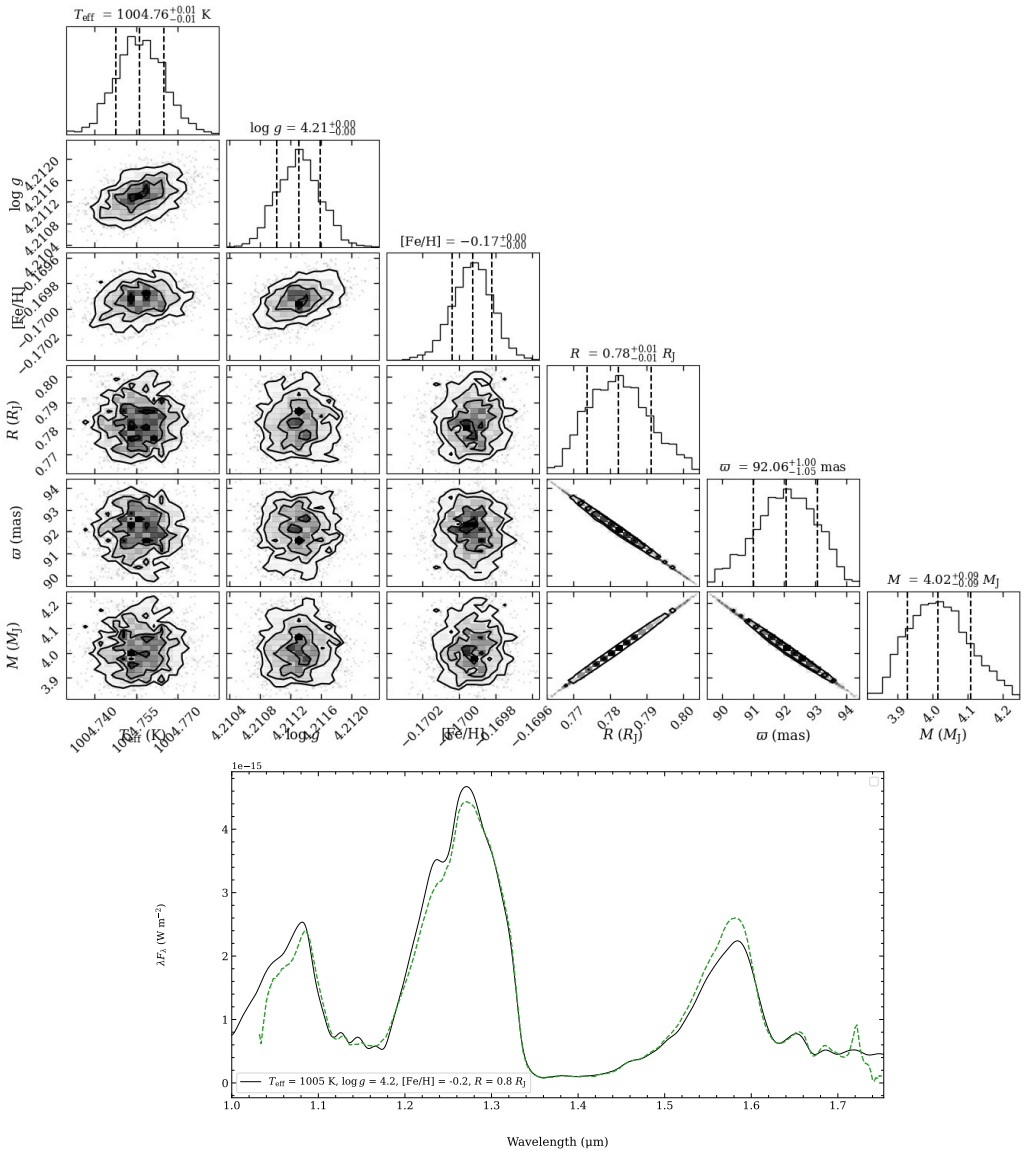

Figure 3.1: Example of reply `species`. Upper: Parameter space that varies to find parameter estimation for the model that best fits the observational data. Bottom: Best fit in comparison with the observation data.

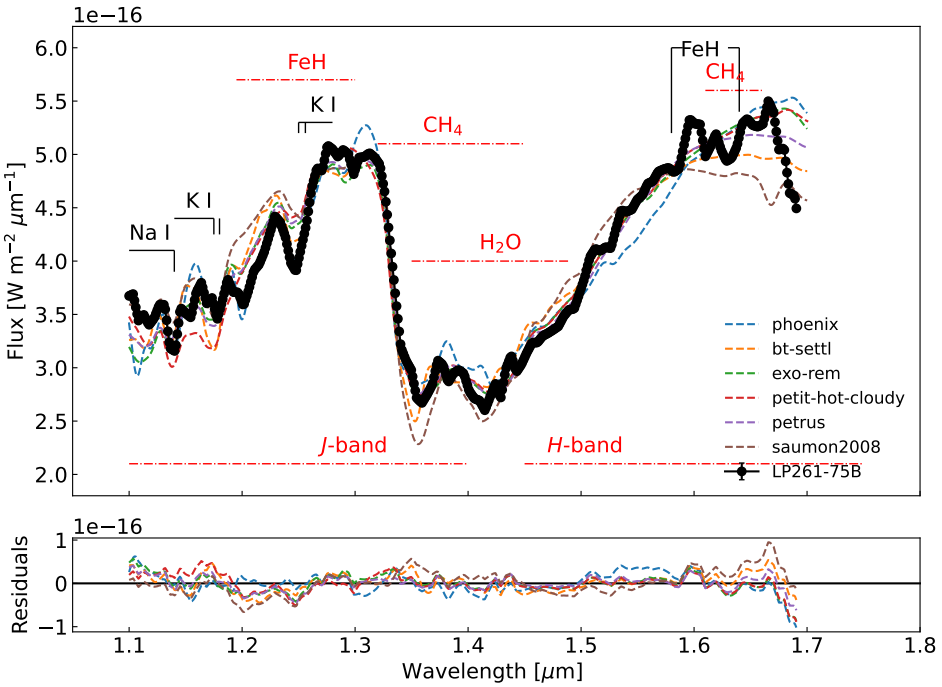

Figure 3.2: Best fits of L-dwarf models generated by `species` in comparison with the observation data of LP261-75B. Bands and lines taken from Cushing et al. (2005).

To model the spectrum of an L dwarf, we must consider many more parameters than for T dwarfs, for example, in this case, we will consider the sedimentation parameter (to take into account clouds) f_{sed}, but in addition we will consider values of carbon-oxygen C/O ratio important for the climate at different heights of the photosphere of these objects (Molaverdikhani et al., 2019).

We modeled the spectrum of LP261-75B by applying 17 different models using `species`. Most of these include clouds, but also others without clouds to evaluate their importance. Most also with variations in metallicity and C/O ratio. Two of them even included an adiabatic index parameter, described in the subsection 3.2.4. From this list of models, we are left with the 6 best-fit models, presented in Figure 3.2. In this case, to select the best fitting model, not only take into account the values of $\mathcal{L}$, because these values are very close to each other. And we notice in Figure 3.2, that there is no single spectrum that fits the whole spectrum completely, but if we separate them into bands, we can obtain better individual fits. Therefore, we are then left with the fits of **drift-phoenix**, as the best fit of the first part of the J-band, including the Fe band, **exo-rem** as a better fit of the center bands that include the CH_4,

and the H_2O, and **petitcode-hot-cloudy** as the best fit for the H-band.

The drift-phoenix model has a more complete list of opacities, which might explain why it provides the best fit between $1.1 - 1.3$ μm, including the FeH, and therefore since you have many lines in that sector that affect the spectrum, since we see that this FeH molecule is the most affected and has the most deviating fits in the other models. On the other hand, for the other sector of the CH_4, and the H_2O and H-band, probably it is most important the presence of clouds and the value of C/O relation that we take into account in the exo-rem and the petit-hot-cloudy models, giving us a dull H_2O band and the characteristic colors of an L-dwarf (Chabrier, Baraffe, 2000). By taking into account this condensation parameter f_{sed} we note its importance in the settings.

With these three models, find the physical parameters that are recorded in Table 3.1 below. These physical parameters of LP261-75B are consistent with values reported previously for this object. Reid, Walkowicz (2006) found an effective temperature of $T_{\rm eff} = 1500 \pm 150$ K, using the scale spectral type/temperature derived of Golimowski et al. (2004). Also Reid, Walkowicz (2006) found a mass of $M = 0.022 M_{\odot}$ using evaluative trajectories, similar to the Pleiades, consistent too with the mass found by Burrows et al. (2001) of $M = 15 - 30 M_J$.

Models	$T_{\rm eff}$ [K]	log(g) [dex]	radii $[R_J]$	mass $[M_J]$	[Fe/H]	f_{sed}	[C/O]
drift-phoenix	1527	3.12	1.02	20.55	-0.6		
exo-rem	1400	4.4	1.06	21.19	0.38	3.5	0.57
petitcode-hot-cloudy	1430	4.20	1.0	16.30	0.3	4.5	0.56

Table 3.1: Parameters calculated with the three best fits of the modeled spectra to the observational data of LP261-75B.

When comparing models with cloudy and non-cloudy atmospheres, we also observed a dismutation behavior in the physical parameters of effective temperature and gravity, but in this case, the best fits were observed in the models with cloudy atmospheres, evidencing the preference for cloudy atmospheres. For cloudless atmospheres, the temperature values were close to $T_{\rm eff} \sim 2000$ K, which is well above the expected values. Also, the radius value was almost half the expected one, for objects of this type (L6).

On the other hand, for this L-type object, we also observed the same behavior of mass values far from the physical sense in some models such as AMES or Saumon2008 for both clear and cloudy models. So we did not take them into account in the analysis.

3.4.2 T-dwarfs

A T-type brown dwarf is characterized by having a spectrum with narrow J- and H-bands and with higher flux in these bands than in any other band of the near-infrared spectrum, due to strong absorption by H_2O and CH_4, as seen, for example, in Figure 3.1. Furthermore, in Figure 3.3 we observed relevant chemical features such as strong absorption bands of H_2O and CH_4 at 1.15, 1.4, 1.6, μm, along with the importance of NH_3 and neutral alkali, generating pressure-broadened wings (Burrows, Volobuyev, 2003), which are highly sensitive to photospheric gas conditions. In addition, a relatively blue SED is observed by analyzing the spectrum between 1.1 to 1.8 μm, due in part to collision-induced absorption of H_2 (Linsky 1969, Saumon et al. 1994, Borysow 2002).

In order to model these features described in broad strokes above, a significantly large list of opacities must be taken into account to reproduce these patterns and correct pressure-temperature profile distributions. However, although the study of molecular opacities and the study of cool astronomical objects improved significantly, some lists of molecular opacities are still incomplete. In addition, the implementation of condensation and sedimentation is another important scenario to explore.

We modeled the spectrum of the brown dwarf J2228-4310 by applying 14 different models using the code of `species`. Among these, we tried most models without clouds, some models with clouds, and some include the eddy diffusion factor. From this list, we only selected the best 6 models to compare with each other, as seen in Figure 3.3. We calculated the Likelihood $\mathcal{L}$ value for these 6 models, where the lowest value represents the model that best fits the observational data of J2228-4310, the best fit being **petitcode-cool-clear**. Fitting the SED of the object using the petitcool-clear atmospheric models, we found an effective temperature of $T_{\rm eff}$ = 1000 K, and a surface gravity of log(g) = 4.9 dex, a metalicity [Fe/H] = 0.8, a radii of R = 0.8 R_J, and a mass of $M = 38.14 M_J$.

The physical parameters found for this brown dwarf are consistent with reported previously values, Buenzli et al. (2012) found an effective temperature of $T_{\rm eff}$ = 900 K, and surface gravity of log(g) = 5 dex, f_{sed} = 5 and found other solution changing the sedimentation parameter of f_{sed} = 3, the effective temperature of $T_{\rm eff}$ = 900 K, and surface gravity of log(g) = 4.5 dex, fitting the SED of the object using the Morley atmospheric models. Yang et al. (2016) also found an effective temperature of $T_{\rm eff}$ = 950 K, surface gravity of log(g) = 4.5 dex, sedimentation parameter of f_{sed} = 5, and a mass of $M = 41.9 M_J$.

For the study of T dwarfs, one of the biggest challenges has been to really identify the importance of taking into account the condensates in this type of

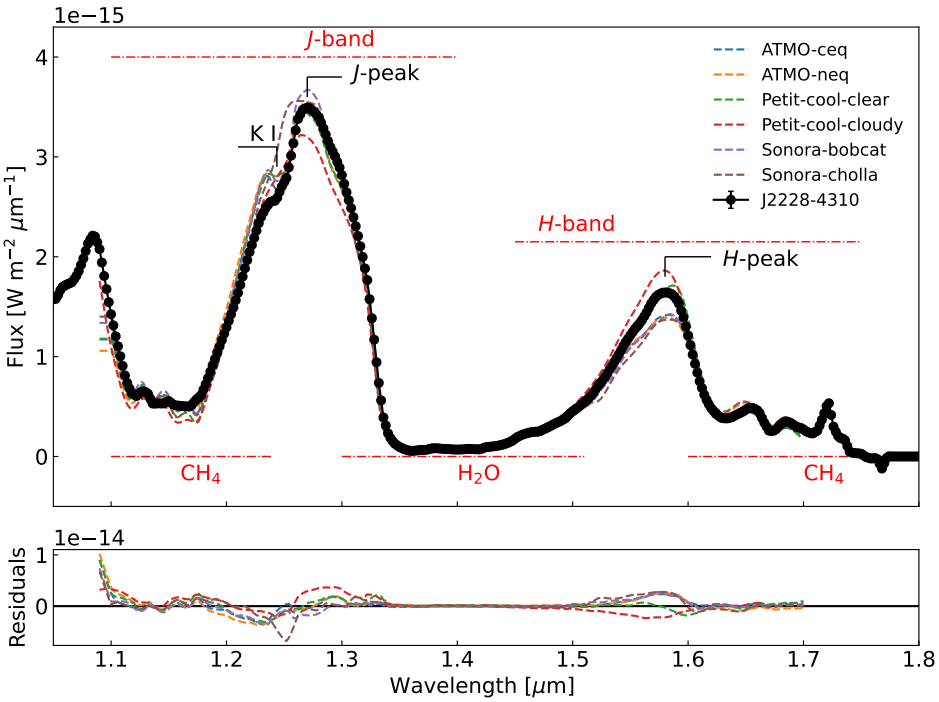

Figure 3.3: Best fits of T-dwarf models generated by `species` in comparison with the observation data of J2228-4310. Bands and lines taken from Cushing et al. (2005).

dwarf. So it is very relevant to know how clouds affect this type of object, and how these effects could be modeled. Previous studies like Burgasser et al. 2010b, or Buenzli et al. 2012, show how clouds are an important source of opacity in the spectra of T dwarfs, especially young and cold ones. However other studies such as Lueber et al. (2022) suggest that there are no appreciable differences between cloud and cloudless models for this type of brown dwarf.

We will initially focus our analysis on the implications of whether or not to consider clouds as a source of relevant opacity in T-type dwarfs and review the implications of both considerations. Within the model grids that we were using in `species` that contained clouds for effective temperatures as low as the T-type brown dwarfs of T_{eff} ~[600, 1500] K, we had only petitcode-cool (cloudy or clear) model. By comparing the cloudy and clear models, shown in Figure 3.4, we can observe how the model with clouds, increases the flow in the *H*-band and decreases in the *J*-band, generating a much smaller difference between the two bands. This generates a less accurate fit to the observed spectrum. Which is consistent with previous studies Burgasser et al. (2010b).

On the other hand, the cloud-free modeled spectrum fits the observational

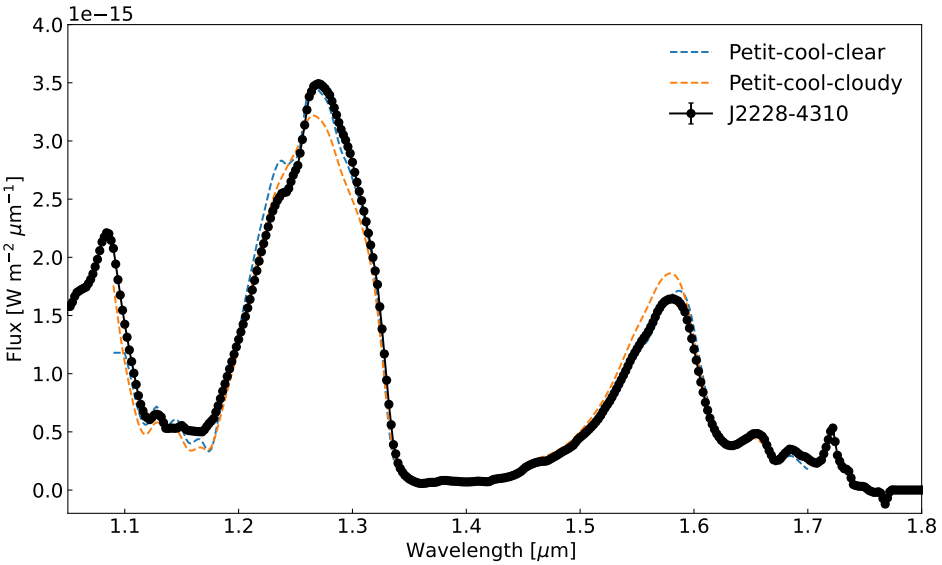

Figure 3.4: Cloudy and cloud-less models comparison

spectrum better, except for the K I neutral line near the peak of the J-band which shows a deviation. However, this particular line does not fit any of the applied models, as observed in Figure 3.3, thus we consider that this may be due to a reduced list of K opacities.

Another important aspect that we can observe is the quantitative differences in the physical parameters when clouds are taken into account. For this case, using petitcode-cool-cloudy we find lower values of effective temperature and surface gravity, as is also evident in other studies such as Burgasser et al. (2010b) studying the T-dwarf ROSS 458C (T8). In our case with J2228-4310, we found an effective temperature of $T_{\rm eff}$ = 850 K, and surface gravity of log(g) = 4.69 dex. There are no variations in mass, but there are variations in the radius R = 1.38 R_J, and the metallicity of [Fe/H] = 0.0, using a sedimentation index of f_{sed} = 0.67. Similar results with decreasing parameters for models with clouds occur for the same object J2228-4310 in Buenzli et al. (2012). We compare the differences of both cases (clear and cloudy) in Table 3.2.

Models	$T_{\rm eff}$ [K]	log(g) [dex]	radii [R_J]	mass [M_J]	[Fe/H]	f_{sed}
petitcode-cool-clear	1000	4.9	0.8	38.14	0.8	
petitcode-cool-cloudy	850	4.69	1.38	38.14	0.0	0.67

Table 3.2: Parameters calculated with the clear and cloudy best fits of the modeled spectra to the observational data of J2228-4310.

On the other hand, something that we found very curious in applying so many models, is that for most of the parameters, we obtained similar values. However, we obtained unphysical mass values, in the order of 1-4 M_J for the Sonora models. A strange behavior besides obtaining these low mass values is that the models still had a close fit to the observational data, as shown in Figure 3.3. This raises doubts about the reliability of the physics and chemistry of this type of model.

Finally, another interesting aspect of the model comparisons for T dwarfs, in the case of the ATMO models, we observed that the non-chemical equilibrium models (NEQ-strong and NEQ-weak) work much better than the chemical equilibrium models (CEQ) because obtaining a small likelihood value. The ATMO-CEQ tends to overestimate the temperature parameters and also gives values for the physically meaningless masses of around $4M_J$, while the ATMO-NEQ models fit the observational spectra better and have more rational stellar parameters.

3.4.3 Comparison between L- and T-dwarfs

We have previously discussed the principles and characteristics of the spectra of T- and L-type dwarfs, taking as representatives of both types, J2228-4310 (T6) and LP261-75B (L6).

From the cloud scenario, we observe that clouds are much more relevant for L-type dwarfs since they allow us to better model the quenched water band that these objects present and that models without clouds do not approach the observed spectrum and also give us physical values that do not agree with the spectral type. For the case of the T-type, both the models with clouds and without clouds fit the entire spectrum except for the flux ratio between the $J-$ and H-band peaks (Figure 3.4).

On the other hand, we also observed a relationship of the radius with respect to the effective temperature, as reported in previous studies such as Lueber et al. (2022). Where the retrieved radius generally decreases with effective temperature. However, in that study, we also found that some values inferred for some T dwarfs are implausibly low and may indicate missing physics or chemistry in the models ($\sim 0.5R_J$). This seemed consistent with an evolutionary cooling sequence. For our case, we obtain radius values of $R \sim 0.6R_J$, which seems consistent with these results.

In addition, the radii have a relation with the age of brown dwarfs, because the objects are cooling with time and therefore their size is decreasing. In addition, the major part of the observations have T-dwarfs older, in comparison with the L-dwarfs, which normally are younger. In this specific case, LP261-

75B is younger and its radius is bigger.

Finally, we conclude that modeling L-type dwarfs is more complex than modeling T-dwarfs, due to the importance of the condensates in their atmosphere. Equilibrium models fit L-type dwarfs better, while for T-type dwarfs, better fits were found for non-equilibrium models. Since in the much cooler stages of T-dwarfs the high-temperature condensates have settled out of their photospheres. However, since this process is gradual, all intermediate classes of brown dwarfs can be understood partly in terms of partial dust settling, which is the case for an L6 like LP261-75B (Allard et al., 2003b).

Chapter 4

Summary

The spectral indices generated during this thesis are a useful method for the course of the study of the variability of brown dwarfs and exoplanets. The study of atmospheric variability is one of the major ways to answer questions about the behavior inside the atmospheres of sub-stellar objects and exoplanets.

Before the existence of the spectral indices to pre-select the most likely L and T variable brown dwarfs, there was no informed method to find them. Thus, long hours of telescope time per object had to be blindly spent to possibly find a few that did show significant variability. Thus, the method presented here will likely save lots of valuable telescope time.

Our spectral indices technique turns out to be an observational and systematic method that studies the variabilities in different layers of the atmosphere, through the variations of different regions of the spectrum that are key to detailed analysis during photo-spectroscopy surveys and to understand the physics of inner the atmospheres. In the case of T dwarfs, the differences between the *J*- and *H*-band peaks study the deepest part of the photosphere, where the greatest variability is found. In the case of L dwarfs, we see that there is greater variability in other areas that are directly related to some molecules such as CH_4 and H_2O. These zones are more extended along the whole pressure column of the atmosphere.

We reported a variability fraction of 51^{+4}_{-38}% for mid-L dwarfs, and 38^{+4}_{-30}% for mid- and late-T dwarf sample assuming that the variable candidates selected are indeed variable. The variability fraction reported agrees with the variability fraction provided by Radigan (2014), Buenzli et al. (2014), and Metchev et al. (2015) for the same ranges of spectral types.

Using the index method we have a recovery rate of variable of ∼92% for mid-L dwarfs and 67% for mid- and late-T dwarfs. We are able to recover a false negative rate of ∼8% for mid-L dwarfs and 12.5% for mid- and late-T

dwarfs.

We compare our results of the spectral index method with respect to the results of the literature on variability studies of some objects, we observe consistency in our results and provide lists of new candidate variables to be studied observationally in the future. Exactly 8 new T-type candidates and 31 new L-type candidates.

Although our methods were created directly to study brown dwarfs, we currently know of cool directly-imaged exoplanets that share temperature and color characteristics with brown dwarfs. Thus, part of our future work is to apply our spectral index method to emission spectra of cool exoplanets, taking advantage of new technologies in observational astronomy such as the instruments aboard the *James Webb Space Telescope*.

The comparative study of spectral models and observational data helps us to conclude the importance of incorporating clouds in brown dwarf atmospheric modeling, with a greater impact on L-type dwarfs than T-dwarfs. It also shows that there is still a lot of work to be done in the modeling of these objects, especially on L-type objects, where it is necessary to extend the opacity lists for better fits in regions mainly where the FeH bands are found. In addition, for this spectral type (L), having more parameters to adjust complicates the calculations and increases the computation time.

Our results of determining physical parameters of brown dwarfs from the SED fit give us results consistent with the literature for both the J2228-4310 (T6) dwarf where we find an effective temperature of $T_{\rm eff} = 1000$ K, a surface gravity of log(g) = 4.9 dex, a metallicity [Fe/H] = 0.8, a radius of R = 0.8 R_J, and a mass of $M = 38.14 M_J$ with the petitcode-cool-clear model. And for LP261-75B (L6) we find an effective temperature of $T_{\rm eff} = 1430$ K, a surface gravity of log(g) = 4.20 dex, a metallicity [Fe/H] = 0.3, a sedimentation rate of $f_{sed} = 4.5$, a carbon-to-oxygen ratio of [C/O] = 0.56, a radius of R = 1.0 R_J, and a mass of $M = 16.30 M_J$ with the petitcode-hot-cloudy model.

Important points to take into account in future work on the use of models to generate synthetic spectra are the determination of masses by other methods to further narrow down this parameter and analyze whether better results are obtained. On the other hand, to reproduce the spectra of L-type brown dwarfs, it is necessary to try to narrow down most of the parameters, since having more variable parameters, they are more difficult to model, and also take into account the importance of the C/O parameter in these spectra of L-type dwarfs, in order to have better fits.

Appendix A

Samples to validate the variability method

A.1 L-dwarfs sample

Sample L dwarfs with spectral type between L4-L8 are available at the SpeX Spectral Library. Variability references: (1) Clarke et al. (2008), (2) Radigan et al. (2014), (3) Vos et al. (2020), (4) Metchev et al. (2015), (5) Buenzli et al. (2014), (6) Dupuy, Liu (2012), (7) Koen et al. (2004), (8) Vos et al. (2018)

Name	SpeX NIR SpT	Our variable candidate	N° regions	Variability literature	Reference variability studies
L 362-29 B	L5.5	Yes	15/15		
2MASS J00282091+2249050	L7	No	05/15		
2MASSW J0030300-145033	L7	No	05/15	Non-variable	(1), (2)
2MASS J00325937+1410371	L8	No	05/15		
LSPM J0036+1821	L4	Yes	09/15	Variable	(3)
2MASSI J0103320+193536	L6	No	04/15	Variable	(4), (3)
2MASSI J0131183+380155	L4	Yes	09/15		
2MASS J01443536-0716142	L5.5	Yes	10/15		
2MASS J01550354+0950003	L5	Yes	09/15		
DENIS J020529.0-115925	L7	Yes	11/15		
2MASSW J0208236+273740	L5	Yes	15/15		
2MASS J02425693+2123204	L4	No	06/15		
2MASS J02572581-3105523	L8	Yes	09/15		
2MASSI J0318540-342129	L7	No	08/15		
2MASS J04390101-2353083	L6	Yes	09/15		
2MASS J04474307-1936045	L5	Yes	09/15		
2MASS J06244595-4521548	L5	Yes	11/15	Variable	(5), (3)
2MASS J06523073+4710348	L4.5	No	04/15		
2MASS J06540564+6528051	L6	Yes	10/15		
2MASS J07171626+5705430	L6.5	Yes	10/15		
2MASSW J0801405+462850	L6.5	Yes	10/15	Non-Variable	(5)
2MASS J08053189+4812330	L4+T5	Yes	09/15	Binary, Variable	(6)
2MASSW J0820299+450031	L5	No	04/15	Non-variable	(4), (3)
2MASSI J0825196+211552	L6	Yes	09/15	Variable	(5), (4)
2MASS J08350622+1953050	L4.5	Yes	11/15		

Name	SpeX NIR SpT	Our variable candidate	N° regions	Variability literature	Reference variability studies
2MASS J08354256-0819237	L5	Yes	10/15		
2MASS J08511627+1817302	L5.5	No	07/15		
2MASS J08575849+5708514	L8	No	02/15		
2MASS J09054654+5623117	L5	No	08/15		
2MASS J09083803+5032088	L7	Yes	09/15	Non-Variable	(5)
2MASS J09153413+0422045	L7	Yes	12/15		
2MASSW J0929336+342952	L7.5	No	04/15		
2MASS J10071185+1930563	L8	No	05/15		
2MASS J10101480-0406499	L6	Yes	09/15	Variable	(3)
2MASS J11040127+1959217	L4	Yes	09/15		
2MASSI J1043075+222523	L8	No	02/15		
2MASS J10433508+1213149	L7	Yes	14/15	Variable	(3)
2MASS J10440942+0429376	L7	No	06/15		
HD 97334B	L4.5	No	06/15		
2MASS J11211858+4332464	L7.5	Yes	14/15		
DENIS J112639.9-500355	L4.5	Yes	09/15	Variable	(2), (4), (3)
2MASS J11555389+0559577	L7	No	06/15	Non-variable	(7)
2MASS J12195156+3128497	L8	No	06/15	Non-variable	(5), (3)
SIPS J1228-1547	L5.5	Yes	12/15		
2MASSW J1239272+551537	L5	No	05/15		
2MASS J13262981-0038314	L5.5	No	01/15		
2MASS J14002320+4338222	L7	Yes	15/15		
ULAS2MASS J1407+1241	L5	Yes	15/15		
2MASS J14222720+2215575	L6.5	Yes	09/15		
2MASS J14283132+5923354	L4	Yes	10/15		

Name	SpeX NIR SpT	Our variable candidate	N° regions	Variability literature	Reference variability studies
2MASSW J1507476-162738	L5.5	Yes	10/15	Variable	(4), (3)
2MASSW J1515008+484742	L6.5	No	04/15	Non-variable	(5)
2MASS J15150607+4436483	L7.5	No	07/15		
2MASS J15200224-4422419B	L4.5	Yes	12/15		
Gl 584c	L8	No	01/15		
2MASSI J1526140+204341	L7	Yes	10/15		
2MASS J16303054+4344032	L7.5	No	02/15		
2MASS J16335933-0640552	L6	No	07/15		
2MASS J17054834-0516462	L4	Yes	10/15		
2MASSI J1711457+223204	L6.5	No	08/15		
2MASS J17461199+5034036	L5	Yes	11/15		
2MASS J17502484-0016151	L5.5	Yes	10/15	Variable	(2), (5), (3)
2MASS J19285196-4356256	L5	Yes	11/15	Variable	(4), (3)
2MASS J18212815+1414010	L5	Yes	11/15	Variable	(4)
2MASSI J2002507-052152	L6	No	07/15		
2MASSW J2101154+175658	L7.5	No	02/15		
2MASS J21321145+1341584	L6	Yes	09/15		
2MASSW J2148162+400359	L6	No	03/15	Non-variable	(4), (3)
2MASSI J2158045-155009	L4	Yes	09/15		
2MASS J22120703+3430351	L5	No	04/15		
2MASSW J2224438-015852	L4.5	No	06/15	Non-variable	(4), (3)
2MASS J22443167+2043433	L6.5	No	06/15	Non-variable	(7), (3)
2MASS J22521073-1730134	L7.5	No	07/15		
2MASSI J2325453+425148	L8	No	05/15		

Table A.1: 75 SpeX/IRTF brown dwarfs to validate method of L-dwarfs.

A.2 T-dwarfs sample

T dwarfs with spectral type between T5.5-7.5 are available at the SpeX Spectral Library. Variability references: (1) Koen et al. (2004), (2) Buenzli et al. (2014), (3) Radigan et al. (2014), (4) Allers et al. (2020), (5) Dupuy, Liu (2012), (6) Metchev et al. (2015), (7) Clarke et al. (2008), (8) Vos et al. (2018), (9) Buenzli et al. (2012)

Name	SpeX NIR SpT	Our variable candidate	N° regions	Variability literature	Reference variability studies
2MASSI J0243137–245329	T6.0	No	04/12	Non-variable	(1)(2)(3)
2MASSI J0727182+171001	T7.0	Yes	11/12		
2MASSI J0937347+293142	T6.0	No	05/12		
2MASSI J1047538+212423	T6.5	No	10/12	Variable	(4)
2MASSI J1217110–031113	T7.5	Yes	11/12		
2MASSI J1534498–295227	T5.5	No	03/12		
2MASSI J1553022+153236	T7.0	Yes	11/12	Binary	(5)
2MASSI J2356547–155310	T5.5	No	03/12		
2MASS J003451+052305	T6.5	Yes	11/12		
2MASS J051609–044549	T5.5	No	04/12	Non-variable	(6)
2MASS J111451–261823	T7.5	No	10/12		
2MASS J122554–273946	T6.0	No	08/12		
2MASS J123147+084733	T5.5	No	04/12		
2MASS J123739+652614	T6.5	No	08/12		
2MASS J154627–332511	T5.5	No	03/12	Non-variable	(3)(7)
2MASS J161504+134007	T6.0	Yes	12/12		
2MASS J182835–484904	T5.5	No	06/12	Non-variable	(3)(7)
Gliese 570D	T7.5	Yes	11/12		
HD 3651B	T7.5	No	10/12		
SDSS J175805+463311	T6.5	Yes	11/12		
SDSSp J111010+011613	T5.5	No	07/12	Non-variable	(8)
SDSSp J134646–003150	T6.5	Yes	11/12		
SDSSp J162414+002915	T6		No	05/12	Non-variable (1)(3)
2MASS J005019–332240	T7.0	Yes	11/12	Variable	(3) (6)
ULAS J141623+134836 B	T7.5	No	10/12	Non-variable	(6)
2MASS J222828–431026	T6.5	Yes	12/12	Variable	(6)(9)

Table A.2: 26 SpeX/IRTF brown dwarfs to validate method of T-dwarfs.

Appendix B

Previously Known Variables and Non-variables

B.1 L-dwarfs

B.1.1 Known variable L-dwarfs

The following objects were selected as variable candidates by our indices.

LSPM J0036+1821

J0036+1821 is an L3.5 dwarf (Reid et al., 2000). It is located at a distance of 8.7356 ± 0.0105 pc (Gaia Collaboration, 2020). Gagné et al. (2015) found an effective temperature of T_{eff} = 1900 K, and a surface gravity of, log(g) = 5.0 dex, by fitting the Spectral Energy Distribution (SED) of the object using the BT-Settl atmospheric models.

Metchev et al. (2015) used J0036+1821 as a control object for recognizing potential activity-induced photometric effects. They found a variability amplitude in the [3.6] Spitzer channel of $0.47 \pm 0.05\%$, and a variability amplitude of $0.19 \pm 0.05\%$ in the [4.5] Spitzer channel. They measured a period 2.7 ± 0.3 hr. Metchev et al. (2015) did not include as a variable in their final sample since its variability might be associated with magnetic activity. Croll et al. (2016) measured a variability amplitude of $A_J = 1.22 \pm 0.04$ %. Osorio et al. (2005) measured a variability in I-band of 0.25%. J0036+1821 was found in 9 out of 15 areas in our index–index plots, indicating that it is a variable candidate.

2MASS J04390101-2353083

J0439-2553 is an L4.5 dwarf (Schneider et al., 2014). It is located at a distance of 12.387 ± 0.0550 pc (Gaia Collaboration, 2020). Gagné et al. (2015) found an effective temperature of T_{eff} = 1600 K, and a surface gravity of, log(g)

= 5.0 dex, by fitting the SED of the object using the BT-Settl atmospheric models.

Wilson et al. (2014) found a variability amplitude for J0439-2553 of 2.6 ± 0.5% and Radigan (2014) found <1.2 % using the same SofI instrument. J0439-2553 was found in the variable areas in 9 out of 15 of our index–index plots, indicating is a variable candidate.

2MASS J06244595-4521548

J0624-4521 is an L6.5 dwarf (Schneider et al., 2014). It is located at a distance of 12.1914 ± 0.0532 pc (Gaia Collaboration, 2020). Gagné et al. (2015) found an effective temperature of T_{eff} = 1500 K, and a surface gravity of, log(g) = 5.0 dex, by fitting the SED of the object using the BT-Settl atmospheric models.

Buenzli et al. (2014) measured a variability of at least 1% and a period of more than 3hr with a sinusoidal light curve. J0624-4521 was found in the variable areas in 11 out of 15 of our index–index plots, indicating that it is a variable candidate.

2MASS J08053189+4812330

J0805+4812 was a candidate to be an unresolved binary (Burgasser, 2007), and it was confirmed as such by Dupuy, Liu (2012) showing large perturbations due to orbital motion with spectral types L4 (primary) + T5 (secondary). J0805+4812 shows variability in their light curve (Dupuy, Liu, 2012). They associated the measurement of variability to the binary system and not necessarily internal processes of the atmospheres such as clouds

J0805+4812 was found in the variable areas in 9 out of 15 of our index–index plots, indicating that it is a variable candidate.

2MASSI J0825196+211552

J0825+2115 is an L7.5 dwarf (Kirkpatrick et al., 2000). (Gagné et al., 2015) found an effective temperature of T_{eff} = 1500 K, and a surface gravity of, log(g) = 5.0 dex, by fitting the SED of the object using the BT-Settl atmospheric models.

Buenzli et al. (2014) measured significant variability in the J- and H-band ($A_{J,H} > 1$). Metchev et al. (2015) found a variability amplitude of $A_{[3.6]} = 0.81 \pm 0.08\%$, $A_{[4.5]}1.4 \pm 0.3$ %, with a period of 7.6 hr. J0825+2115 was found in 9 out of 15 variable areas of our index–index plots, indicating that it is a variable candidate.

2MASS J08350622+1953050

J0835+1953 is a L5 dwarf (Schneider et al., 2014). It is located at a distance of 26.1 ± 5.1 pc (Schmidt et al., 2010). Gagné et al. (2015) found an effective temperature of T_{eff} = 1600 K, and a surface gravity of, log(g) = 5.0 dex, by fitting the SED of the object using the BT-Settl atmospheric models.

Radigan (2014) measured a peak-to-peak variability of $1.3 \pm 0.2\%$ using the SofI instrument, installed on the New Technology Telescope (NTT) in J-band. J0835+1953 was found in the variable areas in 11 out of 15 of our index–index plots, indicating that it is a variable candidate.

2MASS J10433508+1213149

J1043+1213 is an L7 dwarf (Burgasser et al., 2010a). It is located at a distance of 18.2 ± 3.8 pc (Schmidt et al., 2010). Gagné et al. (2015) found an effective temperature of T_{eff} = 1500 K, and a surface gravity of, log(g) = 5.5 dex, by fitting the SED of the object using the BT-Settl atmospheric models. Metchev et al. (2015) measured a variability amplitude of $A_{[3.6]} = 1.54 \pm 0.15$ %, $A_{[4.5]} = 1.2 \pm 0.2$ %, with a period 3.8 ± 0.2 hr, but irregular. J1043+1213 was found in the variable areas in 14 out of 15 of our index–index plots, indicating that it is a variable candidate.

DENIS J112639.9-500355

J1126-5003 is an L5.5 dwarf (Phan-Bao et al., 2008). It is located at a distance of 16.1726 ± 0.0654 pc (Gaia Collaboration, 2020).

Folkes et al. (2007) reported that J1126-5003 has unusually blue colors for its L4.5 optical or L6.5 NIR spectral type. Radigan et al. (2014) measured a peak-to-peak variability amplitude in the J-band of $1.2 \pm 0.1\%$. Metchev et al. (2015) measured a variability amplitude of $A_{[3.6]} = 0.21 \pm 0.04$ %, $A_{[4.5]} = 0.29 \pm 0.15$ %, and they calculated a period of 3.2 ± 0.3 hr with regular periodicity. J1126-5003 was found in the variable areas in 9 out of 15 of our index–index plots, indicating that it is a variable candidate.

2MASSW J1507476-162738

J1507-1627 is an L5 dwarf (Kirkpatrick et al., 2000). It is located at a distance of 7.4102 ± 0.0143 pc (Gaia Collaboration, 2020). Gagné et al. (2015) found an effective temperature of T_{eff} = 1900 K, and a surface gravity of log(g) = 5.0 dex, by fitting the SED of the object using the BT-Settl atmospheric models.

Metchev et al. (2015) measured a variability amplitude of $A_{[3.6]} = 0.53 \pm 0.11$ %, $A_{[4.5]} = 0.45 \pm 0.09$ %, with an irregular period of 2.5 ± 0.1 hr. Metchev et al. (2015) explains that J1507-1627 shows clear spot evolution, since one

oscillation appears around 7hr in one channel observing sequence, and continuously grows in amplitude until the end of the other channel sequence, 2.5 hr rotations later.

J1507-1627 was found in the variable areas in 10 out of 15 of our index–index plots, indicating that it is a variable candidate.

2MASS J17502484-0016151

J1750-0016 is an L5.5 dwarf (Burgasser et al., 2010a). It is located at a distance of 9.2097 ± 0.0168 pc (Gaia Collaboration, 2020). (Gagné et al., 2015) found an effective temperature of T_{eff} = 1800 K, and a surface gravity of log(g) = 4.5 dex, by fitting the SED of the object using the BT-Settl atmospheric models.

Buenzli et al. (2014) measured a significant variability in the J-band, and regions between 1.12 and 1.32 μm. However, the variation in the H-band is not statistically significant. And they obtained a period > 4hr for J-band with a sinusoidal light curve. J1750-0016 was found in the variable areas in 10 out of 15 of our index–index plots, indicating that it is a variable candidate.

2MASS J18212815+1414010

J1821+1414 is an L5 dwarf (Schneider et al., 2014). Gagné et al. (2015) found an effective temperature of T_{eff} = 1800 K, and a surface gravity of log(g) = 4.5 dex, by fitting the SED of the object using the BT-Settl atmospheric models. Looper et al. (2008) classified this object as L4.5 peculiarly red indicating moderately low gravity, including relative weakness in the alkaline and FeH strengths and sharpness of the H-band continuum. Gagné et al. (2014) concluded that despite its signatures of youth this object does not belong to any known young moving group.

Metchev et al. (2015) measured a variability amplitude of $A_{[3.6]} = 0.54 \pm 0.05$ %, $A_{[4.5]} = 0.71 \pm 0.14$ %, and an irregular period of 4.2 ± 0.1 hr. J1821+1414 was found in the variable areas in 11 out of 15 of our index–index plots, indicating that it is a variable candidate.

B.1.2 Known non-variables L-dwarfs

In this appendix, we list the objects that were selected by our indices as non-variable candidates.

2MASSW J0030300-145033

J0030-1450 is an L7 dwarf (Kirkpatrick et al., 2000). It is located at a distance of 26.7 ± 3.3 pc (Faherty et al., 2009). Gagné et al. (2015) found an effective

temperature of T_{eff} = 1500 K, and a surface gravity of log(g) = 5.0 dex, by fitting the SED of the object using the BT-Settl atmospheric models.

Enoch et al. (2003) detected periodic variability in K_s-band, with an amplitude of 0.19 mag and period of 1.5 hr. However Clarke et al. (2008) found no evidence of variability, with amplitude smaller than 40 mmag. Similarly, Radigan et al. (2014) observed a flat light curve for this target in the J-band throughout 3.2 hr. J0030-1450 was found in the variable areas in 5 out of 15 of our index–index plots, indicating that it is a non-variable candidate.

2MASSI J0103320+193536

J0103+1935 is an L6 (Kirkpatrick et al., 2000) dwarf. It is located at a distance of 23 ± 2 pc (Faherty et al., 2009). Gagné et al. (2015) found an effective temperature of T_{eff} = 1600 K, and a surface gravity of log(g) = 5.5 dex, by fitting the SED of the object using the BT-Settl atmospheric models.

Metchev et al. (2015) measured a small variability amplitude of $A_{[3.6]} < 0.40\%$ and $A_{[4.5]} < 0.48\%$. J0103+1935 was found in the variable areas in 3 out of 15 of our index–index plots, indicating that it is a non-variable candidate.

Even though J0103+1935 shows some variability, our index method is probably not sensitive to such small variability levels.

2MASSW J0801405+462850

J0801+4628 is an L6.5 dwarf (Kirkpatrick et al., 2000). It is located at a distance of 19.1 ± 3.7 pc (Schmidt et al., 2010). Gagné et al. (2015) found an effective temperature of T_{eff} = 1500 K, and a surface gravity of log(g) = 5.0 dex, by fitting the SED of the object using the BT-Settl atmospheric models.

Buenzli et al. (2014) did not find any significant variability. J0801+4628 was found in the variable areas in 8 out of 15 of our index–index plots, indicating that it is a non-variable candidate.

2MASSW J0820299+450031

J0820+4500 is an L5 dwarf (Kirkpatrick et al., 2000), located at a distance of 42.7 ± 8.4 pc. Metchev et al. (2015) measured a variability amplitude of $A_{[3.6]} < 0.40\%$, $A_{[4.5]} < 0.48\%$, but period could not be determined for this object. J0820+4500 was found in the variable areas in 4 out of 15 of our index–index plots, indicating that it is a non-variable candidate. Such a low percentage of variability might not be detectable with our method.

2MASS J09083803+5032088

J0908+5032 is an L8 dwarf (Schneider et al., 2014). It is located at a distance of 10.4244 ± 0.0596 pc. Gagné et al. (2015) found an effective temperature of $T_{eff} = 1600$ K, and a surface gravity of log(g) = 5.5 dex, by fitting the SED of the object using the BT-Settl atmospheric models.

Buenzli et al. (2014) did not measure any significant variability using HST/WFC3 time-resolved spectroscopy. J0908+5032 was found only in 8 out of 15 variable areas of our index–index plots, indicating that it is a non-variable candidate.

2MASS J10101480-0406499*

J1010-0406 is an field L6 dwarf (Cruz et al., 2003; Reid et al., 2008). It is located at a distance of 18 ± 2 pc. Gagné et al. (2015) found an effective temperature of $T_{eff} = 1600$ K, and a surface gravity of log(g) = 5.0 dex, by fitting the SED of the object using the BT-Settl atmospheric models.

Wilson et al. (2014) found a variability amplitude of $5.1 \pm 1\%$ in an observation window of only 3 hr, and no period was found. Radigan (2014) also found a large-amplitude variability for this object ($3.6 \pm 0.4\%$) using the SofI instrument. J1010-0406 was found in the variable areas in 6 out of 15 of our index–index plots, indicating that it is a non-variable candidate. This is the only object in our sample that is a false negative.

2MASS J11555389+0559577

J1155+0559 is an L7.5 dwarf (Knapp et al., 2004). It is located at a distance of 17.27 ± 3.04 pc (Faherty et al., 2012). This object is somewhat controversial and interesting with respect to its spectral type and variability, for which they have even cataloged it as L6-L8 peculiar (Gagné et al., 2015). Gizis et al. (2002) noted the presence of H-α, and therefore may have associated magnetic fields, which can generate variability. In addition, over a long observation period of approx. 75 hr in I-band, (Koen, 2003) observed associated variability, which they measured for a period of about 8 hr.

In addition, Koen et al. (2004) studied J1155+0559 in the K- and H-bands and shows variations with a periodicity of 46 min, which is quite far from the 8 hr mentioned in Koen (2003), however, this previous periodicity is not discarded since Koen et al. (2004) it was only studied for 3.4h. J1155+0559 was found in the variable areas in 6 out of 15 of our index–index plots, indicating that it is a non-variable candidate.

2MASS J12195156+3128497

J1219+3128 is an L8 dwarf (Schneider et al., 2014). It is located at a distance of 18.1 ± 3.7 pc (Schmidt et al., 2010). Tannock et al. (2021) found an effective temperature of T_{eff} = 1330 K, and a surface gravity of log(g) = 5.1 dex, by fitting the SED of the object using the BT-Settl and SM08 atmospheric models.

Buenzli et al. (2014) measured a minimum in the 1.12-1.2 μm wavelength range, with a small degree of variability, and they presented J1219+3128 as a curious case. Therefore, they classify it as tentative variability. J1219+3128 was found in the variable areas in 6 out of 15 of our index–index plots, indicating that it is a non-variable candidate.

2MASSW J1515008+484742

J1515+4847 is an L6.5 dwarf (Cruz et al., 2003). It is located at a distance of 9.8073 ± 0.0246 (Gaia Collaboration, 2020). Gagné et al. (2015) found an effective temperature of T_{eff} = 1600 K, and a surface gravity of log(g) = 5.0 dex, by fitting the SED of the object using the BT-Settl atmospheric models.

Buenzli et al. (2014) found no evidence of significant variability in any of the spectral regions for J1515+4847, showing less than 0.5-1% variability per hour, which is within the observational uncertainties. J1515+4847 was found in the variable areas in 4 out of 15 of our index–index plots, indicating that it is a non-variable candidate.

2MASSW J2148162+400359

J2148+4003 is an L7 dwarf (Schneider et al., 2014) at a distance of 8.0857 ± 0.0235 pc (Gaia Collaboration, 2020), and it is a very red brown dwarf (Looper et al., 2008). Metchev et al. (2015) measured low variability ($A_{[3.6]}$ = 1.33 ± 0.07%, $A_{[4.5]}$ = 1.03 ± 0.10%) in a long observation time (14h). They classify J2148+4003 as non-variable for the variability is low over a long period of time, so, it is related to uncertainties. J2148+4003 was found in the variable areas in 3 out of 15 of our index–index plots, indicating that it is a non-variable candidate.

2MASSW J2224438-015852

J2224-0158 is an L4.5 dwarf (Kirkpatrick et al., 2000). It is located at a distance of 11.6075 ± 0.0549 pc (Gaia Collaboration, 2020). Burningham et al. (2021) found an effective temperature of T_{eff} = 1912 K, and a surface gravity of log(g) = 5.47 dex, using atmospheric retrieval present in (Burningham et al., 2017), studying various approaches to cloud decks at different pressures.

Metchev et al. (2015) measured a small variability amplitude of $A_{[3.6]} < 0.10\%$, $A_{[4.5]} < 0.15\%$. Therefore, they classify this object as non-variable. (Gelino et al., 2002) did not measured any variability in the I-band for J2224-0158. In addition, Burningham et al. (2021) showed us that it has a covering of enstatite and quartz clouds, but that the body must have an unfavorable geometry to detect rotational modulation signals, or that the dark regions are arranged latitudinally in bands, and this may be why variability in near-infrared wavelengths is not observed. J2224-0158 was found in the variable areas in 6 out of 15 of our index–index plots, indicating that it is a non-variable candidate.

2MASS J22443167+2043433

J2244+2043 is an L6.7 (Faherty et al., 2016), young and low-gravity dwarf (Gizis et al., 2015). It is located at a distance of 19 ± 2 pc (Faherty et al., 2009).

Morales-Calderón et al. (2006) and Vos et al. (2018) found variability very close to the RMS amplitude, in the channel 4.5 μm in 5.7 hr of observation and no variability in the channel [3.6]. Both using Spitzer/IRAC. In addition, Vos et al. (2018) found no variability in J-band during 4h, using UKIRT/WFCAM but they predict with the periodogram a period of $P > 5.5$ h.

This suggests that the light curves of this object may have evolved in time or that they possess longitudinal bands with sinusoidal surface brightness modulations and an elliptical spot. When two bands have slightly different periods due to different velocities or directions, they interfere to produce rhythm patterns, according to Apai et al. (2017). However, the discussion continues, because in Metchev et al. (2015) found no significant variability ($A_{[3.6]} < 0.10, A_{[4.5]} < 0.15$). J2244+2043 was found in the variable areas in 6 out of 15 of our index–index plots, indicating that it is a non-variable candidate.

B.2 T-dwarfs

B.2.1 Known variables T-dwarfs

The following objects were selected by our indices as variable candidates.

2MASS J22282889–431026

2M2228 was classified as a T6.5 spectral type (Burgasser et al., 2003). Buenzli et al. (2012) measured a variability amplitude of 1.85±0.07 % in the J-band, and a 2.74±0.11% in the H-band using near-infrared HST/WFC3 spectra. The

J-, *H*-band and H_2O band at 1.4 μm light curves show phase shifts. Buenzli et al. (2012) found that the phase lag increases with decreasing pressure level, or higher altitude, probing the heterogeneity in the atmosphere of 2M2228 in both horizontal and vertical directions.

To test our spectral indices, we used a single-epoch SpeX/IRTF spectrum of 2M2228 from Burgasser et al. (2004). 2M2228 was found in the variable areas in 12 out of 12 our index-index plots, validating the effectiveness of our indices.

2MASS J00501994–3322402

J0050–3322 is classified as a T7.0 brown dwarf (Kirkpatrick et al., 2011). Using a forward modelling analysis, Zhang et al. (2021) measured an effective temperature of $T_{eff} = 947^{+23}_{-24} K$, surface gravity log g = $4.06^{+0.26}_{-0.26}$, and metallicity of, Z = $-0.11^{+0.15}_{-0.15}$. J0050-3322 was monitored by Metchev et al. (2015) with *Spitzer*, finding no significant variability in the [3.6] channel, and a variability amplitude of $1.07 \pm 0.11\%$ in the [4.5] channel. J0050–3322 has a regular light curve, with a period of $P = 1.55 \pm 0.02$ hr, being one of the fastest brown dwarf rotators. J0050–3322 was found in the variable areas in 11 out of 12 of our index-index plots.

B.2.2 Known non-variables T-dwarfs

The following objects were selected as non-variable candidates by our spectral indices.

2MASSI J1047538+212423

J1047+2124 is a T6.5 dwarf (Burgasser et al., 2000). Filippazzo et al. (2015) provided physical parameters for this object: $T_{eff} = 880 \pm 76$ K, $log(g) = 4.96 \pm 0.49$ dex, age around $0.5 - 10$ Gyr, M= 41.61 ± 26.03 M_{jup} and R = 4.96 ± 0.49 R_{jup}. Allers et al. (2020) used the Infrared Array Camera on the Spitzer Space Telescope used the Infrared Array Camera on the Spitzer Space Telescope, on its [4.5] channel, for two days, during 7 hr and 14 hr each. Allers et al. (2020) found sinusoidal variability of 0.5%, and adopt a period of 1.741 ± 0.007 hr.

In addition, Allers et al. (2020) measured the wind speed for this object, in radio observation taken with Karl G. Jansky Very Large Array (VLA), which generates an (unknown) atmospheric inhomogeneity that dominates the photometric variability, with a similar period, 1.758 ± 0.0012 hr. J1047+2124 was found in the variable areas in 10 out of 12 of our index-index plots, indicating that it is a non-variable candidate. Since J1047+2124 is a false negative, in

Section 5 of Oliveros-Gomez et al. (2022), we analyze in detail this particular object.

ULAS J141623.94+134836.3 B

J1416+1348 is a resolved L+T subdwarf system, separated by 9" (Burgasser et al., 2010a). The primary dwarf is ULAS J141623.94+134836.3 (J1416+1348A) with a L7 spectral type. On the other hand, the secondary object J1416+1348B, is a T7.5 dwarf. Burgasser et al. (2000) noted the unusually blue $H-W2$ and $W1-W2$ colors of this object and connected these properties to its metal-poor atmosphere. The very blue $Y-K$ color of this companion suggests high gravity and low metallicity, with $logg = 5.21^{+0.26}_{-0.25}$ dex and metallicity $Z = -0.39^{+0.14}_{-0.11}$. Zhang et al. (2021) derived an effective temperature of $T_{eff} = 695 \pm 33$ K.

Variability studies have been performed on both objects. J1416+1348B was initially studied in Khandrika et al. (2013) and marginal evidence of J-band variability was found using the Gemini infrared camera on the 3 m Shane telescope at Lick Observatory. Radigan et al. (2014) and Metchev et al. (2015) found no significant variability. Metchev et al. (2015) provided an upper levels of variability of A[3.6] <0.91 % and A[4.5] <0.59 %. J1416+1348B was found in the variable areas in 10 out of 12 our index-index plots, indicating that it is a non-variable candidate.

2MASS J05160945–0445499

2MJ0516–0445 is a T5.5 dwarf, and it is at a parallactic distance of 12 ± 2 pc. Faherty et al. (2012) measured its effective temperature $T_{eff} = 1211 \pm 137$ K, $log(g) = 5.02 \pm 0.48$ dex, and reported an age between $0.5 - 10$ Gyr. Faherty et al. (2012) estimated a mass of M= 47.18 ± 27.53 M_{jup} and R = 0.97 ± 0.17 R_{jup}. Metchev et al. (2015) measured its variability with the *Spitzer* telescope, finding no significant variability, but providing upper limits on its variability of A[3.6] < 0.83 % and A[4.5] < 0.81 %. J0516–04454 was found in the variable areas in 4 out of 12 our index-index plots, indicating that it is a non-variable candidate.

SDSSp J162414.37+002915.6

J1624+0029 is a T6.0 dwarf (Burgasser et al., 2002). Smart et al. (2013) provided the physical parameters for this object: $T_{eff} = 936 \pm 78$ K, $log(g) = 4.98 \pm 0.48$ dex, age between $0.5 - 10$ Gyr, M = 42.84 ± 26.06 M_{jup} and R = 0.94 ± 0.15 R_{jup}. Koen et al. (2004) and Radigan et al. (2014) did not find any significant variability for this object with ground-based near-infrared monitoring. On the other hand, Buenzli et al. (2014) found a tentative variability for 2M1624+0029 with HST/WFC3 data in the water band. J1624+0029 was

found in the variable areas in 5 out of 12 our index-index plots, indicating that it is a non-variable candidate.

2MASS J15462718–3325111

J1546–3325 is a T5.5 dwarf (Burgasser et al., 2002). Smart et al. (2013) derived some physical parameters for this object: $T_{eff} = 1002 \pm 84$ K, $log(g) = 5.00 \pm 0.48$ dex, age between $0.5 - 10$ Gyr, M $= 44.13 \pm 26.34$ M_{jup} y R $= 0.94 \pm 0.16$ R_{jup}. Koen et al. (2004) found no variability in the near-infrared after 4.4 hr of photometric monitoring. Similarly, Radigan et al. (2014) found no significant variability for J1516-3325 after 3.8 hr of J-band monitoring. J1546–3325 was found in the variable areas in 3 out of 12 our index-index plots, indicating that it is a non-variable candidate.

2MASSI J0243 137–245329

J0243–2453 is a T6 dwarf (Burgasser et al., 2002). Filippazzo et al. (2015) provided physical parameters for this object: $T_{eff} = 972 \pm 83$ K, $log(g) = 4.99 \pm 0.47$ dex, age around $0.5 - 10$ Gyr, M$= 43.59 \pm 26.41$ M_{jup} and R $= 0.94 \pm 0.16$ R_{jup}. Buenzli et al. (2014) found no variability $\sim$ 40 minutes near-infrared monitoring. Similarly, Radigan et al. (2014) did not find any significant variability in the J-band after 3.7 hr of monitoring. J0243–24532 was found in the variable areas in 4 out of 12 our index-index plots, indicating that it is a non-variable candidate.

2MASS J18283572-4849046

J1828–4849 is a T5.5 brown dwarf (Burgasser et al., 2000). Faherty et al. (2012) provided the most relevant physical parameters for this object: $T_{eff} = 1060 \pm 103$ K, $log(g) = 5.01 \pm 0.48$ dex, age between $0.5 - 10$ Gyr, M$= 45.21 \pm 27.07$ M_{jup} and R $= 0.95 \pm 0.16$ R_{jup}. Our spectral indices did not select J1828–4849 as a variable candidate, since it appeared only in 7 out of 12 variable areas. Nevertheless, Radigan et al. (2014) found significant variability for the object, with a variability amplitude of $0.9 \pm 0.1\%$, with a 5 hr rotational period. However, they found that the J1828–4849 light curve followed the same trend of a calibration star. Thus, it is possible that the variability measured for J1828–4849 is not intrinsic. Clarke et al. (2008) found an attenuation of 0.04 mag for the J1828–4849 light curve. Nevertheless, they found a strong correlation with the airmass, suggesting that the attenuation measured could be contamination from the control star they used. J1828–4849 was found in the variable areas in 6 out of 12 our index-index plots, indicating that it is a non-variable candidate.

SDSSp J111010+011613

J1110+0116 (Geballe et al., 2002) is a T5.5 brown dwarf, member of the 150 Myr old AB-Doradus moving group (Gagné et al., 2015). Vos et al. (2018) monitored it for 9 hr of observation with Spitzer in the [4.5] channel, detecting no variability. For periods <18 hr, they place an upper limit of 1.25% on the peak-to-peak variability amplitude of this object. J1110+0116 was found in the variable areas in 7 out of 12 our index-index plots, indicating that it is a non-variable candidate.

Bibliography

Allard F, Homeier D, Freytag B, Schaffenberger W, Rajpurohit AS. Progress in modeling very low mass stars, brown dwarfs, and planetary mass objects // arXiv preprint arXiv:1302.6559. 2013.

Allard France, Guillot Tristan, Ludwig Hans-Günter, Hauschildt Peter H, Schweitzer Andreas, Alexander David R, Ferguson Jason W. Model atmospheres and spectra: the role of dust // Symposium-International Astronomical Union. 211. 2003a. 325–332.

Allard NF, Allard F, Hauschildt PH, Kielkopf JF, Machin L. A new model for brown dwarf spectra including accurate unified line shape theory for the Na I and K I resonance line profiles // Astronomy & Astrophysics. 2003b. 411, 3. L473–L476.

Allers Katelyn N, Vos Johanna M, Biller Beth A, Williams Peter KG. A measurement of the wind speed on a brown dwarf // Science. 2020. 368, 6487. 169–172.

Apai D, Karalidi T, Marley MS, Yang H, Flateau D, Metchev S, Cowan NB, Buenzli Esther, Burgasser AJ, Radigan J, others . Zones, spots, and planetary-scale waves beating in brown dwarf atmospheres // Science. 2017. 357, 6352. 683–687.

Apai Daniel, Cowan Nicolas, Kopparapu Ravikumar, Kasper Markus, Hu Renyu, Morley Caroline, Fujii Yuka, Kane Stephen, Maley Mark, del Genio Anthony, Karalidi Theodora, Komacek Thaddeus, Mamajek Eric, Mandell Avi, Domagal-Goldman Shawn, Barman Travis, Boss Alan, Breckinridge James, Crossfield Ian, Danchi William, Ford Eric, Iro Nicolas, Kasting James, Lowrance Patrick, Madhusudhan Nikku, McElwain Michael, Moore William, Pascucci Ilaria, Plavchan Peter, Roberge Aki, Schneider Glenn, Showman Adam, Turnbull Margaret. Exploring Other Worlds: Science Questions for Future Direct Imaging Missions (EXOPAG SAG15 Report) // arXiv e-prints. VIII 2017. arXiv:1708.02821.

Apai Dániel, Kasper Markus, Skemer Andrew, Hanson Jake R, Lagrange Anne-Marie, Biller Beth A, Bonnefoy Mickaël, Buenzli Esther, Vigan Arthur. High-cadence, high-contrast imaging for exoplanet mapping: observations of the HR 8799 planets with VLT/SPHERE satellite-spot-corrected relative photometry // The Astrophysical Journal. 2016. 820, 1. 40.

Apai Dániel, Radigan Jacqueline, Buenzli Esther, Burrows Adam, Reid Iain Neill, Jayawardhana Ray. HST Spectral Mapping of L/T Transition Brown Dwarfs Reveals Cloud Thickness Variations // The Astrophysical Journal. V 2013. 768, 2. 121.

Apai Dániel, Radigan Jacqueline, Buenzli Esther, Burrows Adam, Reid Iain Neill, Jayawardhana Ray. HST spectral mapping of L/T transition brown dwarfs reveals cloud thickness variations // The Astrophysical Journal. 2013. 768, 2. 121.

Ashraf Afra, Bardalez Gagliuffi Daniella C, Manjavacas Elena, Vos Johanna M, Mechmann Claire, Faherty Jacqueline K. Disentangling the Signatures of Blended-Light Atmospheres in L/T Transition Brown Dwarfs // arXiv preprint arXiv:2206.09025. 2022.

Baraffe Isabelle, Chabrier Gilles, Allard France, Hauschildt Peter. Evolutionary models for solar metallicity low-mass stars: mass-magnitude relationships and color-magnitude diagrams // arXiv preprint astro-ph/9805009. 1998.

Baraffe Isabelle, Chabrier Gilles, Barman TS, Allard France, Hauschildt PH. Evolutionary models for cool brown dwarfs and extrasolar giant planets. The case of HD 209458 // Astronomy & Astrophysics. 2003. 402, 2. 701–712.

Bardalez Gagliuffi Daniella C., Burgasser Adam J., Gelino Christopher R., Looper Dagny L., Nicholls Christine P., Schmidt Sarah J., Cruz Kelle, West Andrew A., Gizis John E., Metchev Stanimir. SpeX Spectroscopy of Unresolved Very Low Mass Binaries. II. Identification of 14 Candidate Binaries with Late-M/Early-L and T Dwarf Components // The Astrophysical Journal. X 2014. 794, 2. 143.

Bardalez Gagliuffi Daniella C, Burgasser Adam J, Gelino Christopher R, Looper Dagny L, Nicholls Christine P, Schmidt Sarah J, Cruz Kelle, West Andrew A, Gizis John E, Metchev Stanimir. SpeX spectroscopy of unresolved very low mass binaries. II. Identification of 14 candidate binaries with late-M/early-L and T dwarf components // The Astrophysical Journal. 2014. 794, 2. 143.

Biller Beth A, Apai Dániel, Bonnefoy Mickaël, Desidera Silvano, Gratton Raffaele, Kasper Markus, Kenworthy Matthew, Lagrange Anne-Marie, Lazzoni Cecilia, Mesa Dino, others . A high-contrast search for variability in HR 8799bc with VLT-SPHERE // Monthly Notices of the Royal Astronomical Society. 2021. 503, 1. 743–767.

Biller Beth A., Vos Johanna, Buenzli Esther, Allers Katelyn, Bonnefoy Mickaël, Charnay Benjamin, Bézard Bruno, Allard France, Homeier Derek, Bonavita Mariangela, Brandner Wolfgang, Crossfield Ian, Dupuy Trent, Henning Thomas, Kopytova Taisiya, Liu Michael C., Manjavacas Elena, Schlieder Joshua. Simultaneous Multiwavelength Variability Characterization of the Free-floating Planetary-mass Object PSO J318.5-22 // Astronomical Journal. II 2018. 155, 2. 95.

Böhm-Vitense Erika. Über die wasserstoffkonvektionszone in sternen verschiedener effektivtemperaturen und leuchtkräfte. Mit 5 textabbildungen // Zeitschrift für Astrophysik, Vol. 46, p. 108. 1958. 46. 108.

Bonnefoy M., Chauvin G., Rojo P., Allard F., Lagrange A. M., Homeier D., Dumas C., Beuzit J. L. Near-infrared integral-field spectra of the planet/brown dwarf companion AB Pictoris b // Astronomy and Astrophysics. III 2010. 512. A52.

Bonnefoy M., Currie T., Marleau G. D., Schlieder J. E., Wisniewski J., Carson J., Covey K. R., Henning T., Biller B., Hinz P., Klahr H., Marsh Boyer A. N., Zimmerman N., Janson M., McElwain M., Mordasini C., Skemer A., Bailey V., Defrère D., Thalmann C., Skrutskie M., Allard F., Homeier D., Tamura M., Feldt M., Cumming A., Grady C., Brandner W., Helling C., Witte S., Hauschildt P., Kandori R., Kuzuhara M., Fukagawa M., Kwon J., Kudo T., Hashimoto J., Kusakabe N., Abe L., Brandt T., Egner S., Guyon O., Hayano Y., Hayashi M., Hayashi S., Hodapp K., Ishii M., Iye M., Knapp G., Matsuo T., Mede K., Miyama M., Morino J. I., Moro-Martin A., Nishimura T., Pyo T., Serabyn E., Suenaga T., Suto H., Suzuki R., Takahashi , Takami M., Takato N., Terada H., Tomono D., Turner E., Watanabe M., Yamada T., Takami H., Usuda T. Characterization of the gaseous companion κ Andromedae b. New Keck and LBTI high-contrast observations // Astronomy and Astrophysics. II 2014a. 562. A111.

Bonnefoy M., Marleau G. D., Galicher R., Beust H., Lagrange A. M., Baudino J. L., Chauvin G., Borgniet S., Meunier N., Rameau J., Boccaletti A., Cumming A., Helling C., Homeier D., Allard F., Delorme P. Physical and orbital properties of β Pictoris b // Astronomy and Astrophysics. VII 2014b. 567. L9.

Borysow A. Collision-induced absorption coefficients of H2 pairs at temperatures from 60 K to 1000 K // Astronomy & Astrophysics. 2002. 390, 2. 779–782.

Bowler Brendan P., Dupuy Trent J., Endl Michael, Cochran William D., MacQueen Phillip J., Fulton Benjamin J., Petigura Erik A., Howard Andrew W., Hirsch Lea, Kratter Kaitlin M., Crepp Justin R., Biller Beth A., Johnson Marshall C., Wittenmyer Robert A. Orbit and Dynamical Mass of the Late-T Dwarf GL 758 B // Astronomical Journal. IV 2018. 155, 4. 159.

Bowler Brendan P, Liu Michael C, Shkolnik Evgenya L, Dupuy Trent J. Planets around low-mass stars. III. A young dusty L dwarf companion at the deuterium-burning limit // The Astrophysical Journal. 2013. 774, 1. 55.

Buenzli Esther, Apai Dániel, Morley Caroline V, Flateau Davin, Showman Adam P, Burrows Adam, Marley Mark S, Lewis Nikole K, Reid I Neill. Vertical atmospheric structure in a variable brown dwarf: Pressure-dependent phase shifts in simultaneous Hubble Space Telescope-Spitzer light curves // The Astrophysical Journal Letters. 2012. 760, 2. L31.

Buenzli Esther, Apai Dániel, Radigan Jacqueline, Reid I Neill, Flateau Davin. Brown dwarf photospheres are patchy: a hubble space telescope near-infrared spectroscopic survey finds frequent low-level variability // The Astrophysical Journal. 2014. 782, 2. 77.

Burgasser Adam J. SDSS J080531.84+481233.0: An Unresolved L Dwarf/T Dwarf Binary // Astronomical Journal. X 2007. 134, 4. 1330–1336.

Burgasser Adam J, Cruz Kelle L, Cushing Michael, Gelino Christopher R, Looper Dagny L, Faherty Jacqueline K, Kirkpatrick J Davy, Reid I Neill. SpeX Spectroscopy of unresolved very low mass binaries. I. Identification of 17 candidate binaries straddling the L dwarf/T dwarf transition // The Astrophysical Journal. 2010a. 710, 2. 1142.

Burgasser Adam J, Kirkpatrick J Davy, Brown Michael E, Reid I Neill, Burrows Adam, Liebert James, Matthews Keith, Gizis John E, Dahn Conard C, Monet David G, others . The spectra of T dwarfs. I. Near-infrared data and spectral classification // The Astrophysical Journal. 2002. 564, 1. 421.

Burgasser Adam J, Kirkpatrick J Davy, Cruz Kelle L, Reid I Neill, Leggett Sandy K, Liebert James, Burrows Adam, Brown Michael E. Hubble Space Telescope NICMOS observations of T dwarfs: Brown dwarf multiplicity and new probes of the L/T transition // The Astrophysical Journal Supplement Series. 2006. 166, 2. 585.

Burgasser Adam J, Kirkpatrick J Davy, Cutri Roc M, McCallon Howard, Kopan Gene, Gizis John E, Liebert James, Reid I Neill, Brown Michael E, Monet David G, others . Discovery of a brown dwarf companion to gliese 570abc: A 2mass t dwarf significantly cooler than gliese 229b // The Astrophysical Journal. 2000. 531, 1. L57.

Burgasser Adam J., Kirkpatrick J. Davy, Reid I. Neill, Brown Michael E., Miskey Cherie L., Gizis John E. Binarity in Brown Dwarfs: T Dwarf Binaries Discovered with the Hubble Space Telescope Wide Field Planetary Camera 2 // The Astrophysical Journal. III 2003. 586, 1. 512–526.

Burgasser Adam J, McElwain Michael W, Kirkpatrick J Davy. The 2MASS wide-field T dwarf search. II. Discovery of three T dwarfs in the southern hemisphere // The Astronomical Journal. 2003. 126, 5. 2487.

Burgasser Adam J, McElwain Michael W, Kirkpatrick J Davy, Cruz Kelle L, Tinney Chris G, Reid I Neill. The 2MASS wide-field T dwarf search. III. Seven new T dwarfs and other cool dwarf discoveries // The Astronomical Journal. 2004. 127, 5. 2856.

Burgasser Adam J, Simcoe Robert A, Bochanski John J, Saumon Didier, Mamajek Eric E, Cushing Michael C, Marley Mark S, McMurtry Craig, Pipher Judith L,

Forrest William J. Clouds in the coldest brown dwarfs: FIRE spectroscopy of Ross 458C // The Astrophysical Journal. 2010b. 725, 2. 1405.

Burningham Ben, Faherty Jacqueline K, Gonzales Eileen C, Marley Mark S, Visscher Channon, Lupu Roxana, Gaarn Josefine, Fabienne Bieger Michelle, Freedman Richard, Saumon Didier. Cloud busting: enstatite and quartz clouds in the atmosphere of 2M2224-0158 // Monthly Notices of the Royal Astronomical Society. 2021. 506, 2. 1944–1961.

Burningham Ben, Marley Mark S, Line Michael R, Lupu Roxana, Visscher Channon, Morley Caroline V, Saumon Didier, Freedman Richard. Retrieval of atmospheric properties of cloudy L dwarfs // Monthly Notices of the Royal Astronomical Society. 2017. 470, 1. 1177–1197.

Burrows Adam, Hubbard WB, Lunine JI, Liebert James. The theory of brown dwarfs and extrasolar giant planets // Reviews of modern physics. 2001. 73, 3. 719.

Burrows Adam, Sudarsky David, Lunine Jonathan I. Beyond the T dwarfs: Theoretical spectra, colors, and detectability of the coolest brown dwarfs // The Astrophysical Journal. 2003. 596, 1. 587.

Burrows Adam, Volobuyev Maxim. Calculations of the far-wing line profiles of sodium and potassium in the atmospheres of substellar-mass objects // The Astrophysical Journal. 2003. 583, 2. 985.

Carson J., Thalmann C., Janson M., Kozakis T., Bonnefoy M., Biller B., Schlieder J., Currie T., McElwain M., Goto M., Henning T., Brandner W., Feldt M., Kandori R., Kuzuhara M., Stevens L., Wong P., Gainey K., Fukagawa M., Kuwada Y., Brandt T., Kwon J., Abe L., Egner S., Grady C., Guyon O., Hashimoto J., Hayano Y., Hayashi M., Hayashi S., Hodapp K., Ishii M., Iye M., Knapp G., Kudo T., Kusakabe N., Matsuo T., Miyama S., Morino J., Moro-Martin A., Nishimura T., Pyo T., Serabyn E., Suto H., Suzuki R., Takami M., Takato N., Terada H., Tomono D., Turner E., Watanabe M., Wisniewski J., Yamada T., Takami H., Usuda T., Tamura M. Direct Imaging Discovery of a "Super-Jupiter" around the Late B-type Star κ And // The Astrophysical Journal, Letters to the Editor. II 2013. 763, 2. L32.

Chabrier Gilles, Baraffe Isabelle. Structure and evolution of low-mass stars // arXiv preprint astro-ph/9704118. 1997.

Chabrier Gilles, Baraffe Isabelle. Theory of low-mass stars and substellar objects // Annual Review of Astronomy and Astrophysics. 2000. 38, 1. 337–377.

Chabrier Gilles, Johansen Anders, Janson Markus, Rafikov Roman. Giant planet and brown dwarf formation // arXiv preprint arXiv:1401.7559. 2014.

Chauvin G., Desidera S., Lagrange A. M., Vigan A., Gratton R., Langlois M., Bonnefoy M., Beuzit J. L., Feldt M., Mouillet D., Meyer M., Cheetham A., Biller

B., Boccaletti A., D'Orazi V., Galicher R., Hagelberg J., Maire A. L., Mesa D., Olofsson J., Samland M., Schmidt T. O. B., Sissa E., Bonavita M., Charnay B., Cudel M., Daemgen S., Delorme P., Janin-Potiron P., Janson M., Keppler M., Le Coroller H., Ligi R., Marleau G. D., Messina S., Mollière P., Mordasini C., Müller A., Peretti S., Perrot C., Rodet L., Rouan D., Zurlo A., Dominik C., Henning T., Menard F., Schmid H. M., Turatto M., Udry S., Vakili F., Abe L., Antichi J., Baruffolo A., Baudoz P., Baudrand J., Blanchard P., Bazzon A., Buey T., Carbillet M., Carle M., Charton J., Cascone E., Claudi R., Costille A., Deboulbe A., De Caprio V., Dohlen K., Fantinel D., Feautrier P., Fusco T., Gigan P., Giro E., Gisler D., Gluck L., Hubin N., Hugot E., Jaquet M., Kasper M., Madec F., Magnard Y., Martinez P., Maurel D., Le Mignant D., Möller-Nilsson O., Llored M., Moulin T., Origné A., Pavlov A., Perret D., Petit C., Pragt J., Puget P., Rabou P., Ramos J., Rigal R., Rochat S., Roelfsema R., Rousset G., Roux A., Salasnich B., Sauvage J. F., Sevin A., Soenke C., Stadler E., Suarez M., Weber L., Wildi F., Antoniucci S., Augereau J. C., Baudino J. L., Brandner W., Engler N., Girard J., Gry C., Kral Q., Kopytova T., Lagadec E., Milli J., Moutou C., Schlieder J., Szulágyi J., Thalmann C., Wahhaj Z. Discovery of a warm, dusty giant planet around HIP 65426 // Astronomy and Astrophysics. IX 2017. 605. L9.

Chauvin G., Lagrange A. M., Zuckerman B., Dumas C., Mouillet D., Song I., Beuzit J. L., Lowrance P., Bessell M. S. A companion to AB Pic at the planet/brown dwarf boundary // Astronomy and Astrophysics. VIII 2005. 438, 3. L29–L32.

Cheetham A., Ségransan D., Peretti S., Delisle J. B., Hagelberg J., Beuzit J. L., Forveille T., Marmier M., Udry S., Wildi F. Direct imaging of an ultracool substellar companion to the exoplanet host star HD 4113 A // Astronomy and Astrophysics. VI 2018. 614. A16.

Clarke FJ, Hodgkin ST, Oppenheimer BR, Robertson J, Haubois X. A search for J-band variability from late-L and T brown dwarfs // Monthly Notices of the Royal Astronomical Society. 2008. 386, 4. 2009–2014.

Croll Bryce, Muirhead Philip S., Han Eunkyu, Dalba Paul A., Radigan Jacqueline, Morley Caroline V., Lazarevic Marko, Taylor Brian. Long-term, Multiwavelength Light Curves of Ultra-cool Dwarfs: I. An Interplay of Starspots Clouds Likely Drive the Variability of the L3.5 dwarf 2MASS 0036+18. 2016.

Cruz Kelle L, Reid I Neill, Kirkpatrick J Davy, Burgasser Adam J, Liebert James, Solomon Adam R, Schmidt Sarah J, Allen Peter R, Hawley Suzanne L, Covey Kevin R. Meeting the cool neighbors. IX. The luminosity function of M7-L8 ultracool dwarfs in the field // The Astronomical Journal. 2007. 133, 2. 439.

Cruz Kelle L, Reid I Neill, Liebert James, Kirkpatrick J Davy, Lowrance Patrick J. Meeting the cool neighbors. V. A 2MASS-selected sample of ultracool dwarfs // The Astronomical Journal. 2003. 126, 5. 2421.

Cushing Michael C, Rayner John T, Vacca William D. An infrared spectroscopic sequence of M, L, and T dwarfs // The Astrophysical Journal. 2005. 623, 2. 1115.

Dupuy Trent J, Liu Michael C. The Hawaii infrared parallax program. I. Ultracool binaries and the L/T transition // The Astrophysical Journal Supplement Series. 2012. 201, 2. 19.

Enoch Melissa L, Brown Michael E, Burgasser Adam J. Photometric variability at the L/T dwarf boundary // The Astronomical Journal. 2003. 126, 2. 1006.

Faherty Jacqueline K, Burgasser Adam J, Walter Frederick M, Bliek Nicole Van der, Shara Michael M, Cruz Kelle L, West Andrew A, Vrba Frederick J, Angladа-Escudé Guillem. The brown dwarf Kinematics Project (BDKP). III. Parallaxes for 70 ultracool dwarfs // The Astrophysical Journal. 2012. 752, 1. 56.

Faherty Jacqueline K, Burgasser Adam J, West Andrew A, Bochanski John J, Cruz Kelle L, Shara Michael M, Walter Frederick M. The brown dwarf kinematics project. II. Details on nine wide common proper motion very low mass companions to nearby stars // The Astronomical Journal. 2009. 139, 1. 176.

Faherty Jacqueline K., Riedel Adric R., Cruz Kelle L., Gagne Jonathan, Filippazzo Joseph C., Lambrides Erini, Fica Haley, Weinberger Alycia, Thorstensen John R., Tinney C. G., Baldassare Vivienne, Lemonier Emily, Rice Emily L. Population Properties of Brown Dwarf Analogs to Exoplanets // The Astrophysical Journal Supplement Series. VII 2016. 225, 1. 10.

Faherty Jacqueline K, Riedel Adric R, Cruz Kelle L, Gagne Jonathan, Filippazzo Joseph C, Lambrides Erini, Fica Haley, Weinberger Alycia, Thorstensen John R, Tinney CG, others . Population properties of brown dwarf analogs to exoplanets // The Astrophysical Journal Supplement Series. 2016. 225, 1. 10.

Fegley Jr. B., Prinn R. G. Equilibrium and nonequilibrium chemistry of Saturn's atmosphere - Implications for the observability of PH3, N2, CO, and GeH4. // The Astrophysical Journal. XII 1985. 299. 1067–1078.

Filippazzo Joseph C, Rice Emily L, Faherty Jacqueline, Cruz Kelle L, Van Gordon Mollie M, Looper Dagny L. Fundamental parameters and spectral energy distributions of young and field age objects with masses spanning the stellar to planetary regime // The Astrophysical Journal. 2015. 810, 2. 158.

Folkes Stuart L, Pinfield David J, Kendall Tim R, Jones Hugh RA. Discovery of a nearby L–T transition object in the Southern Galactic plane // Monthly Notices of the Royal Astronomical Society. 2007. 378, 3. 901–909.

Gagné Jonathan, Burgasser Adam J., Faherty Jacqueline K., Lafreniére David, Doyon René, Filippazzo Joseph C., Bowsher Emily, Nicholls Christine P. SDSS J111010.01+011613.1: A New Planetary-mass T Dwarf Member of the AB Doradus Moving Group // The Astrophysical Journal, Letters to the Editor. VII 2015. 808, 1. L20.

Gagné Jonathan, Faherty Jacqueline K, Cruz Kelle L, Lafreniére David, Doyon René, Malo Lison, Burgasser Adam J, Naud Marie-Eve, Artigau Étienne, Bouchard Sandie, others . BANYAN. VII. A new population of young substellar candidate members of nearby moving groups from the BASS survey // The Astrophysical Journal Supplement Series. 2015. 219, 2. 33.

Gagné Jonathan, Lafrenière David, Doyon René, Malo Lison, Artigau Étienne. BANYAN. II. Very low mass and substellar candidate members to nearby, young kinematic groups with previously known signs of youth // The Astrophysical Journal. 2014. 783, 2. 121.

Gaia Collaboration . VizieR Online Data Catalog: Gaia EDR3 (Gaia Collaboration, 2020) // VizieR Online Data Catalog. XI 2020. I/350.

Geballe TR, Knapp GR, Leggett SK, Fan X, Golimowski DA, Anderson S, Brinkmann J, Csabai I, Gunn JE, Hawley SL, others . Toward spectral classification of L and T dwarfs: Infrared and optical spectroscopy and analysis // The Astrophysical Journal. 2002. 564, 1. 466.

Gelino Christopher R, Marley Mark S, Holtzman Jon A, Ackerman Andrew S, Lodders Katharina. L dwarf variability: I-band observations // The Astrophysical Journal. 2002. 577, 1. 433.

Gizis John E, Allers Katelyn N, Liu Michael C, Harris Hugh C, Faherty Jacqueline K, Burgasser Adam J, Kirkpatrick J Davy. WISEP J004701. 06+ 680352.1: An intermediate surface gravity, dusty brown dwarf in the AB Dor Moving Group // The Astrophysical Journal. 2015. 799, 2. 203.

Gizis John E, Reid I Neill, Hawley Suzanne L. The Palomar/MSU nearby star spectroscopic survey. III. Chromospheric activity, M dwarf ages, and the local star formation history // The Astronomical Journal. 2002. 123, 6. 3356.

Golimowski David A, Leggett SK, Marley MS, Fan X, Geballe TR, Knapp GR, Vrba FJ, Henden AA, Luginbuhl CB, Guetter HH, others . L and M photometry of ultracool dwarfs // The Astronomical Journal. 2004. 127, 6. 3516.

Hayashi Chushiro, Nakano Takenori. Evolution of stars of small masses in the premain-sequence stages // Progress of Theoretical Physics. 1963. 30, 4. 460–474.

Helling Christiane, Dehn Matthias, Woitke Peter, Hauschildt Peter H. Consistent simulations of substellar atmospheres and nonequilibrium dust cloud formation // The Astrophysical Journal. 2008. 675, 2. L105.

Joergens Viki. 50 Years of Brown Dwarfs. 2016.

Karalidi Theodora, Apai Dániel, Schneider Glenn, Hanson Jake R., Pasachoff Jay M. Aeolus: A Markov Chain Monte Carlo Code for Mapping Ultracool Atmospheres. An Application on Jupiter and Brown Dwarf HST Light Curves // The Astrophysical Journal. XI 2015. 814, 1. 65.

Karalidi Theodora, Apai Dániel, Schneider Glenn, Hanson Jake R, Pasachoff Jay M. Aeolus: A Markov chain Monte Carlo code for mapping ultracool atmospheres. An application on Jupiter and brown dwarf HST light curves // The Astrophysical Journal. 2015. 814, 1. 65.

Karalidi Theodora, Marley Mark, Fortney Jonathan, Morley Caroline, Saumon Didier, Lupu Roxana, Visscher Channon, Freedman Richard. Sonora Cholla: A Grid of Cloud-free, Solar Metallicity Models in Chemical Disequilibrium for the JWST Era. X 2021.

Khandrika Harish, Burgasser Adam J, Melis Carl, Luk Christopher, Bowsher Emily, Swift Brandon. A search for photometric variability in L-and T-type brown dwarf atmospheres // The Astronomical Journal. 2013. 145, 3. 71.

Kirkpatrick J Davy. New spectral types L and T // Annu. Rev. Astron. Astrophys. 2005. 43. 195–245.

Kirkpatrick J Davy, Cushing Michael C, Gelino Chr istopher R, Griffith Roger L, Skrutskie Michael F, Marsh Kenneth A, Wright Edward L, Mainzer A, Eisenhardt Peter R, McLean Ian S, others . The first hundred brown dwarfs discovered by the Wide-Field Infrared Survey Explorer (WISE) // The Astrophysical Journal Supplement Series. 2011. 197, 2. 19.

Kirkpatrick J. Davy, Gelino Christopher R., Faherty Jacqueline K., Meisner Aaron M., Caselden Dan, Schneider Adam C., Marocco Federico, Cayago Alfred J., Smart R. L., Eisenhardt Peter R., Kuchner Marc J., Wright Edward L., Cushing Michael C., Allers Katelyn N., Bardalez Gagliuffi Daniella C., Burgasser Adam J., Gagné Jonathan, Logsdon Sarah E., Martin Emily C., Ingalls James G., Lowrance Patrick J., Abrahams Ellianna S., Aganze Christian, Gerasimov Roman, Gonzales Eileen C., Hsu Chih-Chun, Kamraj Nikita, Kiman Rocio, Rees Jon, Theissen Christopher, Ammar Kareem, Andersen Nikolaj Stevnbak, Beaulieu Paul, Colin Guillaume, Elachi Charles A., Goodman Samuel J., Gramaize Léopold, Hamlet Leslie K., Hong Justin, Jonkeren Alexander, Khalil Mohammed, Martin David W., Pendrill William, Pumphrey Benjamin, Rothermich Austin, Sainio Arttu, Stenner Andres, Tanner Christopher, Thévenot Melina, Voloshin Nikita V., Walla Jim, Wedracki Zbigniew, Backyard Worlds: Planet 9 Collaboration . The Field Substellar Mass Function Based on the Full-sky 20 pc Census of 525 L, T, and Y Dwarfs // The Astrophysical Journal Supplement Series. III 2021. 253, 1. 7.

Kirkpatrick J Davy, Reid I Neill, Liebert James, Gizis John E, Burgasser Adam J, Monet David G, Dahn Conard C, Nelson Brant, Williams Rik J. 67 additional L dwarfs discovered by the Two Micron All Sky Survey // The Astronomical Journal. 2000. 120, 1. 447.

Kitzmann Daniel, Heng Kevin, Oreshenko Maria, Grimm Simon L, Apai Dániel, Bowler Brendan P, Burgasser Adam J, Marley Mark S. Helios-r2: a new bayesian,

open-source retrieval model for brown dwarfs and exoplanet atmospheres // The Astrophysical Journal. 2020. 890, 2. 174.

Knapp GR, Leggett Sandy K, Fan X, Marley MS, Geballe TR, Golimowski DA, Finkbeiner Douglas, Gunn JE, Hennawi J, Ivezić Z, others . Near-infrared photometry and spectroscopy of L and T dwarfs: The effects of temperature, clouds, and gravity // The Astronomical Journal. 2004. 127, 6. 3553.

Koen C, Matsunaga N, Menzies J. A search for short time-scale JHK variability in ultracool dwarfs // Monthly Notices of the Royal Astronomical Society. 2004. 354, 2. 466–476.

Koen Chris. A search for short time-scale I-band variability in ultracool dwarfs // Monthly Notices of the Royal Astronomical Society. 2003. 346, 2. 473–482.

Kumar Shiv S. The structure of stars of very low mass. // The Astrophysical Journal. 1963. 137. 1121.

Lagrange A. M., Gratadour D., Chauvin G., Fusco T., Ehrenreich D., Mouillet D., Rousset G., Rouan D., Allard F., Gendron É., Charton J., Mugnier L., Rabou P., Montri J., Lacombe F. A probable giant planet imaged in the β Pictoris disk. VLT/NaCo deep L'-band imaging // Astronomy and Astrophysics. I 2009. 493, 2. L21–L25.

Linsky Jeffrey L. On the pressure-induced opacity of molecular hydrogen in late-type stars // Astrophysical Journal, vol. 156, p. 989. 1969. 156. 989.

Liu Michael C, Dupuy Trent J, Allers Katelyn N. The Hawaii infrared parallax program. II. Young ultracool field dwarfs // The Astrophysical Journal. 2016. 833, 1. 96.

Lodders Katharina. Solar system abundances and condensation temperatures of the elements // The Astrophysical Journal. 2003. 591, 2. 1220.

Lodders Katharina, Fegley Jr Bruce. Atmospheric chemistry in giant planets, brown dwarfs, and low-mass dwarf stars: I. Carbon, nitrogen, and oxygen // Icarus. 2002. 155, 2. 393–424.

Looper Dagny L, Kirkpatrick J Davy, Cutri Roc M, Barman Travis, Burgasser Adam J, Cushing Michael C, Roellig Thomas, McGovern Mark R, McLean Ian S, Rice Emily, others . Discovery of two nearby peculiar L dwarfs from the 2MASS proper-motion survey: Young or metal-rich? // The Astrophysical Journal. 2008. 686, 1. 528.

Lueber Anna, Kitzmann Daniel, Bowler Brendan P, Burgasser Adam J, Heng Kevin. Retrieval Study of Brown Dwarfs across the LT Sequence // The Astrophysical Journal. 2022. 930, 2. 136.

Luger Rodrigo, Agol Eric, Foreman-Mackey Daniel, Fleming David P., Lustig-Yaeger Jacob, Deitrick Russell. starry: Analytic Occultation Light Curves // Astronomical Journal. II 2019a. 157, 2. 64.

Luger Rodrigo, Agol Eric, Foreman-Mackey Daniel, Fleming David P., Lustig-Yaeger Jacob, Deitrick Russell. starry: Analytic Occultation Light Curves // Astronomical Journal. II 2019b. 157, 2. 64.

Luhman Kevin L. The formation and early evolution of low-mass stars and brown dwarfs // Annual Review of Astronomy and Astrophysics. 2012. 50. 65–106.

Macintosh B., Graham J. R., Barman T., De Rosa R. J., Konopacky Q., Marley M. S., Marois C., Nielsen E. L., Pueyo L., Rajan A., Rameau J., Saumon D., Wang J. J., Patience J., Ammons M., Arriaga P., Artigau E., Beckwith S., Brewster J., Bruzzone S., Bulger J., Burningham B., Burrows A. S., Chen C., Chiang E., Chilcote J. K., Dawson R. I., Dong R., Doyon R., Draper Z. H., Duchêne G., Esposito T. M., Fabrycky D., Fitzgerald M. P., Follette K. B., Fortney J. J., Gerard B., Goodsell S., Greenbaum A. Z., Hibon P., Hinkley S., Cotten T. H., Hung L. W., Ingraham P., Johnson-Groh M., Kalas P., Lafreniere D., Larkin J. E., Lee J., Line M., Long D., Maire J., Marchis F., Matthews B. C., Max C. E., Metchev S., Millar-Blanchaer M. A., Mittal T., Morley C. V., Morzinski K. M., Murray-Clay R., Oppenheimer R., Palmer D. W., Patel R., Perrin M. D., Poyneer L. A., Rafikov R. R., Rantakyrö F. T., Rice E. L., Rojo P., Rudy A. R., Ruffio J. B., Ruiz M. T., Sadakuni N., Saddlemyer L., Salama M., Savransky D., Schneider A. C., Sivaramakrishnan A., Song I., Soummer R., Thomas S., Vasisht G., Wallace J. K., Ward-Duong K., Wiktorowicz S. J., Wolff S. G., Zuckerman B. Discovery and spectroscopy of the young jovian planet 51 Eri b with the Gemini Planet Imager // Science. X 2015. 350, 6256. 64–67.

Manjavacas Elena, Apai Dániel, Lew Ben WP, Zhou Yifan, Schneider Glenn, Burgasser Adam J, Karalidi Theodora, Miles-Páez Paulo A, Lowrance Patrick J, Cowan Nicolas, others . Cloud Atlas: Rotational Spectral Modulations and Potential Sulfide Clouds in the Planetary-mass, Late T-type Companion Ross 458C // The Astrophysical Journal Letters. 2019. 875, 2. L15.

Manjavacas Elena, Apai Dániel, Zhou Yifan, Karalidi Theodora, Lew Ben WP, Schneider Glenn, Cowan Nicolas, Metchev Stan, Miles-Páez Paulo A, Burgasser Adam J, others . Cloud Atlas: Discovery of Rotational Spectral Modulations in a Low-mass, L-type Brown Dwarf Companion to a Star // The Astronomical Journal. 2018. 155, 1. 11.

Manjavacas Elena, Karalidi Theodora, Tan Xianyu, Vos Johanna M., Lew Ben W. P., Biller Beth A., Oliveros-Gómez Natalia. Top-of-the-atmosphere and Vertical Cloud Structure of a Fast-rotating Late T Dwarf // Astronomical Journal. VIII 2022. 164, 2. 65.

Manjavacas Elena, Karalidi Theodora, Vos Johanna M, Biller Beth A, Lew Ben WP. Revealing the Vertical Cloud Structure of a Young Low-mass Brown Dwarf, an Analog to the β-Pictoris b Directly Imaged Exoplanet, through Keck I/MOSFIRE Spectrophotometric Variability // The Astronomical Journal. 2021. 162, 5. 179.

Marley Mark, Saumon Didier, Morley Caroline, Fortney Jonathan, Visscher Channon, Freedman Richard, Lupu Roxana. Sonora Bobcat: cloud-free, substellar atmosphere models, spectra, photometry, evolution, and chemistry. VII 2021.

Marley Mark S, Robinson Tyler D. On the cool side: modeling the atmospheres of brown dwarfs and giant planets // Annual Review of Astronomy and Astrophysics. 2015. 53. 279–323.

Marley Mark S, Seager S, Saumon D, Lodders Katharina, Ackerman Andrew S, Freedman Richard S, Fan Xiaohui. Clouds and chemistry: Ultracool dwarf atmospheric properties from optical and infrared colors // The Astrophysical Journal. 2002. 568, 1. 335.

Metchev Stanimir A, Heinze Aren, Apai Dániel, Flateau Davin, Radigan Jacqueline, Burgasser Adam, Marley Mark S, Artigau Étienne, Plavchan Peter, Goldman Bertrand. Weather on other worlds. II. Survey results: Spots are ubiquitous on L and T dwarfs // The Astrophysical Journal. 2015. 799, 2. 154.

Miret-Roig Núria, Bouy Hervé, Raymond Sean N, Tamura Motohide, Bertin Emmanuel, Barrado David, Olivares Javier, Galli Phillip AB, Cuillandre Jean-Charles, Sarro Luis Manuel, others . A rich population of free-floating planets in the Upper Scorpius young stellar association // Nature Astronomy. 2022. 6, 1. 89–97.

Molaverdikhani Karan, Henning Thomas, Mollière Paul. From cold to hot irradiated gaseous exoplanets: Toward an observation-based classification scheme // The Astrophysical Journal. 2019. 873, 1. 32.

Mollière Paul, Boekel Roy van, Dullemond C, Henning Th, Mordasini Christoph. Model atmospheres of irradiated exoplanets: the influence of stellar parameters, metallicity, and the C/O ratio // The Astrophysical Journal. 2015. 813, 1. 47.

Morales-Calderón M, Stauffer JR, Kirkpatrick J Davy, Carey S, Gelino CR, Navascués D Barrado y, Rebull L, Lowrance P, Marley MS, Charbonneau D, others . A sensitive search for variability in late L dwarfs: the quest for weather // The Astrophysical Journal. 2006. 653, 2. 1454.

Nakajima T, Oppenheimer BR, Kulkarni SR, Golimowski DA, Matthews K, Durrance ST. Discovery of a cool brown dwarf // nature. 1995. 378, 6556. 463–465.

Oliveros-Gomez Natalia, Manjavacas Elena, Ashraf Afra, Bardalez Gagliuffi Daniella C, Vos Johanna M, Faherty Jacqueline K, Karalidi Theodora, Apai Daniel. Informed Systematic Method to Identify Variable Mid-and Late-T Dwarfs // The Astrophysical Journal. 2022. 939, 2. 72.

Oppenheimer BR, Kulkarni SR, Matthews K, Nakajima T. Infrared spectrum of the cool brown dwarf Gl 229B // Science. 1995. 270, 5241. 1478–1479.

Osorio MR Zapatero, Caballero JA, Béjar VJS. Optical linear polarization of late M and L type dwarfs // The Astrophysical Journal. 2005. 621, 1. 445.

Pedregosa F., Varoquaux G., Gramfort A., Michel V., Thirion B., Grisel O., Blondel M., Prettenhofer P., Weiss R., Dubourg V., Vanderplas J., Passos A., Cournapeau D., Brucher M., Perrot M., Duchesnay E. Scikit-learn: Machine Learning in Python // Journal of Machine Learning Research. 2011. 12. 2825–2830.

Petrus Simon, Chauvin Gaël, Bonnefoy M, Tremblin Pascal, Charnay B, Delorme P, Marleau G-D, Bayo Amelia, Manjavacas Elena, Lagrange A-M, others . X-SHYNE: X-shooter spectra of young exoplanet analogs-I. A medium-resolution 0.65–2.5 μm one-shot spectrum of VHS 1256- 1257 b // Astronomy & Astrophysics. 2023. 670. L9.

Phan-Bao N, Bessell MS, Martín EL, Simon Grégory, Borsenberger J, Tata R, Guibert J, Crifo F, Forveille T, Delfosse X, others . Discovery of new nearby L and late-M dwarfs at low Galactic latitude from the DENIS data base // Monthly Notices of the Royal Astronomical Society. 2008. 383, 3. 831–844.

Phillips Mark W, Tremblin Pascal, Baraffe Isabelle, Chabrier Gilles, Allard Nicole F, Spiegelman Fernand, Goyal Jayesh M, Drummond Ben, Hebrard Eric. A new set of atmosphere and evolution models for cool T–Y brown dwarfs and giant exoplanets // Astronomy & Astrophysics. 2020. 637. A38.

Prandtl Ludwig. Applications of modern hydrodynamics to aeronautics. 1925.

Radigan Jacqueline. An independent analysis of the brown dwarf atmosphere monitoring (BAM) data: large-amplitude variability is rare outside the L/T transition // The Astrophysical Journal. 2014. 797, 2. 120.

Radigan Jacqueline, Lafrenière David, Jayawardhana Ray, Artigau Etienne. Strong brightness variations signal cloudy-to-clear transition of brown dwarfs // The Astrophysical Journal. 2014. 793, 2. 75.

Rebolo Rafael, Osorio MR Zapatero, Martín EL. Discovery of a brown dwarf in the Pleiades star cluster // Nature. 1995. 377, 6545. 129–131.

Reid I Neill, Cruz Kelle L, Kirkpatrick J Davy, Allen Peter R, Mungall F, Liebert James, Lowrance Patrick, Sweet Anne. Meeting the cool neighbors. X. Ultracool dwarfs from the 2MASS all-sky data release // The Astronomical Journal. 2008. 136, 3. 1290.

Reid I Neill, Kirkpatrick J Davy, Gizis JE, Dahn CC, Monet DG, Williams Rik J, Liebert James, Burgasser AJ. Four nearby L dwarfs // The Astronomical Journal. 2000. 119, 1. 369.

Reid I Neill, Walkowicz Lucianne M. LP 261-75/2MASSW J09510549+ 3558021: A Young, Wide M4. 5/L6 Binary1 // Publications of the Astronomical Society of the Pacific. 2006. 118, 843. 671.

Saumon D, Bergeron Po, Lunine JI, Hubbard W Bo, Burrows A. Cool zero-metallicity stellar atmospheres // Astrophysical Journal, Part 1 (ISSN 0004-637X), vol. 424, no. 1, p. 333-344. 1994. 424. 333–344.

Saumon D., Marley M. S. The Evolution of L and T Dwarfs in Color-Magnitude Diagrams // The Astrophysical Journal. XII 2008. 689. 1327–1344.

Schmidt Sarah J, West Andrew A, Hawley Suzanne L, Pineda J Sebastian. Colors and kinematics of l dwarfs from the sloan digital sky survey // The Astronomical Journal. 2010. 139, 5. 1808.

Schneider Adam C, Cushing Michael C, Kirkpatrick J Davy, Mace Gregory N, Gelino Christopher R, Faherty Jacqueline K, Fajardo-Acosta Sergio, Sheppard Scott S. Discovery of the Young L Dwarf WISE J174102. 78- 464225.5 // The Astronomical Journal. 2014. 147, 2. 34.

Smart RL, Tinney CG, Bucciarelli B, Marocco F, Abbas U, Andrei A, Bernardi G, Burningham B, Cardoso C, Costa E, others . NPARSEC: NTT Parallaxes of Southern Extremely Cool objects. Goals, targets, procedures and first results // Monthly Notices of the Royal Astronomical Society. 2013. 433, 3. 2054–2063.

Tan Xianyu, Showman Adam P. Atmospheric circulation of brown dwarfs and directly imaged exoplanets driven by cloud radiative feedback: effects of rotation // Monthly Notices of the Royal Astronomical Society. III 2021. 502, 1. 678–699.

Tannock Megan E, Metchev Stanimir, Heinze Aren, Miles-Páez Paulo A, Gagné Jonathan, Burgasser Adam, Marley Mark S, Apai Dániel, Suárez Genaro, Plavchan Peter. Weather on Other Worlds. V. The Three Most Rapidly Rotating Ultra-cool Dwarfs // The Astronomical Journal. 2021. 161, 5. 224.

Tremblin Pascal. Thermo-compositional diabatic convection in the atmospheres of brown dwarfs, exoplanets, and in Earth's atmosphere and oceans // AAS/Division for Extreme Solar Systems Abstracts. 2019. 51. 327–02.

Tremblin Pascal, Amundsen David S, Mourier P, Baraffe I, Chabrier G, Drummond B, Homeier D, Venot Olivia. Fingering convection and cloudless models for cool brown dwarf atmospheres // The Astrophysical Journal Letters. 2015. 804, 1. L17.

Tremblin Pascal, Amundsen David Skålid, Chabrier G, Baraffe I, Drummond B, Hinkley Sasha, Mourier P, Venot Olivia. Cloudless atmospheres for L/T dwarfs and extrasolar giant planets // The Astrophysical journal letters. 2016. 817, 2. L19.

Vos Johanna M, Allers Katelyn N, Biller Beth A, Liu Michael C, Dupuy Trent J, Gallimore Jack F, Adenuga Iyadunni J, Best William MJ. Variability of the lowest mass objects in the AB Doradus moving group // Monthly Notices of the Royal Astronomical Society. 2018. 474, 1. 1041–1053.

Vos Johanna M, Biller Beth A, Allers Katelyn N, Faherty Jacqueline K, Liu Michael C, Metchev Stanimir, Eriksson Simon, Manjavacas Elena, Dupuy Trent J, Janson Markus, others . Spitzer variability properties of low-gravity L dwarfs // The Astronomical Journal. 2020. 160, 1. 38.

Vos Johanna M, Biller Beth A, Bonavita Mariangela, Eriksson Simon, Liu Michael C, Best William MJ, Metchev Stanimir, Radigan Jacqueline, Allers Katelyn N, Janson Markus, others . A search for variability in exoplanet analogues and low-gravity brown dwarfs // Monthly Notices of the Royal Astronomical Society. 2019. 483, 1. 480–502.

Vos Johanna M., Faherty Jacqueline K., Gagné Jonathan, Marley Mark, Metchev Stanimir, Gizis John, Rice Emily L., Cruz Kelle. Let the Great World Spin: Revealing the Stormy, Turbulent Nature of Young Giant Exoplanet Analogs with the Spitzer Space Telescope // The Astrophysical Journal. I 2022. 924, 2. 68.

Wilson PA, Rajan A, Patience Jennifer. The brown dwarf atmosphere monitoring (BAM) project-I. The largest near-IR monitoring survey of L and T dwarfs // Astronomy & Astrophysics. 2014. 566. A111.

Witte S, Helling Ch, Barman T, Heidrich N, Hauschildt PH. Dust in brown dwarfs and extra-solar planets-III. Testing synthetic spectra on observations // Astronomy & Astrophysics. 2011. 529. A44.

Wood Charlotte M., Boyajian Tabetha, von Braun Kaspar, Brewer John M., Crepp Justin R., Schaefer Gail, Adams Arthur, White Timothy R. Benchmarking Substellar Evolutionary Models Using New Age Estimates for HD 4747 B and HD 19467 B // The Astrophysical Journal. III 2019. 873, 1. 83.

Yang Hao, Apai Dániel, Marley Mark S, Karalidi Theodora, Flateau Davin, Showman Adam P, Metchev Stanimir, Buenzli Esther, Radigan Jacqueline, Artigau Étienne, others . Extrasolar storms: Pressure-dependent changes in light-curve phase in brown dwarfs from simultaneous HST and Spitzer observations // The Astrophysical Journal. 2016. 826, 1. 8.

Yang Hao, Apai Dániel, Marley Mark S, Saumon Didier, Morley Caroline V, Buenzli Esther, Artigau Étienne, Radigan Jacqueline, Metchev Stanimir, Burgasser Adam J, others . HST rotational spectral mapping of two L-type brown dwarfs: variability in and out of water bands indicates high-altitude haze layers // The Astrophysical Journal Letters. 2015. 798, 1. L13.

Zhang Zhoujian, Liu Michael C, Marley Mark S, Line Michael R, Best William MJ. Uniform Forward-modeling Analysis of Ultracool Dwarfs. II. Atmospheric Properties of 55 Late-T Dwarfs // The Astrophysical Journal. 2021. 921, 1. 95.

Zhou Yifan, Apai Dániel, Metchev Stanimir, Lew Ben WP, Schneider Glenn, Marley Mark S, Karalidi Theodora, Manjavacas Elena, Bedin Luigi R, Cowan Nicolas B, others . Cloud atlas: Rotational modulations in the L/T transition brown dwarf companion HN Peg B // The Astronomical Journal. 2018. 155, 3. 132.